

---

# Quantum transport of fermions in honeycomb lattices and cold atomic systems

**Inauguraldissertation**

zur

Erlangung der Würde eines Doktors der Philosophie

vorgelegt der

Philosophisch-Naturwissenschaftlichen Fakultät

der Universität Basel

von

Tibor Sekera

aus Trnava, Slowakei

Basel, 2018

Originaldokument gespeichert auf dem Dokumentenserver der Universität Basel

**edoc.unibas.ch**

Genehmigt von der Philosophisch-Naturwissenschaftlichen Fakultät

auf Antrag von

Prof. Christoph Bruder

Prof. Thomas L. Schmidt

Basel, den 26. Juni 2018

Prof. Martin Spiess,  
Dekan der Philosophisch-  
Naturwissenschaftlichen Fakultät

# *Abstract*

Due to the increasing demand for miniaturization, transport phenomena in many novel materials require quantum description. The first part of the thesis is concerned with quantum transport of electrons in two-dimensional materials with honeycomb lattice structure. Graphene, a honeycomb layer of carbon atoms, is the prominent example from this class of materials. In addition to the spin, the electrons in graphene have a valley degree of freedom which has the potential to encode binary information. We study a graphene  $p$ - $n$  junction in a uniform out-of-plane magnetic field as a platform to generate and controllably manipulate the valley polarization of electrons. Furthermore, graphene is also a zero band gap material, which makes the specular Andreev reflection at the interface with a superconductor feasible. In the quantum Hall regime, the interplay between specular Andreev reflections and Andreev retro-reflections in the presence of a Zeeman field can lead to a spin filtering effect. Another intriguing phenomenon, the disorder-induced transition from the trivial insulator to topological insulator phase, is also shown to take place in honeycomb materials described by the Kane-Mele Hamiltonian. A material exhibiting this behavior is termed topological Anderson insulator. Here, the parameters of the disorder-free Hamiltonian are renormalized in the presence of disorder, which leads to the topologically non-trivial phase with conducting edge states. The second part of the thesis deals with quantum transport in a junction between interacting cold atomic Fermi gases. In such a dilute cloud of fermions, the interparticle interaction can be controlled via a Feshbach resonance allowing to tune the system from the BCS state of overlapping Cooper pairs to the BEC state of tightly-bound two atomic molecules. Theoretically, we account for the interaction tunability using the generalized BCS theory. Cold atomic systems have the potential to explore condensed matter phenomena in regimes inaccessible in typical solid-state systems.





*It is not knowledge, but the act of learning,  
not possession but the act of getting there,  
which grants the greatest enjoyment.*

Carl Friedrich Gauss (1777–1855)



# *Acknowledgements*

The completion of this thesis would not be possible without the influence and support of many people, the list of which is lengthy. Here, I would like to mention some that guided, helped, or had another first-order impact on me throughout my almost-four-year period as a Ph.D. candidate at the University of Basel.

First and foremost, I would like to express my gratitude to Prof. Christoph Bruder, who made it possible for me to study and do research in his group in Basel. Besides being a great scientific advisor, he has an admirable passion for teaching, which made it very enjoyable to be the teaching assistant for his courses. He was supportive on many occasions and was always there to help, even in the broader context of life.

Notably, I want to thank Prof. Wolfgang Belzig for the scientific discussions in the earlier stages of my doctorate and the hospitality during my visit in his group in Konstanz. Furthermore, I am thankful to Prof. Thomas L. Schmidt who agreed to co-referee my thesis and Prof. Jelena Klinovaja for chairing my defense.

I feel indebted to my present and former colleagues for the fruitful discussions and all the fun events and activities, like movie nights, barbecues and rooftop table-tennis games. These are Christoph Orth, Rakesh Tiwari, Martin Koppenhöfer, Niels Lörch, Alexandre Roulet, Axel Lode, Yanick Volpez, Christina Psaroudaki, Pawel Szumniak, Silas Hoffman, Denis Chevallier, Viktoriia Kornich, Kouki Nakata, Constantin Schrade, and Bilal Kalyoncu. I would like to especially thank Marcel Serina, with whom I shared a significant part of my academic journey and who was always willing to discuss a range of scientific questions. I am thankful to many more researchers who shaped my scientific career in one way or another.

My gratitude also belongs to my friend and colleague, Ehud Amitai, who was always cheerful and taught me to look at life from various perspectives. We led many scientific and philosophical discussions that were a great source of thoughts for me. It was an honor to share the office with you. Interactions with these people were of great importance to me during my doctoral studies: Duško, Šimon, Jris, Samy, and RUM-beros. I am grateful to have you as friends.

I am thankful to have met Ksenia Kondrateva, a person who makes me feel content and walks with me through the ups and downs of life.

The sincerest gratitude belongs to my closest family members, mother Silvia, brother Michal, sister Zuzana and grandfather Július, for they were always there for me.



<b>Abstract</b>	<b>iii</b>
<b>Acknowledgements</b>	<b>vii</b>
<b>Contents</b>	<b>viii</b>
<b>Acronyms</b>	<b>xi</b>
<b>1 Introduction</b>	<b>1</b>
1.1 This thesis . . . . .	4
1.1.1 Part I: Quantum transport in materials with a honeycomb lattice .	4
1.1.2 Part II: Quantum transport in a junction between interacting cold atomic Fermi gases . . . . .	5
<b>I Quantum transport in materials with a honeycomb lattice</b>	<b>7</b>
<b>2 Theoretical Background</b>	<b>9</b>
2.1 Honeycomb lattice . . . . .	9
2.2 Tight-binding model . . . . .	10
2.3 Band structures . . . . .	12
2.3.1 Two-dimensional sheet . . . . .	12
2.3.2 Ribbons . . . . .	13
2.4 Effect of a magnetic field . . . . .	14
2.5 Low-energy approximation . . . . .	16
2.6 Landau levels in graphene . . . . .	18
2.7 Mesoscopic coherent transport: Landauer-Büttiker formalism and scat- tering matrix . . . . .	21
<b>3 Switchable valley filter based on a graphene <math>p</math>-<math>n</math> junction in a magnetic     field</b>	<b>25</b>
3.1 Introduction . . . . .	25
3.2 Setup . . . . .	28
3.3 Switchable valley filter . . . . .	30

3.4	Polarizations and transmissions upon varying potential step height and geometry . . . . .	32
3.5	Conclusion . . . . .	37
<b>4</b>	<b>Interface between graphene and superconductor</b>	<b>39</b>
4.1	Semiclassical discussion of Andreev reflection in graphene . . . . .	39
4.2	Bogoliubov-De Gennes Hamiltonian . . . . .	41
4.3	Two-terminal conductance across graphene-superconductor junction . . .	42
4.4	Two-terminal magnetoconductance across normal metal-superconductor junctions in the quantum Hall regime . . . . .	44
4.5	Spin transport in the spin-split zeroth Landau level edge states coupled to a superconductor . . . . .	48
4.6	Conclusion . . . . .	54
<b>5</b>	<b>The topological Anderson insulator phase in the Kane-Mele model</b>	<b>57</b>
5.1	Introduction . . . . .	57
5.2	Kane-Mele Hamiltonian . . . . .	60
5.3	Numerical results . . . . .	61
5.4	Lowest-order Born approximation . . . . .	63
5.5	Phase diagram . . . . .	66
5.6	Alternative disorder models . . . . .	66
5.6.1	Magnetic disorder . . . . .	66
5.6.2	Sparse disorder . . . . .	67
5.7	Conclusion . . . . .	68
<b>II</b>	<b>Quantum transport in a junction between interacting cold atomic Fermi gases</b>	<b>69</b>
<b>6</b>	<b>Thermoelectricity in a junction between interacting cold atomic Fermi gases</b>	<b>71</b>
6.1	Introduction: cold fermionic atoms . . . . .	71
6.2	Model: tunneling Hamiltonian . . . . .	74
6.3	Time evolution of the system . . . . .	77
6.4	Conclusion . . . . .	81
<b>7</b>	<b>Summary</b>	<b>83</b>
<b>A</b>	<b>Numerics in Part I</b>	<b>85</b>
A.1	Kwant: an example . . . . .	85
	<b>Bibliography</b>	<b>91</b>
	<b>List of publications</b>	<b>99</b>

---

## ACRONYMS

<b>DOS</b>	density of states
<b>GS</b>	graphene - superconductor (junction)
<b>KM</b>	Kane-Mele
<b>LL</b>	Landau level
<b>NS</b>	normal metal - superconductor (junction)
<b>SOC</b>	spin-orbit coupling
<b>TAI</b>	topological Anderson insulator





The central notion of this thesis is quantum transport. With the miniaturization of electronic devices, quantum coherence effects may start to play a significant role. Therefore the study of mesoscopic transport is not only of importance for fundamental research but may also be relevant for technological applications.

Transport of classical particles governed by Newtonian physics can be drastically different from the transport of particles described by quantum mechanics. For electrons in crystalline solids, the ratio of the mean free path  $\ell_{\text{mean}}$  and the coherence length  $\ell_{\varphi}$  of an electron can help us decide which description is appropriate. While  $\ell_{\text{mean}}$  represents the average distance between two collisions with, e.g., phonons or impurities,  $\ell_{\varphi}$  is determined by the average distance on which the phase of the electronic wavefunction is well-defined. If the sample size is much larger than  $\ell_{\text{mean}} > \ell_{\varphi}$ , the electrons in a solid move as Brownian particles and the conductivity is given by the semi-classical Drude model. Upon lowering the temperature  $T$ , both characteristic lengths increase. However, for  $T \rightarrow 0$ ,  $\ell_{\text{mean}}$  saturates at a constant value determined by the scattering with static impurities, while  $\ell_{\varphi}$  diverges. Hence, for low enough temperatures,  $\ell_{\varphi}$  may become larger than the sample size. Such a situation leads to interference and the wave nature of electrons may manifest itself in macroscopic features, e.g., in conductance. These phenomena are called mesoscopic. In the first part of the thesis we are concerned with ballistic conductance quantization, quantum Hall effect, and superconductivity in materials with a honeycomb lattice structure. In the second part we deal with tunneling between two cold atomic superfluid reservoirs.

The most famous material with a honeycomb lattice structure is graphene. It is a two-dimensional layer of carbon atoms and can be thought of as a single layer of graphite. The electronic configuration of a carbon atom in the ground state is the following: two electrons are in the inner shell occupying a  $1s$  orbital and four in the outer shell occupying  $2s$  and  $2p$  orbitals. This is often written as  $1s^2 2s^2 2p^2$ . In graphene, however, three out of the four outer-shell electrons occupy states that are superpositions of  $s$ ,  $p_x$  and  $p_y$  orbitals in order to minimize the total energy by forming in-plane covalent bonds with neighboring atoms. This is called the  $sp^2$  hybridization. The electrons in

the  $sp^2$ -hybridized orbitals can be treated as inert because they do not contribute to the transport within the range of energies used in typical experiments. The remaining electron is in the out-of-plane  $p_z$  orbital and can quantum-mechanically tunnel between the  $p_z$  orbitals of neighboring atoms in the honeycomb lattice. The resulting band structure of the  $p_z$  electrons, i.e., single-electron energies as a function of the crystal momentum, was first calculated already in 1947 by Wallace [1]. The low-energy excitations in graphene are described by a Schrödinger equation that is identical to the relativistic Dirac equation for massless fermions in  $2 + 1$ -dimensional space-time. However, it was not until the experimental breakthrough of Novoselov et al. [2] in 2004, that the popularity of graphene-related research exploded. In 2010, the Nobel Prize in Physics was awarded to Geim and Novoselov “for groundbreaking experiments regarding the two-dimensional material graphene” [3]. One of the great advantages of graphene is that the charge carrier density can be controlled by a simple application of a gate voltage. This allows for patterning a  $p$ - $n$  junction that is an elementary building block of many electronic devices. Graphene and graphene-related materials continue to be one of the leading research areas due to the strong application potential in nanotechnology as well as the contributions to the fundamental science of material physics. From now on we use term graphene as a representative of this class of materials.

An important notion in the realm of condensed matter is the quantum Hall effect, that is the quantization of the Hall resistance in strong magnetic fields. If we apply a weak magnetic field perpendicularly to the plane of a two-dimensional conductor, the electron trajectories will get slightly curved as a result of the Lorentz force. Hence, upon applying an electric field, a voltage difference develops in the direction transverse to the electric current. The transverse voltage leads to the transverse (Hall) resistance, named after its discoverer Hall in 1879 [4]. In the limit of weak magnetic fields, the Hall resistance is proportional to the out-of-plane magnetic field strength. In 1980, it was experimentally found by von Klitzing et al. [5] that for large magnetic fields ( $\sim$  few T), the Hall resistance is no longer linear but shows a stepwise behavior as a function of the field and also as a function of the charge carrier density. Such a quantization is a direct consequence of the drastic change of the density of electronic states in the presence of a strong magnetic field, i.e., the formation of Landau levels. The quantized conductance plateaus at  $h/(e^2\nu)$  can be measured with unprecedented precision, better than  $10^{-6}$ , and are used as a resistance standard. Five years after this essential experimental finding, it was recognized by a Nobel prize that was awarded to von Klitzing “for the discovery of the quantized Hall effect” [6]. The quantum Hall effect was later also measured in graphene [2, 7], where the conductance plateaus are even wider due to the high-quality graphene samples. In this thesis, we consider only the integer quantum Hall effect, where  $\nu$  can take just integer values. The case when  $\nu$  can take fractional values is realized in systems with strong electron-electron interactions and is called the fractional quantum Hall effect [8, 9]. From now on, the term quantum Hall effect refers to the integer one.

The precise quantization of the Hall conductance in the quantum Hall effect is tightly connected to the class of phenomena, for which the Nobel prize in 2016 was awarded to Thouless, Haldane, and Kosterlitz [10]. The official wording is “for theoretical discoveries of topological phase transitions and topological phases of matter”. The laureates laid the foundations of ideas used widely today in the topological classification of gapped electronic systems. While there is an elaborate mathematical theory behind such a

classification, in concrete physical examples we are often well-off with a simplified phenomenological description. One can assign a number, known as topological invariant, to a gapped Hamiltonian. Such a Hamiltonian typically depends on a set of parameters depending on which material under which circumstances we are trying to describe. The property of the topological invariant is that it cannot change upon an adiabatic change of these parameters unless a gap is closed or an underlying symmetry is broken. This leads to the notion of topologically distinct gapped electronic phases, i.e., topologically distinct Hamiltonians that cannot be deformed into each other without closing the gap or breaking an underlying symmetry. In recent years, classification of such phases was developed, and both theoretical and experimental research in this area was launched. In mathematics, topology is concerned with geometrical properties of a space that are preserved under continuous deformations. The role of such a space in the context of gapped electronic systems is played by a complex vector bundle, called the Bloch bundle. This is a mathematical structure that arises naturally for Hamiltonians that depend on crystal momentum. One example of a system with a non-trivial topology is the quantum Hall effect, where the topological invariant can take only integer values ( $\mathbb{Z}$  invariant). The system is gapped when the Fermi energy lies in between the Landau levels. Another example is the two-dimensional topological insulator, where the topological invariant in the presence of time-reversal symmetry can take only two distinct values ( $\mathbb{Z}_2$  invariant). Here, the spin-orbit interaction leads to a topologically non-trivial electronic phase. The common feature of topologically non-trivial systems is the existence of states localized at the boundary with vacuum called edge states in two-dimensions. This is a consequence of the bulk-boundary correspondence stating that the difference between the number of right and left moving modes at the boundary with vacuum is determined solely by the topological structure of the bulk [11]. The concept of topologically distinct phases can be elucidated using an analogy with the difference between a sphere and a torus from a topological point of view. The sphere cannot be continuously deformed into the torus, because the torus has a hole. The sphere and the torus, therefore, belong to different topological classes where the role of the topological invariant is played by the genus (the number of holes).

In many materials below a certain critical temperature, the effective electron-electron interaction mediated by phonons leads to the formation of Cooper pairs, large and overlapping coherent pairs of electrons. Charge in such a system can flow with zero resistance, a phenomenon known as superconductivity. The Nobel prize in 1972 was awarded to Bardeen, Cooper, and Schrieffer “for their jointly developed theory of superconductivity, usually called the BCS-theory” [12]. Another state of matter that exhibits a flow of particles without resistance is called the Bose-Einstein condensate (BEC). The two phenomena turn out to be just two sides of the same coin, more precisely, two limits of the BCS-BEC crossover that can be experimentally realized in a cloud of fermionic atoms. In such a cloud the interatomic interaction can be tuned from the weakly coupled Cooper-pair regime to the BEC regime of tightly bound molecules. The advantage of such systems is that they can simulate conditions inaccessible in conventional solid-state devices.

We ought to mention that particle-particle interactions in this thesis are neglected, or taken into account via a mean-field approximation. As a result, all the Hamiltonians are of a single-particle nature. Interactions are implicitly taken into account in two

cases: interaction of electrons and motionless ions that form the lattice resulting in the periodic lattice potential and the Bloch theory; the effective attractive interaction between fermions that leads to superconductivity.

## 1.1 This thesis

This thesis is divided into two parts: Part I deals with quantum transport in two-dimensional materials with honeycomb lattice structure, while Part II touches upon a quantum transport in a junction between two interacting cold atomic Fermi gases.

### 1.1.1 Part I: Quantum transport in materials with a honeycomb lattice

#### Chapter 2: Theoretical background

In Chapter 2 we review some of the basic notions used in the subsequent three chapters. That is, we introduce the tight-binding model of electrons on a honeycomb lattice within the nearest-neighbor approximation and calculate the band structure by diagonalizing the Hamiltonian in the momentum space. We also numerically calculate and show band structures of ribbons with zigzag and armchair edge terminations and discuss their properties. The presence of an external magnetic field affects the orbital motion as well as the spin degree of freedom of an electron. How to include this in the tight-binding descriptions is also presented. Next, we show the low-energy theory of graphene and derive the spectrum of Landau levels within this approximation. Last but not least, we briefly introduce the Landauer-Büttiker formalism and the scattering matrix.

#### Chapter 3: Switchable valley filter based on a graphene $p$ - $n$ junction in a magnetic field

In Chapter 3 we present a valley filter realized in a three-terminal device based on a graphene  $p$ - $n$  junction in a uniform quantizing magnetic field. We show that, by tuning the external potential that gives rise to a  $p$ - $n$  junction, we can switch the current from one valley polarization to the other. We also consider the effect of different types of edge terminations and present a setup, where we can partition an incoming valley-unpolarized current into two branches of valley-polarized currents. The branching ratio can be chosen by changing the location of the  $p$ - $n$  junction using a gate. The valley degree of freedom is a potential alternative to the spin degree of freedom with applications in quantum computing.

#### Chapter 4: Interface between graphene and superconductor

In Chapter 4 we study Andreev reflection at the interface between graphene and a superconductor. When the Fermi energy  $E_F$  is smaller than the superconducting pairing  $\Delta$ , the unique nature of graphene excitations allows for two kinds of Andreev reflection:

retro-reflection and specular reflection. The two are separated by a dip in the two-terminal differential conductance plotted as a function of the incoming electron energy in the absence of magnetic fields. In the presence of a quantizing magnetic field, the differential conductance as a function of the field is constant within the zeroth Landau level. That is in stark contrast to the junction based on a two-dimensional electron gas in semiconductor heterostructures with quadratic dispersion, for which the conductance oscillates as a function of the field within the zeroth Landau level. Next, we inspect a three-terminal geometry, where two leads are in a normal state and one in a superconducting state. We find that a spin-filtering effect takes place within the zeroth Landau level, if the spin-degeneracy is lifted by a Zeeman field.

## **Chapter 5: The topological Anderson insulator phase in the Kane-Mele model**

In Chapter 5 we investigate the concept of a topological Anderson insulator, i.e., a trivial insulator that is driven into a topological phase by disorder. First, we introduce the Kane-Mele model that describes a topological insulator on a honeycomb lattice. Then we show numerically, that if the system in the absence of disorder is topologically trivial, it can be driven into a topologically nontrivial phase by increasing the disorder strength. This can be understood via renormalization of the Hamiltonian parameters due to the disorder. We also present the lowest-order Born approximation and reproduce the gap closing and re-opening that is seen in the numerical calculations of the differential conductance. Next, we numerically study the presence of magnetic disorder and find, that the topological Anderson insulator phase does not occur unless the disorder term commutes with the Hamiltonian.

### **1.1.2 Part II: Quantum transport in a junction between interacting cold atomic Fermi gases**

## **Chapter 6: Thermoelectricity in a junction between interacting cold atomic Fermi gases**

In Chapter 6 we examine quasiparticle transport in a system of two weakly-coupled reservoirs of interacting ultracold fermions. While in a solid state device the interaction between the electrons is fixed, in a cloud of fermions the interatomic interaction can be tuned by an external magnetic field via a Feshbach resonance. Hence, in such a cloud one can sweep from the Bardeen-Cooper-Schrieffer (BCS) regime of large and overlapping Cooper pairs through the strongly interacting unitary regime to the Bose-Einstein condensate (BEC) regime of tightly-bound pairs. This is known as the BCS-BEC crossover. In a dilute gas, the interaction can be characterized by the s-wave scattering length. Using the generalized BCS theory, where the scattering length explicitly enters, we calculate the time evolution of the two-reservoir system that is assumed to be initially prepared in a nonequilibrium state characterized by a particle number imbalance or a temperature imbalance. We find a number of characteristic features like sharp peaks in quasiparticle currents or transitions between the normal and superconducting states.

Put in a broader context, the high tunability in a cloud of ultracold atoms allows for an experimental realization of a system that reproduces physics of a precisely defined Hamiltonian, i.e., a quantum simulator [13].

## Part I

# Quantum transport in materials with a honeycomb lattice





## 2.1 Honeycomb lattice

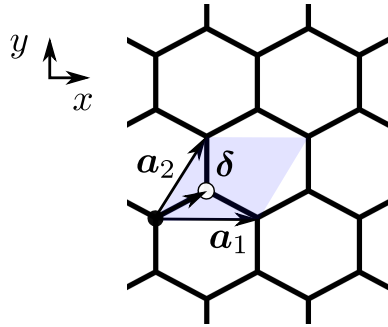


FIGURE 2.1: Honeycomb lattice structure of graphene. The two Bravais lattice vectors  $\mathbf{a}_1$  and  $\mathbf{a}_2$  and the basis vector  $\boldsymbol{\delta}$  are shown. The unit cell is marked with a blue-shaded rhombus. The black and white circles show the A and B sublattice atom in the unit cell, respectively.

The honeycomb lattice structure is shown in Fig. 2.1. It is a triangular lattice with a two-atomic basis. The two primitive (lattice) vectors are

$$\begin{aligned}\mathbf{a}_1 &= a(1, 0), \\ \mathbf{a}_2 &= a\left(\frac{1}{2}, \frac{\sqrt{3}}{2}\right),\end{aligned}\tag{2.1}$$

where  $a$  is the lattice constant,  $a = 0.246$  nm for graphene. The basis vector connecting a site from sublattice  $A$  to the site from sublattice  $B$  in the same unit cell is

$$\boldsymbol{\delta} = a\left(\frac{1}{2}, \frac{1}{2\sqrt{3}}\right).\tag{2.2}$$

The position of any site in the sublattice  $A$  can be expressed as

$$\mathbf{R}_i = n\mathbf{a}_1 + m\mathbf{a}_2,\tag{2.3}$$

while in the sublattice  $B$  as

$$\mathbf{R}_i + \boldsymbol{\delta} = n\mathbf{a}_1 + m\mathbf{a}_2 + \boldsymbol{\delta}. \quad (2.4)$$

Here,  $n$  and  $m$  are integers.

## 2.2 Tight-binding model

The nearest-neighbor (nn) tight-binding model of electrons on a honeycomb lattice is given by the Hamiltonian

$$H = -E_F \sum_i c_i^\dagger c_i + \sum_{\langle ij \rangle} t_{ij} c_i^\dagger c_j, \quad (2.5)$$

where the first term accounts for the Fermi energy, while the second term for the nn hopping. The sum over  $\langle ij \rangle$  runs over the nearest neighbors, and  $t_{ij}$  is the nn hopping amplitude, e.g.,  $t_{\langle ij \rangle} = -t \approx 2.5 \text{ eV}$  for graphene.  $c_i^\dagger (c_i)$  creates (annihilates) a particle in a Wannier state localized at the site at position  $\mathbf{R}_i$ . In the (single-particle) basis of Wannier states  $\{|\mathbf{R}_i\rangle, |\mathbf{R}_i + \boldsymbol{\delta}\rangle\}$ , the Hamiltonian has a sparse matrix structure with hopping element  $-t$  between the nearest neighbors and 0 otherwise.

According to Bloch's theorem, the Hamiltonian (2.5) can be diagonalized using the following ansatz

$$|\mathbf{k}\rangle = c_A(\mathbf{k}) |A(\mathbf{k})\rangle + c_B(\mathbf{k}) |B(\mathbf{k})\rangle, \quad (2.6)$$

where the two kets on the right-hand side are two Bloch sums on the respective sublattices:

$$\begin{aligned} |A(\mathbf{k})\rangle &= \frac{1}{\sqrt{N}} \sum_i e^{i\mathbf{k} \cdot \mathbf{R}_i} |\mathbf{R}_i\rangle, \\ |B(\mathbf{k})\rangle &= \frac{1}{\sqrt{N}} \sum_i e^{i\mathbf{k} \cdot (\mathbf{R}_i + \boldsymbol{\delta})} |\mathbf{R}_i + \boldsymbol{\delta}\rangle. \end{aligned} \quad (2.7)$$

Here,  $N$  is the number of unit cells in the volume under consideration and  $\mathbf{k}$  is the wave vector associated with the crystal momentum  $\hbar\mathbf{k}$ . The periodic boundary conditions

$$\begin{aligned} |\mathbf{R}_i + N_1\mathbf{a}_1\rangle &= |\mathbf{R}_i\rangle, \\ |\mathbf{R}_i + N_2\mathbf{a}_2\rangle &= |\mathbf{R}_i\rangle, \end{aligned} \quad (2.8)$$

where  $N_1$  and  $N_2$  are large integers, restrict the wave vectors to discrete values

$$\mathbf{k} = \frac{2\pi}{a} \left( \frac{n_1}{N_1}, \frac{1}{\sqrt{3}} \left( \frac{2n_2}{N_2} - \frac{n_1}{N_1} \right) \right), \quad (2.9)$$

with  $n_1$  and  $n_2$  being integers. The wave vector can be expressed as  $\mathbf{k} = \frac{n_1}{N_1}\mathbf{b}_1 + \frac{n_2}{N_2}\mathbf{b}_2$  using reciprocal lattice vectors

$$\begin{aligned} \mathbf{b}_1 &= \frac{2\pi}{a} \left( 1, -\frac{1}{\sqrt{3}} \right), \\ \mathbf{b}_2 &= \frac{2\pi}{a} \left( 0, \frac{2}{\sqrt{3}} \right), \end{aligned} \quad (2.10)$$

defined as  $\mathbf{a}_i \mathbf{b}_j = 2\pi \delta_{ij}$ .

Plugging the ansatz in Eq. (2.6) into the Schrödinger equation we obtain the following block-diagonal form

$$\begin{pmatrix} H_{AA}(\mathbf{k}) & H_{AB}(\mathbf{k}) \\ H_{BA}(\mathbf{k}) & H_{BB}(\mathbf{k}) \end{pmatrix} \begin{pmatrix} c_A(\mathbf{k}) \\ c_B(\mathbf{k}) \end{pmatrix} = E(\mathbf{k}) \begin{pmatrix} c_A(\mathbf{k}) \\ c_B(\mathbf{k}) \end{pmatrix}, \quad (2.11)$$

where

$$H_{AA}(\mathbf{k}) = H_{BB}(\mathbf{k}) = -E_F \quad (2.12)$$

and

$$H_{AB}(\mathbf{k}) = \frac{1}{N} \sum_{ij} e^{i\mathbf{k} \cdot (\mathbf{R}_j + \boldsymbol{\delta} - \mathbf{R}_i)} \langle \mathbf{R}_i | H | \mathbf{R}_j + \boldsymbol{\delta} \rangle \quad (2.13)$$

with  $H_{AB}(\mathbf{k}) = H_{BA}^*(\mathbf{k})$ . In Eq. (2.11) we neglected the overlap of the Wannier wave-functions localized at the lattice sites, that is we assumed  $\langle \mathbf{R} | \mathbf{R}' \rangle = \delta_{\mathbf{R}\mathbf{R}'}$ .

The expectation value  $\langle \mathbf{R}_i | H | \mathbf{R}_j + \boldsymbol{\delta} \rangle$  is equal to  $-t$  for the three nearest neighbors of site  $i$ , i.e., sites with coordinates

$$\mathbf{R}_j + \boldsymbol{\delta} = \begin{cases} \mathbf{R}_i + \boldsymbol{\delta}, \\ \mathbf{R}_i - \mathbf{a}_1 + \boldsymbol{\delta}, \\ \mathbf{R}_i - \mathbf{a}_2 + \boldsymbol{\delta}, \end{cases} \quad (2.14)$$

and zero otherwise (Fig. 2.1). Hence,

$$H_{AB}(\mathbf{k}) = -te^{i\mathbf{k} \cdot \boldsymbol{\delta}} (1 + e^{-i\mathbf{k} \cdot \mathbf{a}_1} + e^{-i\mathbf{k} \cdot \mathbf{a}_2}). \quad (2.15)$$

The eigenenergies are obtained by diagonalizing the 2x2 matrix in Eq. (2.11) and are given by

$$E(\mathbf{k}) = -E_F + \lambda t \sqrt{1 + 4 \cos\left(\frac{a}{2}k_x\right) \cos\left(\frac{a\sqrt{3}}{2}k_y\right) + 4 \cos^2\left(\frac{a}{2}k_x\right)}, \quad (2.16)$$

where  $\lambda = \pm 1$  is for the conduction and valence band, respectively.  $E(\mathbf{k})$  can be plotted as a function of  $k_x$  and  $k_y$ , which yields the band structure shown in Fig. 2.2.

Note that Eq. (2.5) is the simplest version of a tight-binding Hamiltonian describing the physics of electrons on a honeycomb lattice. We might consider other terms entering the Hamiltonian, depending on which effect (or which material) we wish to study. For instance, we will introduce the orbital effect of the magnetic field by adding the Peierls phase to the nn hopping term in Chapter 3. On top of that, in Chapter 4 we couple the

spin degree of freedom to the magnetic field via the Zeeman term, and add the superconducting pairing of electrons and holes within the Bogoliubov-De Gennes framework. To model topological insulators with honeycomb lattice structure, in Chapter 5 we will introduce intrinsic and extrinsic (Rashba) spin-orbit coupling terms and the staggered sublattice potential that lifts the sublattice symmetry. The spin-orbit terms may be less relevant for graphene, but gain importance for other materials such as germanene, stanene, and silicene. Finally, in Chapter 5 we include disorder effects via the random on-site potential.

## 2.3 Band structures

In this section we review band structures of a two-dimensional graphene sheet, and one-dimensional zigzag and armchair ribbon.

### 2.3.1 Two-dimensional sheet

The periodic boundary conditions in Eq. (2.8) describe an infinite two-dimensional sheet of a honeycomb lattice and lead to the band structure in Eq. (2.16). If plotted as a function of  $k_x$  and  $k_y$ , we can observe six Dirac cones in the corners of the first Brillouin zone (Dirac points), as shown in Fig. 2.2. In the case of undoped graphene, the Fermi energy lies at the Dirac point,  $E = 0$ . Hence, the band structure in the vicinity of this point is particularly important. Only two out of the six Dirac points can be chosen as inequivalent, i.e., such that they cannot be connected by the reciprocal lattice vectors. Once chosen, the low-energy excitations can be thought of as located in two separate regions in momentum space, so-called *valleys*. The band structure in the valleys has a linear character, see Sec. 2.5.

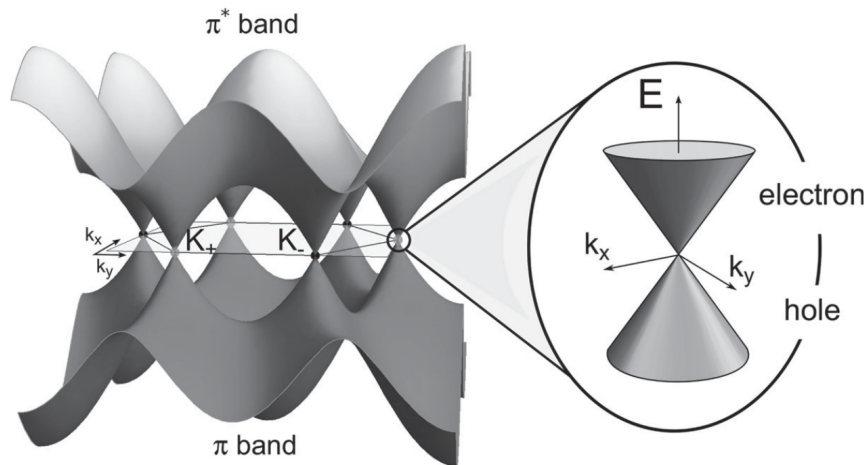


FIGURE 2.2: Band structure of a two-dimensional graphene sheet. Reproduced from Ref. [14].

### 2.3.2 Ribbons

Now we review the band structure of ribbons, also called nanoribbons or strips in the literature. These are one-dimensional (1D) slices of a 2D honeycomb sheet of width  $W$ , as shown for the zigzag and armchair edge termination in Fig. 2.3(a-b). The two cases are related via rotation of the honeycomb lattice by  $\pi/6$  angle. In this thesis, the 1D ribbons serve as leads, i.e., translationally invariant systems with well-defined scattering states. The leads allow us to calculate the scattering matrix that describes transport properties of the scattering region to which the leads are attached, see Sec. 2.7. Experimentally, graphene ribbons with more or less well-defined edges can be made using several techniques. To mention some: lithographic patterning of graphene samples [15], unzipping a carbon nanotube [16], chemical bottom-up approach [17], anisotropic etching by hydrogen plasma [18] or nickel nanoparticles [19], and several others.

Below we present band structures of a zigzag and armchair ribbon calculated numerically by diagonalizing the tight-binding Hamiltonian (2.5) with proper boundary conditions. For the review and derivation of analytical expressions from the tight-binding model see Ref. [20].

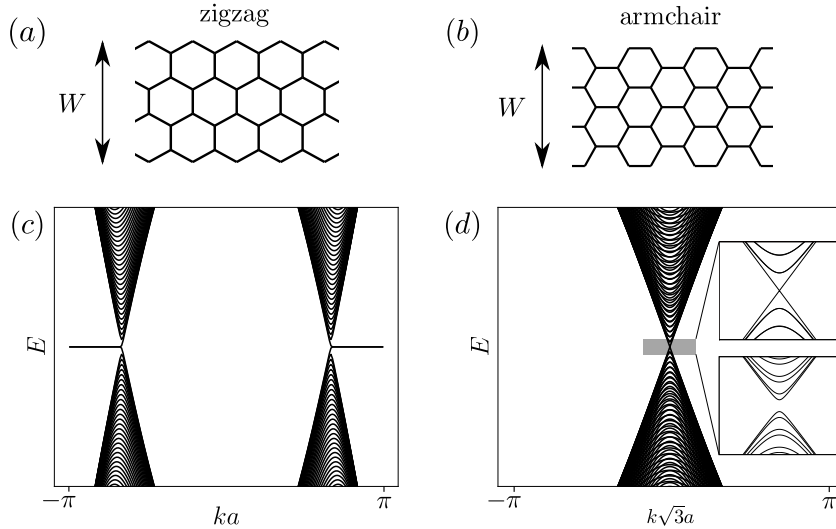


FIGURE 2.3: Graphene ribbons and their band structures. (a) A zigzag ribbon of width  $W = 5a/\sqrt{3}$  and with the unit cell (dashed rectangle) of width  $a$ . (b) An armchair ribbon with  $W = 3a$  and with the unit cell of width  $\sqrt{3}a$ . (c) Band structure of a zigzag ribbon ( $W = 149.245a$ ) and (d) of an armchair ribbon ( $W = 149a$ ). The armchair ribbon can be either metallic or gapped, see the upper or lower panel of the inset in (d), respectively. The metallic case occurs when  $2W = 2 \pmod{3}$ , and the gapped cases otherwise.

#### Zigzag ribbon

The low-energy band structure of a zigzag ribbon is shown in Fig. 2.3(c). The bulk bands are separated in momentum space into two valleys connected by a flat edge band. The flat band appears within the region  $2\pi/3 \leq |k| \leq \pi$  (for  $W \rightarrow \infty$ ), which can be understood by considering a wavefunction at the zigzag edge of a semi-infinite honeycomb sheet [20]. Away from zero energy, this band disperses and forms propagating edge

states, which are more delocalized further from zero energy. The band structure of a zigzag ribbon has zero gap and the ribbon is always metallic.

Due to the separation of the states in momentum space, a zigzag ribbon can be used as a probe for a valley polarization (in analogy to the spin polarization) [21]. We investigate a valley filtering effect in Chapter 3.

It is worth mentioning that due to the flat band the density of states is highly enhanced at  $E = 0$ , which results in non-zero magnetization at the edge in the presence of electron-electron interaction [22, 23].

### Armchair ribbon

The low-energy band structure of an armchair ribbon is shown in Fig. 2.3(d). The states are not valley-resolved in momentum space. The band structure of an armchair ribbon can be obtained by slicing the bandstructure of a 2D sheet, and the low-energy spectrum can be described as a superposition of the two valleys of the 2D sheet.

Depending on the width of the ribbon, either a metallic or a gapped state is realized. Namely, the metallic case occurs when  $2W = 2 \pmod{3}$  and the gapped case otherwise, with the magnitude of the gap proportional to  $1/W$ . The threefold character manifests itself also in transport properties, whenever an armchair ribbon is included, see Figs. 3.7 and 4.12.

## 2.4 Effect of a magnetic field

The orbital motion in 2D materials in presence of an out-of-plane magnetic field can be understood as follows. If the field is weak, the (semiclassical) trajectories of electrons are slightly curved which results in an accumulation of charge imbalance transverse to the direction of applied current. Hence, one can measure a non-zero transverse (Hall) conductance proportional to the field strength  $B$ . This is the classical Hall effect, first measured in 1879 [4]. Upon further increasing  $B$ , the semiclassical trajectories are curved more and more, and they become circular eventually. This leads to the situation, where the electrons in the bulk of a sample are localized on circular orbits (discrete spectrum of Landau levels). However, close to the boundary with vacuum, the electrons bounce from the edge and form a skipping orbit (propagating edge state). In this situation, the Hall conductivity is no longer linear in  $B$  and exhibits quantized steps. This phenomenon, termed integer quantum Hall effect, was first measured experimentally [5], and only later explained theoretically. For the quantum Hall effect to be observable, one needs  $\ell_B = \sqrt{\hbar/eB} < \text{sample size}$ , so that the sample is large enough for the circular orbit to form, and  $\omega_c\tau > 1$ , so that the electron makes at least one circular turn on the semiclassical orbit before a collision. Here,  $\omega_c$  is the cyclotron frequency characterizing the circular motion of an electron in a magnetic field and  $\tau$  is the collision rate.

The magnetic field also influences the spin degree of freedom. The coupling of the electronic spin to the external magnetic field enters the Hamiltonian in the Schrödinger

equation as a result of the non-relativistic approximation to the relativistic Dirac equation. In this thesis we will treat it merely as another term in the Hamiltonian regardless of its origin.

Below we describe, how the influence of an external magnetic field on the orbital and spin degree of freedom can be included in tight-binding Hamiltonian (2.5).

### Orbital effect in the tight-binding model

Let us consider a magnetic field perpendicular to the graphene sheet, since in 2D materials only the out-of-plane component of magnetic field plays a role in orbital effects. This can be included in the hopping term (kinetic part) of Hamiltonian (2.5) by adding a complex phase to the hopping amplitude. Namely,

$$t_{ij} = -te^{i\varphi_{ij}}, \quad (2.17)$$

where

$$\varphi_{ij} = \frac{e}{\hbar} \int_j^i \mathbf{A} \cdot d\mathbf{r} \quad (2.18)$$

is the Peierls phase [24] accumulated by an electron hopping from site  $j$  to site  $i$  along a straight line.  $\mathbf{A}$  is the vector potential corresponding to the out-of-plane magnetic field  $\mathbf{B} = \nabla \times \mathbf{A}$ . It is often convenient to choose the Coulomb gauge,  $\nabla \cdot \mathbf{A} = 0$ . This gauge does not determine  $\mathbf{A}$  uniquely. Hence, in the presence of leads, i.e., systems with discrete translational symmetry, we are allowed to choose  $\mathbf{A}$  such that it respect this symmetry.

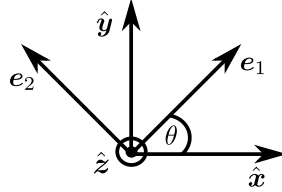


FIGURE 2.4: Orientation of the vector  $\mathbf{e}_1$  that is parallel to the translational symmetry vector of the lead, and the transverse vector  $\mathbf{e}_2$ . The external magnetic field is applied along the  $z$  axis.

Let us confine the electron motion to the  $x$ - $y$  plane and consider the  $B$  field along the  $z$  axis,  $\mathbf{B} = (0, 0, B)$ . For a general orientation of the translational symmetry vector of the lead shown as  $\mathbf{e}_1$  in Fig. 2.4, the proper gauge respecting the translational symmetry is

$$\mathbf{A} = -B(\mathbf{r} \cdot \mathbf{e}_2)\mathbf{e}_1, \quad (2.19)$$

where  $\mathbf{e}_1 = (\cos \theta, \sin \theta)^T$  and  $\mathbf{e}_2 = (-\sin \theta, \cos \theta)^T$ , see also Appendix of Ref. [25]. We can parametrize the straight line from site  $j$  to site  $i$  as

$$\begin{aligned} x &= x_j + (x_i - x_j)t, \\ y &= y_j + (y_i - y_j)t, \end{aligned} \quad (2.20)$$

where  $(x_i, y_i)$  are coordinates of the site  $i$  and  $t \in [0, 1]$ . For the Peierls phase in Eq. (2.18) we obtain the following expression

$$\varphi_{ij} = \frac{eB}{2\hbar} \left[ (x_j y_i - x_i y_j) - \cos 2\theta (x_i y_i - x_j y_j) + \frac{\sin 2\theta}{2} (x_i^2 - x_j^2 - y_i^2 + y_j^2) \right]. \quad (2.21)$$

Therefore, choosing a lead along the  $x$  axis ( $\theta = 0$ ), we obtain

$$\varphi_{ij} = -\frac{eB}{2\hbar} (x_i - x_j)(y_i + y_j) \quad (2.22)$$

while for a lead along the  $y$  axis ( $\theta = \pi/2$ )

$$\varphi_{ij} = \frac{eB}{2\hbar} (y_i - y_j)(x_i + x_j). \quad (2.23)$$

### **Zeeman effect in the tight-binding model**

An external magnetic field couples also to the spin degree of freedom via term  $\propto \boldsymbol{\mu} \cdot \mathbf{B}$ , where  $\boldsymbol{\mu}$  is the magnetic moment of an electron (Zeeman effect). This can be included in the tight-binding model via an on-site term  $\Delta_Z \sum_i (c_{i\uparrow}^\dagger c_{i\uparrow} - c_{i\downarrow}^\dagger c_{i\downarrow})$ , where  $i$  is the site index and  $\uparrow$  ( $\downarrow$ ) is for spin up (down). This essentially splits the spin-degenerate single-electron states in energy. The energy difference between the two spin states for an electron in vacuum is  $2\Delta_Z$ , where

$$\Delta_Z = \frac{1}{2} g \mu_B B. \quad (2.24)$$

Here,  $g \approx 2.0023$  is the effective Landé factor ( $g$ -factor),  $\mu_B = e\hbar/2m_e$  is the Bohr magneton with  $m_e$  being the electron rest mass in vacuum, and  $B = |\mathbf{B}|$  is the magnitude of the magnetic field. The  $g$ -factor for an electron in graphene is enhanced by interaction effects. This can be included by replacing  $g$  by effective  $g^*$ , which is found to be in range  $2 \leq g^* \lesssim 4$ , Ref. [26, 27]. Therefore, the Zeeman energy can reach up to

$$\Delta_Z = 2.3 \text{ meV}, \quad (2.25)$$

for  $B = 10 \text{ T}$  and  $g^* = 4$ . The magnetic field in Eq. (2.24) is  $B = \sqrt{B_\perp^2 + B_\parallel^2}$ , where  $B_\perp$  is the out-of-plane component and  $B_\parallel$  is the in-plane component of the field. Note, that while the orbital motion is affected only by  $B_\perp$ , the spin degree of freedom experiences both,  $B_\perp$  and  $B_\parallel$ .

## **2.5 Low-energy approximation**

In this section we present the famous linear (low-energy) approximation to the block-diagonal Hamiltonian in Eq. (2.11) and energy in Eq. (2.16). We choose the two Dirac points to be

$$\mathbf{K}^\xi = \left( \xi \frac{4\pi}{3a}, 0 \right), \quad (2.26)$$



where  $\xi = \pm 1$ . To obtain the low-energy (long-wavelength) Hamiltonian of graphene, we plug  $\mathbf{k} = \mathbf{K}^\xi + \mathbf{q}$  into Eq. (2.11) assuming with  $q \ll 1/a$ , where  $q = \sqrt{q_x^2 + q_y^2}$ . We perform the Taylor expansion keeping only terms linear in  $q_x$  and  $q_y$ .<sup>1</sup> Hence, the Hamiltonian in the vicinity of  $\mathbf{K}^\xi$  is

$$\begin{pmatrix} -E_F & \hbar v_F(\xi q_x - i q_y) \\ \hbar v_F(\xi q_x + i q_y) & -E_F \end{pmatrix} \begin{pmatrix} c_A(\mathbf{K}^\xi + \mathbf{q}) \\ c_B(\mathbf{K}^\xi + \mathbf{q}) \end{pmatrix} = E(\mathbf{K}^\xi + \mathbf{q}) \begin{pmatrix} c_A(\mathbf{K}^\xi + \mathbf{q}) \\ c_B(\mathbf{K}^\xi + \mathbf{q}) \end{pmatrix}, \quad (2.27)$$

where we defined the Fermi velocity as  $\hbar v_F = -\sqrt{3}at/2$ , for graphene  $v_F \approx 10^6$  m/s. Consequently, the low-energy spectrum

$$E(\mathbf{K}^\xi + \mathbf{q}) = -E_F + \lambda \hbar v_F q \quad (2.28)$$

is independent of the valley index and is linear, i.e., has a form of a double cone, in the vicinity of each of the Dirac points (inset of Fig. 2.2). We can combine the two pairs of equations (2.27) into one set of four equations as

$$\begin{pmatrix} -E_F & \hbar v_F(q_x - i q_y) & 0 & 0 \\ \hbar v_F(q_x + i q_y) & -E_F & 0 & 0 \\ 0 & 0 & -E_F & \hbar v_F(-q_x + i q_y) \\ 0 & 0 & \hbar v_F(-q_x - i q_y) & -E_F \end{pmatrix} \begin{pmatrix} c_A(\mathbf{K}^+ + \mathbf{q}) \\ c_B(\mathbf{K}^+ + \mathbf{q}) \\ c_B(\mathbf{K}^- + \mathbf{q}) \\ c_A(\mathbf{K}^- + \mathbf{q}) \end{pmatrix} = E(\mathbf{q}) \begin{pmatrix} c_A(\mathbf{K}^+ + \mathbf{q}) \\ c_B(\mathbf{K}^+ + \mathbf{q}) \\ c_B(\mathbf{K}^- + \mathbf{q}) \\ c_A(\mathbf{K}^- + \mathbf{q}) \end{pmatrix}. \quad (2.29)$$

We see that the low-energy excitations in one valley do not couple to the excitations in the other valley. The off-diagonal terms coupling the two valleys appear when a scatterer is introduced, e.g., an edge or disorder on the scale of the lattice constant.

The low-energy Hamiltonian can be written compactly using tensor products of Pauli matrices as

$$H = -E_F \tau_0 \otimes \sigma_0 + \hbar v_F \tau_z \otimes (\boldsymbol{\sigma} \cdot \mathbf{q}), \quad (2.30)$$

where  $\tau_\nu$  and  $\sigma_\nu$  with  $\nu = \{0, 1, 2, 3\}$  are two sets of Pauli matrices describing the valley and sublattice degree of freedom, respectively. The four eigenvectors of Hamiltonian (2.30) can be written as four-spinors

$$\begin{pmatrix} \lambda \frac{q}{q_x + i q_y} \\ 1 \\ 0 \\ 0 \end{pmatrix} \quad \text{and} \quad \begin{pmatrix} 0 \\ 0 \\ 1 \\ -\lambda \frac{q}{q_x + i q_y} \end{pmatrix}. \quad (2.31)$$

---

<sup>1</sup>Tight-binding terms, such as the overlap of the Wannier functions on the neighboring sites and the next-nearest-neighbor hopping lead to corrections of the order of  $q^2 a^2$ . To be consistent, this is neglected in our derivation.

Note, that another common form of the Hamiltonian (2.30),  $H' = -E_F\tau_0 \otimes \sigma_0 + \hbar v_F\tau_0 \otimes (\boldsymbol{\sigma} \cdot \mathbf{q})$ , is commonly used in the literature [28]. It is related to the one in Eq. (2.30) by a unitary transformation  $H' = U H U^\dagger$ , where  $U = (\tau_0 + \tau_z)/2 \otimes \sigma_0 + (\tau_0 - \tau_z)/2 \otimes \sigma_z$ .

## 2.6 Landau levels in graphene

Here we derive the quantized energy levels within the low-energy approximation (2.30) in the presence of a strong magnetic field.

To include a coupling of the orbital motion to the magnetic field  $\mathbf{B} = (0, 0, B)$  with the vector potential in Landau gauge  $\mathbf{A} = (0, Bx, 0)$ , we replace the canonical momentum by the gauge-invariant momentum. The low-energy Hamiltonian (2.30) then takes the following form in a magnetic field

$$H = \hbar v_F \tau_z \otimes \boldsymbol{\sigma} \cdot (\mathbf{q} + e\mathbf{A}), \quad (2.32)$$

where we set  $E_F = 0$ , since it is just a constant shift of the energies. Hence, the Schrödinger equation is

$$H\Psi = E\Psi, \quad (2.33)$$

where  $\Psi = (\psi_A^+, \psi_B^+, \psi_B^-, \psi_A^-)^T$  is a four-spinor;  $\psi_{A(B)}^\pm$  is the amplitude of the wavefunction on  $A(B)$  sublattice in  $K^\pm$  valley.

To solve Eq. (2.33) means to find eigenvalues and corresponding eigenfunctions of the Hamiltonian (2.32). We introduce a transformation using the annihilation and creation operators

$$\begin{aligned} a &= \frac{\ell_B}{\sqrt{2}\hbar}(\hbar q_x - i(\hbar q_y + eBx)), \\ a^\dagger &= \frac{\ell_B}{\sqrt{2}\hbar}(\hbar q_x + i(\hbar q_y + eBx)), \end{aligned} \quad (2.34)$$

with bosonic commutation relation  $[a, a^\dagger] = 1$ . The inverse transformation is

$$\begin{aligned} \Pi_x &= \frac{\hbar}{\sqrt{2}\ell_B}(a^\dagger + a), \\ \Pi_y &= \frac{\hbar}{i\sqrt{2}\ell_B}(a^\dagger - a), \end{aligned} \quad (2.35)$$

where the gauge-invariant momentum is  $\Pi_i = \hbar q_i + eA_i$ . Plugging this transformation into Hamiltonian (2.32) we obtain

$$H = \hbar\omega_c \begin{pmatrix} 0 & a & 0 & 0 \\ a^\dagger & 0 & 0 & 0 \\ 0 & 0 & 0 & -a \\ 0 & 0 & -a^\dagger & 0 \end{pmatrix} \quad (2.36)$$

where we denoted the cyclotron frequency  $\hbar\omega_c = \sqrt{2}\hbar v_F/\ell_B$ . Eq. (2.33) is a system of four pairwise coupled equations

$$\begin{aligned}\hbar\omega_c a\psi_B^+ &= E\psi_A^+, \\ \hbar\omega_c a^\dagger\psi_A^+ &= E\psi_B^+, \\ -\hbar\omega_c a\psi_B^- &= E\psi_A^-, \\ -\hbar\omega_c a^\dagger\psi_A^- &= E\psi_B^-. \end{aligned} \tag{2.37}$$

Eliminating  $\psi_A^+$  from the first two yields

$$a^\dagger a\psi_B^+ = \frac{E^2}{(\hbar\omega_c)^2}\psi_B^+. \tag{2.38}$$

Since  $\psi_B^+$  is an eigenstate of  $a^\dagger a$ , then  $\psi_B^+ = \alpha|n\rangle$ ,  $\alpha \in \mathbb{C}$ . It follows that

$$a^\dagger a\alpha|n\rangle = \alpha n|n\rangle = \frac{E^2}{(\hbar\omega_c)^2}\alpha|n\rangle, \tag{2.39}$$

where in the first equation we used the fact that  $a^\dagger a|n\rangle = n|n\rangle$ ,  $n = 0, 1, 2, \dots$  and the second equation follows from (2.38). Hence the eigenenergies are

$$E_n = \lambda\hbar\omega_c\sqrt{n}, \tag{2.40}$$

Using the well-known relations between the bosonic operators and their eigenstates

$$\begin{aligned}a|n\rangle &= \sqrt{n}|n-1\rangle, \\ a^\dagger|n\rangle &= \sqrt{n+1}|n+1\rangle, \end{aligned} \tag{2.41}$$

and fixing  $\psi_B^+ = |n\rangle$ , we obtain for the  $\psi_A^+$  component

$$\psi_A^+ = \frac{\hbar\omega_c}{E_n}a|n\rangle = \frac{1}{\lambda}|n-1\rangle. \tag{2.42}$$

The second pair of equations in Eq. (2.37) can be treated analogously and yields the same eigenenergies as in Eq. (2.40). The corresponding eigenstates are  $\psi_A^- = |n\rangle$  and  $\psi_B^- = -\frac{1}{\lambda}|n-1\rangle$ .

To summarize, the resulting normalized eigenstate in Eq. (2.33) is

$$\Psi_n = \frac{1}{2} \begin{pmatrix} |n-1\rangle \\ \lambda|n\rangle \\ |n-1\rangle \\ -\lambda|n\rangle \end{pmatrix} \tag{2.43}$$

with the corresponding eigenvalue

$$E_n = \lambda\hbar\omega_c\sqrt{n} = \lambda\frac{\hbar v_F}{\ell_B}\sqrt{2n}. \tag{2.44}$$

These eigenenergies are called Landau levels (LLs). They are different from the LLs that arise in a conventional two-dimensional electron gas with  $E'_n = \hbar\omega'_c(n + 1/2)$ , where  $\omega'_c = eB/m$ . See Fig. 2.5 for the behaviour of the LLs as a function of a magnetic field.

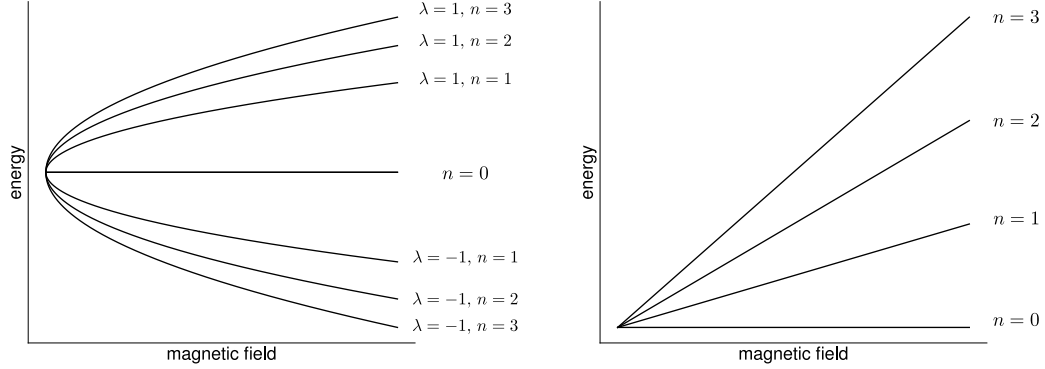


FIGURE 2.5: Landau levels as a function of an out-of-plane magnetic field in (a) graphene and in (b) a conventional two-dimensional electron gas.

We can plug in the tight-binding parameters to obtain

$$E_n = \lambda |t| \sqrt{2\sqrt{3}\pi\phi/\phi_0} \sqrt{n}, \quad (2.45)$$

where we introduced the magnetic flux through the unit cell  $\phi = BS$  with the unit cell area  $S = \sqrt{3}a^2/2$  and the magnetic flux quantum  $\phi_0 = h/e$ . The energy gap between the  $n = 1$  and  $n = 0$  LL is  $\delta = |t| \sqrt{2\sqrt{3}\pi\phi/\phi_0} \approx 3.3|t| \sqrt{\phi/\phi_0}$ .

A peculiar situation arises for the zeroth Landau level ( $n = 0$ ). Here the bulk eigenstate is

$$\Psi_0 = \frac{1}{\sqrt{2}} \begin{pmatrix} 0 \\ \lambda |0\rangle \\ 0 \\ -\lambda |0\rangle \end{pmatrix}, \quad (2.46)$$

which means that the sublattice and valley degree of freedom are locked together: when an electron is in a state in  $K^+(K^-)$  valley, it has zero probability to be on the  $A(B)$  sublattice.

The existence of LLs implies the quantization of the Hall resistance, i.e., the quantum Hall effect. The LLs are flat (momentum-independent) in the bulk, however, towards the edge of the sample, the LLs bend upwards (downwards) for the conduction (valence) band due to the edge potential. This bending means that the states close to the edge acquire a finite velocity. The direction of propagation at the edge is fixed and the propagating edge states cannot backscatter. Hence, if the Fermi energy is in between the bulk Landau levels, one can measure the quantized Hall resistance ( $R_H$ ) in a Hall-bar geometry

$$R_H = \frac{1}{\nu} \frac{h}{e^2}, \quad (2.47)$$

where  $\nu$  is the filling factor, i.e., the number of occupied LLs. If we also account for the spin degree of freedom, for spin-degenerate electrons in graphene the sequence is  $\nu = \pm 2, \pm 6, \pm 10, \dots$ , while for a conventional 2DEG it is  $\nu = 0, 2, 4, 6, \dots$ . However, note that the degeneracy of LLs may be lifted as a result of, e.g., the Zeeman effect. This results in different filling factor sequences. Since the energy gaps between the first few LLs in graphene are large enough, the resistance quantization (2.47) can be measured already at relatively small field strengths [29], and even at room temperatures [7] in this material.

## 2.7 Mesoscopic coherent transport: Landauer-Büttiker formalism and scattering matrix

### Landauer-Büttiker formalism

Mesoscopic transport is coherent if the size of the sample is smaller than coherence length. Landauer, Büttiker and Imry developed a widely used framework for the description of such transport. Here we summarize the main results.

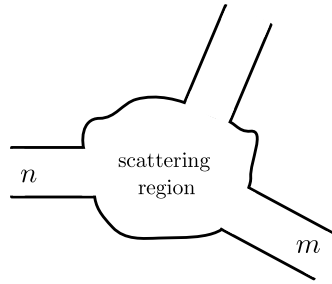


FIGURE 2.6: Mesoscopic system with quasi-one-dimensional leads connected to the scattering region.

Consider the system shown in Fig. 2.6. There are (quasi) one-dimensional leads connected to the scattering region. Leads are translationally-invariant systems that have well-defined scattering states and serve as a probe of the transport properties of the scattering region. In general, each state in lead  $n$  can be written as a product of a stationary wave in the transverse direction and a propagating wave in the longitudinal direction<sup>2</sup>. To each longitudinal wave vector there is  $N_n(E)$  transverse waves at energy  $E$ , called modes, and their number depends on the transverse size of the lead. Transmission amplitude from mode  $\alpha$  in lead  $m$  to mode  $\beta$  in lead  $n$  at energy  $E$  is denoted as  $t_{n\beta,m\alpha}(E)$  and depends on the details of the scattering region. The total transmission probability from lead  $m$  to lead  $n$  at energy  $E$  (transmission function) is given by

$$T_{nm}(E) = \sum_{\beta=1}^{N_n} \sum_{\alpha=1}^{N_m} |t_{n\beta,m\alpha}(E)|^2. \quad (2.48)$$

<sup>2</sup>Besides the propagating waves, there are evanescent waves with imaginary wave vector which do not carry current. However, they have an indirect effect on the conductance. For simplicity, the evanescent modes are excluded from this discussion but included in the numerical approach below.

Then, the summation rule

$$\sum_m T_{nm}(E) = \sum_m T_{mn}(E) = N_n(E) \quad (2.49)$$

follows from current conservation. The symmetry of the transmission function in the presence of a magnetic field,

$$T_{nm}(E, B) = T_{mn}(E, -B), \quad (2.50)$$

is a direct consequence of the symmetry of the Schrödinger equation. The Fermi function in lead  $n$  describing the occupation of states at energy  $E$  and temperature  $T$  is

$$f_n(E) = \frac{1}{e^{(E-\mu_n)/k_B T} + 1}, \quad (2.51)$$

where  $\mu_n$  is the chemical potential of electrons in lead  $n$  and  $k_B$  is the Boltzmann constant. We can write the current per unit energy flowing in lead  $n$  as

$$i_n(E) = \frac{2e}{h} \sum_m T_{nm}(E) [f_n(E) - f_m(E)], \quad (2.52)$$

where we sum over all the leads connected to the scattering region. The total current in lead  $n$  is given by the following integral

$$I_n = \int dE i_n(E). \quad (2.53)$$

In the approximation of small bias, i.e., when  $\mu_n - \mu_m \ll \varepsilon_c + \text{few } k_B T$ , where  $\varepsilon_c$  is the energy range over which the transmission function is constant, we have  $f_n(E) - f_m(E) \approx \delta\mu(-\partial f_0(E)/\partial E)$  with equilibrium Fermi function  $f_0(E)$ . Consequently, the total current is

$$I_n = \sum_m G_{nm}(V_n - V_m), \quad (2.54)$$

where  $V_n = \mu_n/e$  and

$$G_{nm} = \frac{2e^2}{h} \int T_{nm}(E) \left( -\frac{\partial f_0(E)}{\partial E} \right) dE. \quad (2.55)$$

If also the temperature is very low (as we will assume in Part I of the thesis), the expression  $(-\partial f_0(E)/\partial E)$  can be approximated by a delta function  $\delta(E - E_F)$ . Hence, the conductance characterizing transport through the scattering region in the limit of small bias and temperature is

$$G_{nm} = \frac{2e^2}{h} T_{nm}(E_F). \quad (2.56)$$

The transmission function  $T_{nm}$  is related to the scattering matrix, which can be calculated directly from the Schrödinger equation by matching wavefunctions at the interface.

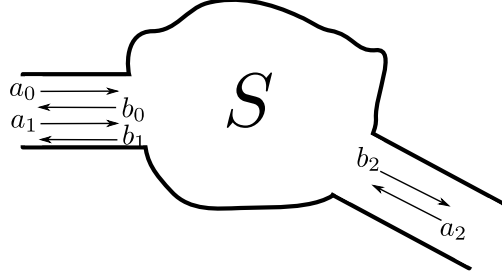


FIGURE 2.7: The scattering region can be characterized by the scattering matrix  $S$  at each energy. Two leads with incoming and outgoing states with amplitudes  $a_\alpha$  and  $b_\alpha$  are connected to the scattering region.

## Scattering matrix

The scattering matrix  $S$  of a system (scattering region) relates the incoming amplitudes to the outgoing amplitudes of the propagating modes in all leads. Let us illustrate it on a simple example of two leads shown in Fig. 2.7, where lead  $L_0$  has two modes and lead  $L_1$  has only one mode. The relation between incoming amplitudes  $a_i$  and outgoing amplitudes  $b_i$  is

$$\begin{pmatrix} b_0 \\ b_1 \\ b_2 \end{pmatrix} = \begin{pmatrix} S_{00} & S_{01} & S_{02} \\ S_{10} & S_{11} & S_{12} \\ S_{20} & S_{21} & S_{22} \end{pmatrix} \begin{pmatrix} a_0 \\ a_1 \\ a_2 \end{pmatrix}, \quad (2.57)$$

where  $S_{ij}$  are the elements of the scattering matrix. It can be calculated directly from the Schrödinger equation by matching the wavefunction in the leads to the wavefunction in the scattering region at energy  $E$ . Numerically, this amounts to solving a large sparse linear system of equations. Clearly,  $S_{ij}$  are the transmission amplitudes in Eq. (2.48). Therefore, the scattering matrix is related to the transmission function by

$$T_{nm}(E) = \sum_{j \in m} \sum_{i \in n} |S_{ij}(E)|^2, \quad (2.58)$$

where the index  $i$  contains all the quantum numbers labeling the transverse modes in lead  $n$ . Hence, once we know the matrix  $S$ , the conductance follows from Eq. (2.56).

In general, the index  $i$  can also contain other quantum numbers than the transverse-mode quantum numbers, such as the electron spin projection. Then,  $S_{\alpha s, \beta s'}$  represents the transmission amplitude from mode  $\beta$  in lead  $m$  with spin  $s'$  to mode  $\alpha$  in lead  $n$  with spin  $s$ . Hence, we can calculate the spin-resolved conductance which allows for studying spin-filtering effects. In this thesis, also other quantum numbers like the valley degree of freedom (Chapter 3) and the electron-hole degree of freedom (Chapter 4) are used to partition the scattering matrix into corresponding blocks.

We employ Kwant [30], the Python package for numerical calculations on tight-binding models, to obtain the scattering matrix in various setups. An example is shown in Appendix A.





## CHAPTER 3

# SWITCHABLE VALLEY FILTER BASED ON A GRAPHENE P-N JUNCTION IN A MAGNETIC FIELD

*The results presented in this chapter were published in*

T. Sekera, C. Bruder, E. J. Mele, and R. P. Tiwari  
*Switchable valley filter based on a graphene p-n junction in a magnetic field*  
Phys. Rev. B **95**, 205431 (2017).

*Minor changes have been made to better embed this work into the thesis.*

Low-energy excitations in graphene exhibit relativistic properties due to the linear dispersion relation close to the Dirac points in the first Brillouin zone. Two of the Dirac points located at opposite corners of the first Brillouin zone can be chosen as inequivalent, representing a new *valley* degree of freedom, in addition to the charge and spin of an electron. Using the valley degree of freedom to encode information has attracted significant interest, both theoretically and experimentally, and gave rise to the field of *valleytronics*. We study a graphene *p-n* junction in a uniform out-of-plane magnetic field as a platform to generate and controllably manipulate the valley polarization of electrons. We show that by tuning the external potential giving rise to the *p-n* junction we can switch the current from one valley polarization to the other. We also consider the effect of different types of edge terminations and present a setup, where we can partition an incoming valley-unpolarized current into two branches of valley-polarized currents. The branching ratio can be chosen by changing the location of the *p-n* junction using a gate.

### 3.1 Introduction

Two-dimensional (2D) materials are promising candidates for future electronics due to their unique characteristics. The pioneering 2D material, graphene, was experimentally isolated in 2004 [2]. The bandstructure of  $p_z$  electrons in single-layer graphene, modeled

as a honeycomb lattice with lattice constant  $a = 0.246$  nm consisting of two triangular Bravais sublattices  $A$  and  $B$  with nearest-neighbor hopping in the tight-binding formulation, hosts six Dirac cones resulting from touching of the valence and conduction bands at the Fermi energy  $E_F = 0$ . Two of the cones located at diagonally opposite corners of the first Brillouin zone can be chosen as inequivalent, for example at  $K = 2\pi/3a$  and  $-K$ . For the low-energy electronic excitations in the system they represent a new degree of freedom of an electron, in addition to the charge and spin. This *valley* degree of freedom can be exploited in analogy with the spin in spintronics, which gave rise to the field called *valleytronics*, where one uses the valley degree of freedom to encode information.

There is a strong motivation to generate, controllably manipulate and read out states of definite valley polarization, and a substantial amount of theoretical and experimental work has been done towards achieving these goals. A recent review of some advances made in the field of valleytronics in 2D materials is provided in Ref. [31]. To mention some: a gated graphene quantum point contact with zigzag edges was proposed to function as a valley filter [21]. Superconducting contacts were shown to enable the detection of the valley polarization in graphene [28]. In 2D honeycomb lattices with broken inversion symmetry, e.g. transition metal dichalcogenide (TMD) monolayers, a non-zero Berry curvature carries opposite signs in the  $K$  and  $-K$  valleys. In these 2D materials, the velocity in the direction perpendicular to an applied in-plane electric field is proportional to this Berry curvature [32]. Hence the electrons acquire a valley-antisymmetric transverse velocity leading to the valley Hall effect, which spatially separates different valley states. In a system where the occupation numbers of the two valleys are different (valley-polarized system), a finite transverse voltage across the sample is developed and the sign of this voltage can be used to measure the valley polarization [33]. The valley Hall effect can also be exploited in a biased bilayer graphene, where the out-of-plane electric field breaks the inversion symmetry [34–36]. Moreover, it was shown that the broken inversion symmetry results in the valley-dependent optical selection rule, which can be used to selectively excite carriers in the  $K$  or  $-K$  valley via right or left circularly polarized light, respectively [37, 38]. Valley polarization can also be achieved in monolayer[39–42] and bilayer[42] graphene systems with barriers. In addition, proposals exploiting strain that induces pseudomagnetic fields acting oppositely in the two valleys[43, 44] together with artificially induced carrier mass and spin-orbit coupling[45] have been put forward.

In this chapter we propose a way to generate and controllably manipulate the valley polarization of electrons in a graphene  $p$ - $n$  junction in the presence of an out-of-plane magnetic field. Applying an out-of-plane magnetic field to the graphene sheet leads to the formation of low-energy relativistic Landau levels (LLs) [46]. These are responsible for the unusual quantum Hall conductance quantization  $G_n = 2_s \times 2_v \times (n + 1/2)e^2/h$ , where the integer  $n$  is the highest occupied Landau level index (for  $n$ -type doping) for a given chemical potential. The factor  $2_s$  in the formula accounts for the spin degeneracy and the second factor  $2_v$  for the valley degeneracy of the LLs. The presence of the  $E = 0$  Dirac point and particle-hole symmetry lead to a special zeroth Landau level (ZLL) for  $n = 0$ , which is responsible for the fraction  $1/2$  in the conductance.

Semiclassically, charged particles propagating in a spatially varying out-of-plane magnetic field in 2D may exhibit snake-like trajectories that are oriented perpendicularly to the field gradient [47]. The simplest case occurs along a nodal line of a spatially varying magnetic field [48–51]. Another system, a graphene  $p$ - $n$  junction in a homogeneous out-of-plane magnetic field, hosts similar states located at the interface between  $n$ - and  $p$ -doped regions. These interface states are also called snake states due to the shape of their semiclassical trajectories [52–54]. A correspondence between these two kinds of snake trajectories was pointed out in Ref. [55]. A mapping between these two systems was found by rewriting both problems in a Nambu (doubled) formulation [56]. In this chapter we consider a graphene  $p$ - $n$  junction in a homogeneous out-of-plane magnetic field, a system which has attracted a lot of attention [57–63]. In the limit of a large junction (where the phase coherence is suppressed due to inelastic scattering or random time-dependent electric fields), the conductance is a series conductance of  $n$ - and  $p$ -doped regions [64]. However, for sufficiently small junctions the conductance depends on the microscopic edge termination close to the  $p$ - $n$  interface. When the chemical potential in the  $n$  and  $p$  regions is within the first Landau gap, i.e., is restricted to energy values smaller than the absolute value of the energy difference between the zeroth and the first Landau level, an analytical formula for the conductance can be derived [65], see Eq. (3.3).

We demonstrate that a three-terminal device like the one shown in Fig. 3.1 can be used as a switchable, i.e. voltage-tunable valley filter. In short, it works as follows: valley-unpolarized electrons injected from the upper lead are collected in the lower leads with high valley polarization. The valley polarization of the collected electrons is controlled by switching the  $p$ - $n$  junction on and off, while the partitioning of the electron density between the two lower leads is controlled by the edge termination and the width  $W$  of the central region close to the  $p$ - $n$  interface.

Our results are not restricted to graphene. They apply also to honeycomb lattices with broken inversion symmetry, where the inversion symmetry breaking term is represented by a staggered sublattice potential. As long as the amplitude of this term is smaller than the built-in potential step in the  $p$ - $n$  junction, our results remain valid. In a system with broken inversion symmetry, a non-zero Berry curvature would give rise to the valley Hall effect which could be used to read out the polarization of the outgoing states [33].

The rest of this chapter is organized as follows. In Sec. 3.2 we describe the setup of the proposed switchable valley filter and the methods we use to investigate its properties in detail. In Sec. 3.3 we present our numerical results, which demonstrate the valley-polarized electronic transport. In Sec. 3.4 we study the effect of potential step height and different edge terminations of the graphene lattice close to the  $p$ - $n$  interface on the valley polarization. We show that using a tilted staircase edge  $p$ - $n$  junction allows to partition a valley-unpolarized incoming current into two outgoing currents with opposite valley polarizations, where the partitioning can be controlled by tuning the location of the  $p$ - $n$  junction. Finally we summarize our results in Sec. 3.5.

### 3.2 Setup

Figure 3.1 shows the three-terminal device that we would like to study. A rectangular region of width  $W$  and length  $L$  represents the graphene  $p$ - $n$  junction in a uniform out-of-plane magnetic field, also referred to as the scattering region. It is described by a tight-binding Hamiltonian of the form

$$H = \sum_i V(\mathbf{r}_i) c_i^\dagger c_i + \sum_{\langle i,j \rangle} t e^{i\varphi_{ij}} c_i^\dagger c_j, \quad (3.1)$$

where  $V(\mathbf{r}_i)$  is the scalar on-site potential at site  $i$  with coordinate  $\mathbf{r}_i$  and  $\varphi_{ij} = (e/\hbar) \int_i^j \mathbf{A} \cdot d\mathbf{r}$  is the Peierls phase accumulated along the link from site  $i$  to site  $j$  in magnetic field  $\mathbf{B} = [0, 0, B]$ . The Zeeman splitting is neglected, i.e., we consider spinless electrons. The sum over  $\langle i, j \rangle$  denotes the sum over nearest neighbors. We choose

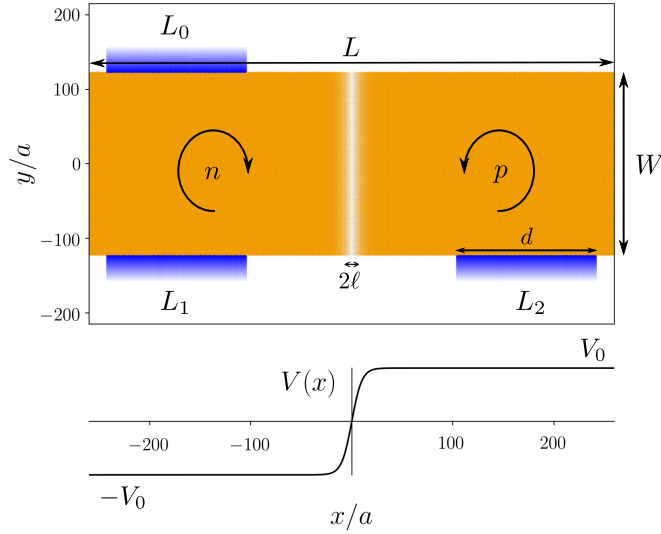


FIGURE 3.1: Three-terminal device used as a switchable valley filter. The three leads of horizontal size  $d$  with zigzag edge termination, upper lead  $L_0$ , lower-left lead  $L_1$  and lower-right lead  $L_2$ , are attached to the rectangular scattering region of length  $L$  and width  $W$ . Top and bottom edges of the scattering region are of armchair type, while the left and right edges are of zigzag type. The  $p$ - $n$  interface of thickness  $2\ell$  (white color gradient) is modeled by an  $x$ -dependent on-site potential  $V(x)$ . In an out-of-plane magnetic field with  $n$  Landau levels occupied ( $n = 0, 1, 2, \dots$ ), there are  $2n + 1$  edge states with opposite chirality in the  $n$ - and  $p$ -doped region. Along the  $p$ - $n$  interface there are  $2(2n + 1)$  co-propagating snake states.

the Landau gauge, where the vector potential is

$$\mathbf{A} = [0, Bx, 0].$$

In this gauge we can define a (quasi-)momentum parallel to the edges of the leads. The leads  $L_0$ ,  $L_1$ , and  $L_2$  are modeled as semi-infinite zigzag nanoribbons, where the valley index can be well distinguished in  $k$ -space. They are also described by the Hamiltonian (3.1) and below we present the case with  $B = 0$  in the leads, which is however not crucial

for our results. The Peierls phase  $\varphi_{ij}$  can be written in the form

$$\varphi_{ij} = 2\pi \frac{\phi}{\phi_0} \frac{2}{\sqrt{3}a^2} \frac{x_i + x_j}{2} (y_j - y_i),$$

where  $\phi_0 = h/e$  is the magnetic flux quantum and  $\phi = BS$  is the flux through a single hexagonal plaquette of a honeycomb lattice. Here,  $S = \sqrt{3}a^2/2$  is the area of a hexagonal plaquette of the honeycomb lattice. An important length scale derived from the magnetic field is the magnetic length  $\ell_B = \sqrt{\hbar/eB}$ . In the rest of the chapter the magnetic field is chosen such that  $\phi/\phi_0 = 0.003$  and hence  $\ell_B \approx 6.78a$ . We also denote the energy difference between the first and the zeroth LL by

$$\delta = \sqrt{2}\hbar v_F/\ell_B, \quad (3.2)$$

where the Fermi velocity at the  $K$  point is  $v_F = \sqrt{3}at/2\hbar$ . For the chosen magnetic field,  $\delta = 0.18t$ .

The scalar on-site potential is varying only in the  $x$ -direction as

$$V(x) = V_0 \tanh(x/\ell),$$

where  $V_0$  is the external scalar potential and  $2\ell$  is the thickness of the domain wall characterizing the  $p$ - $n$  junction. If both  $V_0$  and  $B$  are non-zero and  $V_0 < \delta$  in such a setup, there exist two snake states co-propagating along the  $p$ - $n$  junction [56]. The orientation of the fields in the system is such that the snake states are traveling downwards in the negative  $y$ -direction.

We calculate the transmission  $T_{10}$  from  $L_0$  to  $L_1$ , and  $T_{20}$  from  $L_0$  to  $L_2$ . We also calculate the valley-resolved transmissions, with the following notation:  $T_{20}^{K(-K)}$  is the transmission from  $L_0$  to  $L_2$ , where in  $L_2$  we sum only over outgoing modes with  $k \in (0, \pi/a]$  ( $k \in (-\pi/a, 0]$ ). Then we can define the valley polarization in  $L_2$  as  $P_2 = (T_{20}^K - T_{20}^{-K})/T_{20}$ . Analogous quantities are defined for  $L_1$ .

Due to the absence of backscattering in chiral quantum Hall edge states and the symmetry of the  $p$ - $n$  junction for  $E = 0$ , the net transmission (no spin) is  $T_{10} + T_{20} = 2n + 1$ , where  $n$  is the highest occupied LL in the  $n$ -doped region. The partitioning of the net transmission between  $T_{10}$  and  $T_{20}$  depends on the edge termination close to the  $p$ - $n$  interface according to the formula [65]

$$T_{20} = \frac{1}{2}(1 - \cos \Phi), \quad (3.3)$$

where  $\Phi$  is the angle between valley isospins at the upper and lower edge represented as vectors on the Bloch sphere. For armchair edges one has  $\Phi = \pi$  if  $W/a \bmod 3 = 0$  and  $\Phi = \pm\pi/3$  otherwise. The formula is valid if the  $n$  and  $p$  regions are on the lowest Hall plateau, where the quantum Hall conductances in the  $n$ - and  $p$ -doped regions are equal to  $e^2/h$  (ignoring the spin degree of freedom) [65]. The transmission from  $L_0$  to  $L_1$  is then given by  $T_{10} = 1 - T_{20}$ . Interference between wavefunctions of the snake states is responsible for this partitioning. The snake-state wavefunctions are located at the  $p$ - $n$  interface and their effective spread in the  $x$ -direction is given by the magnetic length  $\ell_B$  to the left and right of the interface. Hence one way to control the partitioning

experimentally will be to control the edge termination around the  $p$ - $n$  interface on a length scale of the order of  $2\ell_B$ .

In the following we show numerically that by switching the  $p$ - $n$  junction on ( $V_0 \neq 0$ ) and off ( $V_0 = 0$ ) we can control the valley polarization of the outgoing states in leads  $L_1$  and  $L_2$ .

### 3.3 Switchable valley filter

We demonstrate the principle of the switchable valley filter using a  $p$ - $n$  junction in an out-of-plane magnetic field, where the upper and the lower edges are of armchair type. The system is described by the Hamiltonian shown in Eq. (3.1). The width  $W$  of the  $p$ - $n$  junction is chosen such that the number of hexagons in this width is a multiple of 3, i.e. such that the corresponding armchair nanoribbon would be metallic. If, furthermore, both the  $n$ - and  $p$ -doped regions are on the lowest Hall plateau and  $V_0$  is large enough [65], we expect  $T_{20} = 1$  and  $T_{10} = 0$ , see Eq. (3.3). The switchable valley filter is based on the fact that for a zigzag graphene nanoribbon the quantum Hall edge states of the ZLL lying in opposite valleys  $K$  and  $-K$  have opposite velocities [46, 66, 67].

Unless stated otherwise, the system has length  $L = 520a$  and width  $W = 246a$  (the exception is Fig. 3.4). The horizontal size of each lead is  $d = 156a$ . The thickness of the  $p$ - $n$  junction is  $2\ell = 20a$ . We set the magnitude of the magnetic field in the leads to zero, which is however not crucial for the result. Our tight-binding calculations were performed using Kwant [30].

First, we consider the case  $V_0 = 0$ . A valley-unpolarized electron current (injected from both valleys) in  $L_0$  ends up as outgoing valley-polarized electron current in  $L_2$ . In Figs. 3.2(a) and 3.3(a) we also plot the probability density of one of the states carrying the current by drawing a black dot on each site whose size is proportional to the probability of finding an electron on that particular site. This is plotted for a state in the scattering region due to an incoming mode from  $L_0$  at Fermi energy  $E$  and with momentum  $k_y$  indicated by the red arrow in the bandstructure for  $L_0$ , see Figs. 3.2(b) and 3.3(b). Figure 3.2(a) shows the probability density of the state in the scattering region due to an incoming mode from  $L_0$  at  $E = \delta/2$  and  $k_y a = 2.08$ . Since  $V_0 = 0$ , there are no snake states in this system and the electronic current is carried by the quantum Hall edge states. The electrons injected from  $L_0$  travel in a clockwise manner to  $L_2$ . The calculated transmissions  $T_{10}$  and  $T_{20}$  and polarizations  $P_1$  and  $P_2$  are shown in the inset table in Fig. 3.2(a). We find that the outgoing electrons in  $L_2$  are perfectly polarized in the  $K$  valley. This shows the valley-polarized nature of the zeroth LL. Thus, this system can be used as a valley filter.

If we now turn on the  $p$ - $n$  junction, the situation will change. We assume that the  $p$ - $n$  junction is turned on adiabatically. We choose  $V_0 = \delta/2$ , so that the  $n$ - and  $p$ -doped regions are on the ZLL. Figure 3.3(a) shows the probability density of the state in the scattering region due to the incoming mode from  $L_0$  at the Fermi energy  $E = 0.001t$  and with  $k_y a = 2.08$  (red arrow in the inset of Fig. 3.3(b)). In this system there are two co-propagating snake states along the  $p$ - $n$  interface, and the electronic current is

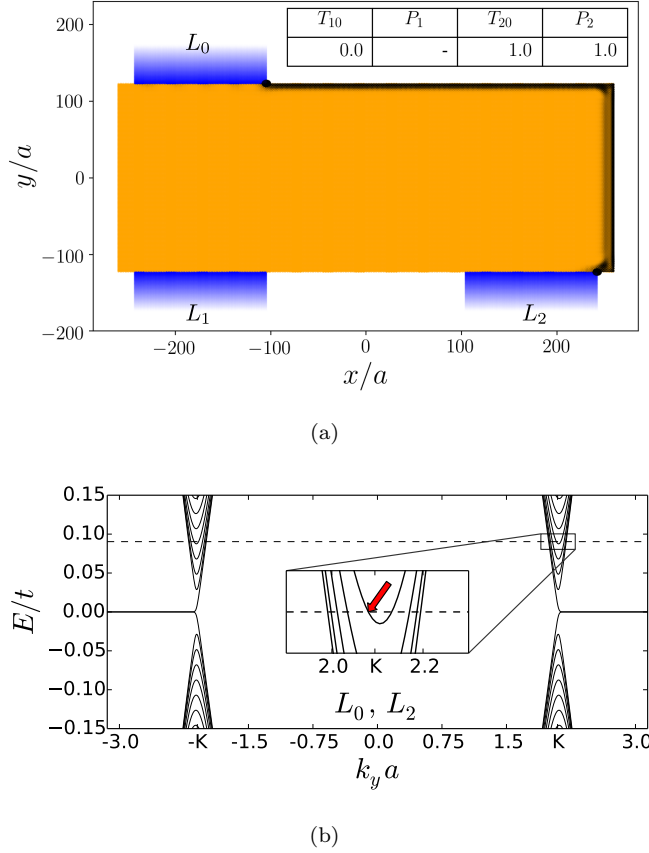


FIGURE 3.2: Case when  $V_0 = 0$  and  $E = \delta/2$ . (a) State in the scattering region due to incoming mode from lead  $L_0$  with  $k_y a = 2.08$ . The inset table lists the transmissions  $T_{10}$  and  $T_{20}$  and polarizations  $P_1$  and  $P_2$ . (b) Bandstructure of leads  $L_0$  and  $L_2$ . The Fermi energy is indicated by the horizontal dashed line. The red arrow indicates the incoming mode on lead  $L_0$  which has velocity  $v < 0$  and is chosen to be plotted in (a).

carried by these states. These snake states are located at the  $p$ - $n$  interface and spread in the  $\pm x$ -direction over the magnetic length  $l_B$ , which is independent of the domain wall thickness  $2\ell$ .

The electrons injected from  $L_0$  now travel along the upper edge in the  $n$  region towards the  $p$ - $n$  interface and continue along the  $p$ - $n$  interface towards the lower edge, where they enter the  $p$  region with probability  $\approx 1$  due to the specifically chosen  $W$  and the armchair edge termination at both ends of the interface. Finally, they end up in  $L_2$ . The corresponding transmissions and polarizations are shown in the inset table of Fig. 3.3(a). We find that the electrons in  $L_2$  are nearly perfectly polarized in the  $-K$  valley. Thus, by turning on the  $p$ - $n$  junction we have *flipped* the valley polarization of the electronic current in  $L_2$ .

It is worth noting that these results are robust with respect to edge disorder because of the absence of backscattering in the chiral quantum Hall edge states. Our results also apply to the case where the magnetic field is present in the leads. However, since for low energies and dopings, only the ZLL plays a role, states in the leads are already valley-polarized edge states and thus our three-terminal device would then work as a perfect valley switch.

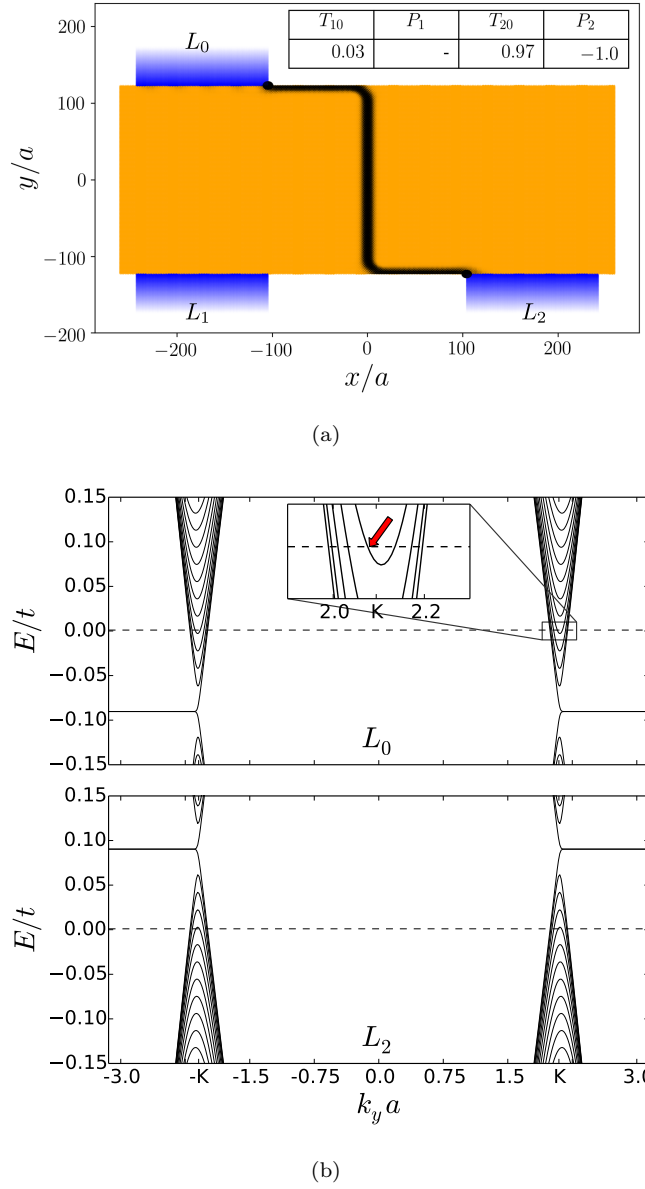


FIGURE 3.3: Case when  $V_0 = \delta/2$  and  $E = 0.001t$ . (a) State in the scattering region due to incoming mode from lead  $L_0$  with  $k_y a = 2.08$ . The inset table lists the transmissions  $T_{10}$  and  $T_{20}$  and polarizations  $P_1$  and  $P_2$ . (b) Top: bandstructure of lead  $L_0$ . The Fermi energy is indicated by the horizontal dashed line. The red arrow indicates the incoming mode chosen to plot (a). Bottom: bandstructure of lead  $L_2$ .

### 3.4 Polarizations and transmissions upon varying potential step height and geometry

In the following we analyze how the valley polarizations  $P_1$  and  $P_2$  and transmissions  $T_{10}$  and  $T_{20}$  change upon varying  $V_0$  and edge terminations.

*Polarization vs.  $V_0$ .* In Fig. 3.4 we plot the polarization in the leads as a function of  $V_0$ . Let us focus on  $P_2$ , because the majority of electrons are traveling into lead  $L_2$  (for this specifically chosen scattering region). The case shown in Fig. 3.2 corresponds to  $V_0 = 0$ ,



where  $P_2 = 1$  (not visible in the figure). For  $V_0 > 0$  (Fig. 3.3), the polarization in lead  $L_2$  changes sign,  $P_2 = -1$ . For  $0 < V_0 < \delta = 0.18t$  only the ZLL valley-polarized edge states contribute to the transport and  $P_2$  stays close to  $-1$  until  $V_0 \approx \delta$ . For  $V_0 > \delta$  the higher LLs get occupied. Edge states in the higher LLs are not valley-polarized which reduces  $P_2$ . On further increasing  $V_0$  higher and higher LLs get occupied which further obscures the edge state valley polarization of the ZLL and the magnitude of  $P_2$  decreases. The population of the LLs can be seen from  $T_{10} + T_{20}$  as a function of  $V_0$ , which is shown with the red curve in Fig. 3.4. Hence the efficiency of the switchable valley filter device is observed to decrease with an increase in  $V_0$ , i.e. with populating higher LLs.

Furthermore, one can notice in Fig. 3.4 that the valley polarizations  $P_1$  and  $P_2$  in leads  $L_1$  and  $L_2$  jump at the same voltages  $V_0$ , where the  $p$ - $n$  junction undergoes quantum Hall transitions and the total transmission  $T_{10} + T_{20}$  changes by 2. The larger  $V_0$ , the more the values of  $V_0$  at which the total transmission changes by 2 deviate from the vertical lines indicating the LL energies at  $E_n = \sqrt{2n}\hbar v_F/\ell_B$ . This is due to the nonlinearity of the dispersion which leads to a change in group velocity. The oscillations seen in the blue and green curves stem from oscillations of transmissions as shown in Fig. 3.5. This can be viewed as a consequence of interference effects between modes confined at the  $p$ - $n$  interface with different momenta[60, 68]. However, the amplitude of these oscillations decreases with increasing system size. In our simulations, the system size is increased proportionally, i.e. parameters  $L, W, d$  and  $\ell$  are multiplied by  $\alpha = 1, 1.5, 4$ , while the magnetic flux per plaquette is kept constant,  $\phi/\phi_0 = 0.003$  (see Fig. 3.5).

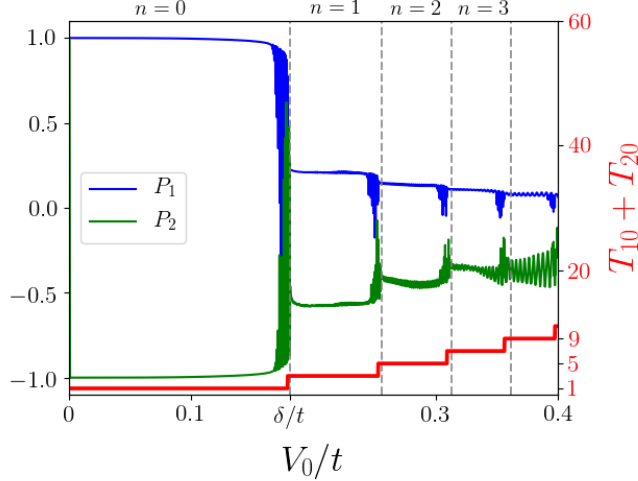


FIGURE 3.4: Polarization  $P_1$  in lead  $L_1$  (blue, left axis), and  $P_2$  in lead  $L_2$  (green, left axis) as a function of  $V_0$  for the device shown in Fig. 3.1. For  $0 < V_0 < \delta$  only the zeroth Landau level (LL) is occupied and  $P_2 \approx -1$ . As soon as higher LLs get involved ( $V_0 > \delta$ ), where the edge states are not valley-polarized, the valley polarization in  $L_1$  and  $L_2$  decreases towards 0 with increasing  $V_0$ . The sum of the transmissions  $T_{10} + T_{20}$  (red step-like curve, right axis) exhibits quantization due to LLs in the scattering region. The device is a good valley filter for  $V_0 < \delta$ , i.e., when only the zeroth LL is occupied. Vertical (grey dashed) lines mark the LL energies  $E_n = \sqrt{2n}\hbar v_F/\ell_B$  in the  $n$ -doped region calculated for a linear Dirac dispersion. The parameters chosen for this figure are  $L = 2080a$ ,  $W = 984a$ ,  $\ell = 40a$ , and  $d = 320a$ .

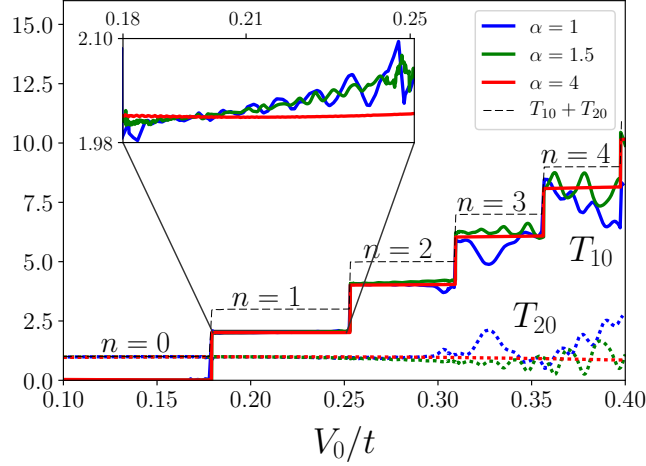


FIGURE 3.5: Transmissions  $T_{10}$  (solid lines),  $T_{20}$  (dotted lines) and  $T_{10} + T_{20}$  (dashed line) as a function of  $V_0$  for different system sizes. The inset shows that the amplitude of the oscillations tend to vanish as we increase the system size, which is accomplished by multiplying the parameters  $L, W, d$  and  $\ell$  by a factor of  $\alpha = 1$  (blue), 1.5 (green), 4 (red) while  $\phi/\phi_0 = 0.003$  is kept constant.

*Different edge terminations.* We find that different edge terminations and  $p$ - $n$  interface length have almost no influence on the valley polarization in the leads, but they determine the partitioning of the net transmission between  $T_{10}$  and  $T_{20}$ . In Tab. 3.1(a), where the  $p$ - $n$  interface meets armchair edges,  $T_{10}$  and  $T_{20}$  exhibit the expected periodicity when changing the width  $W$  such that the number of hexagons across the width of the scattering region changes by 3. The case in which the  $p$ - $n$  interface meets zigzag edges is considered in Tab. 3.1(b). Here, the transmissions  $T_{10}$  and  $T_{20}$  switch values depending on whether the two edges are in zigzag or anti-zigzag configuration, which is in agreement with Ref. [69]. To model different edge terminations, we also added a triangular region to the sample, see Tab. 3.1(c)–(e) (a zoom-in onto the tip is shown in the last column of Tab. 3.1(c)). Thus by controlling the edge termination on a length scale of  $2\ell_B$  around the  $p$ - $n$  interface one can tune the partitioning of the current into  $L_1$  and  $L_2$ . The currents in both of these leads are polarized in opposite valleys. Thus if one chooses the situation where the current is finite in both  $L_1$  and  $L_2$  (for example the case shown in Tab. 3.1(c)), one can create two streams of oppositely valley-polarized currents in leads  $L_1$  and  $L_2$ .

*Tilted staircase edge.* Now we consider the three-terminal setup shown in Fig. 3.6. The upper edge has many steps on the atomic scale, shown in the upper panel of Fig. 3.6. The size of each of these steps is assumed to be constant and is denoted by  $\ell_{\text{step}}$ . The bottom-edge termination of the sample is of armchair type. We study the transmission  $T_{20}$  as a function of the position of the  $p$ - $n$  interface  $x_0$ . Note that  $T_{10} = 1 - T_{20}$ , because here the parameters are such that only the ZLL contributes to the electronic transport. If  $\ell_{\text{step}} \gg 2\ell_B$ , the transmission  $T_{20}$  shows a plateau-like behavior (see Fig. 3.7(a)). The transmission jumps to a different plateau as a new step is encountered while moving  $x_0$  from  $-180a$  to  $180a$  (the jump happens on length scales of the order of  $2\ell_B$ ). Since the upper and the lower edges are of armchair type, we observe three plateau values corresponding to different angles the between valley isospins at the two

	geometry	$T_{10}$	$P_1$	$T_{20}$	$P_2$	notes
(a)		0.03	–	0.97	-1	$W = 246a$
		0.6	0.99	0.4	-0.99	$W = 247a$
		0.88	1	0.12	-1	$W = 248a$
(b)		0.0	–	1.0	-0.93	$L = 520a$
		1.0	0.93	0.0	–	$L = 521a$
(c)		0.48	1	0.52	-1	
(d)		1	1	0	–	W independent
(e)		0.02	–	0.98	-1	W independent

TABLE 3.1: Transmissions  $T_{10}$  and  $T_{20}$  and polarizations  $P_1$  and  $P_2$  for different devices. The first column shows different sample geometries where the dashed line denotes the  $p$ - $n$  interface. (a) Transmissions for three different widths  $W$  for the same geometry as in Fig. 3.1, i.e. the  $p$ - $n$  interface meets armchair edges. The partitioning of the net transmission between  $T_{10}$  and  $T_{20}$  is a periodic function of  $W$  with period  $3a$  (or three hexagons across the width of the scattering region). (b) The  $p$ - $n$  interface meets edges of zigzag type. The two rows describe the zigzag/anti-zigzag configuration which lead to a different partitioning of the transmission. Note the changed position of the leads. (c) A triangular region is added to the lower edge (a zoom-in onto the tip is shown in the last column) to model different edge terminations. (d)–(e) Triangular regions added to the top and bottom edge. When the transmission to a particular lead is negligible, the polarization in this lead is not shown (long dash).

edges  $\Phi = \pi, \pm\pi/3$ , in agreement with Ref. [65]. The width of these plateaus corresponds to  $\ell_{\text{step}}$ . In the regime  $\ell_{\text{step}} \lesssim 2\ell_B$  there is a qualitative change from the plateau-like to sine-like behavior of  $T_{20}$ , see Fig. 3.7(b). Thus, when  $\ell_{\text{step}} \lesssim 2\ell_B$ , the incoming current in  $L_0$  can be partitioned into valley-polarized currents in  $L_1$  ( $K$  valley) and  $L_2$  ( $-K$  valley) in any desired ratio by tuning the location of the  $p$ - $n$  junction. When  $\ell_{\text{step}} \lesssim 2\ell_B$ , mixing of Landau orbits on neighboring guiding centers gives rise to the conductance behavior shown in Fig. 3.7(b). Our results are in agreement with the simulations in Ref. [70].

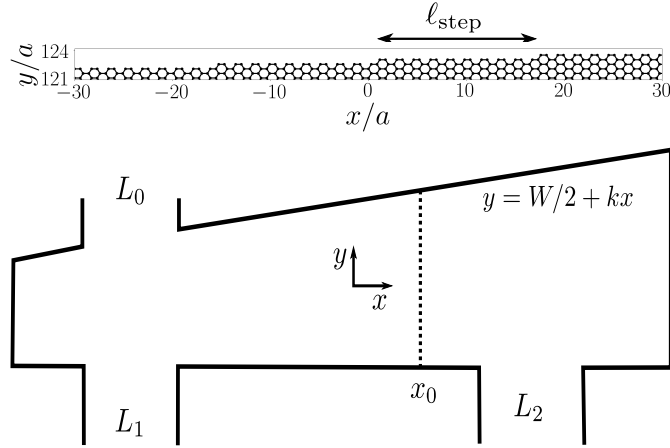
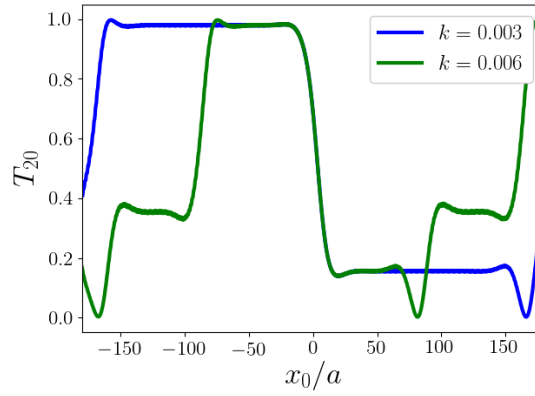
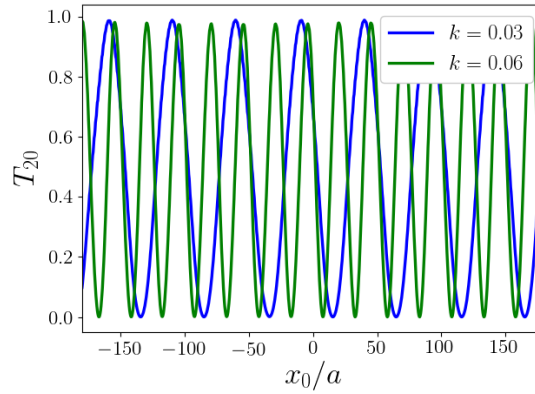


FIGURE 3.6: Geometry of a device with a tilted staircase edge. Upper panel: zoom-in onto a part of the tilted upper edge displaying the staircase. The step length (length of the region of constant width  $W$ ) is denoted by  $\ell_{\text{step}}$ . Lower panel: a schematic of the device. The slope of the tilted edge  $k$  is related to  $\ell_{\text{step}}$ , e.g.  $k = 0.003$  corresponds to  $\ell_{\text{step}} \approx 166a$  while  $k = 0.03$  corresponds to  $\ell_{\text{step}} \approx 16a$ .



(a)



b

FIGURE 3.7: Transmission  $T_{20}$  in a device with a tilted staircase edge as a function of the position of the  $p$ - $n$  interface  $x_0$  for different values of the slope  $k$ , see Fig. 3.6. (a) Plateau-like behavior of  $T_{20}$  as expected for  $\ell_{\text{step}} \gg 2\ell_B$ . (b) Sine-like behavior of  $T_{20}$  for  $\ell_{\text{step}} \lesssim 2\ell_B$ . In this figure  $L = 780a$ .

In an experiment, one could measure the resulting valley polarization by utilizing the valley Hall effect [33]. This would require breaking the inversion symmetry, which can be modeled by a staggered sublattice potential of the form  $\pm\lambda_\nu \sum_i c_i^\dagger c_i$  in our system. Our results remain valid even after adding such a term to the Hamiltonian in Eq. (3.1) as long as  $\lambda_\nu < V_0$ . This condition ensures the presence of snake states in the system at  $E \approx 0$ .

### 3.5 Conclusion

In summary, we have demonstrated that a graphene  $p$ - $n$  junction in a uniform out-of-plane magnetic field can effectively function as a switchable valley filter. The valley polarization of the carriers in the outgoing leads is quite robust. Changing the edge termination at the  $p$ - $n$  interface can drastically modify the partitioning of the current into the two outgoing leads, but the outgoing current in both leads remains valley-polarized. We have also shown that in a device where one of the edges has many steps on the atomic scale, the partitioning of the current into two outgoing leads can be tuned by choosing the *location* of the  $p$ - $n$  junction. In such a device it will be possible to partition a valley-unpolarized incoming current into two streams of oppositely valley-polarized currents in two outgoing leads in any desired ratio.



## CHAPTER 4

# INTERFACE BETWEEN GRAPHENE AND SUPERCONDUCTOR

A superconducting electrode placed on top of a graphene sheet will induce a nonzero superconducting pairing  $\Delta(\mathbf{r})$  in the sheet via the proximity effect [71–73]. In this chapter, we will treat for simplicity the spatial dependence of the pair potential  $\Delta(\mathbf{r})$  as a step function, i.e., it is a non-zero constant in the graphene sheet under the superconducting electrode and zero otherwise. We adopt the following terminology. The term two-dimensional electron gas (2DEG) is used for a material that has energy dispersion near the bottom of the conduction band proportional to  $p^2$  and can be modeled by a tight-binding Hamiltonian with a nearest-neighbor hopping on a square lattice, like the 2DEG formed in AlGaAs/GaAs heterostructures. The corresponding junction with a superconductor is abbreviated as NS. On the other hand, *graphene* has low-energy excitation energies near the Dirac point linear in  $p$  and is modeled by a tight-binding Hamiltonian with a nearest-neighbor hopping on a honeycomb lattice. The junction between graphene and superconductor is abbreviated as GS. We use the term normal metal for both 2DEG and graphene in the normal (non-superconducting) state.

### 4.1 Semiclassical discussion of Andreev reflection in graphene

An electron is incoming from a normal metal onto the interface with a superconductor at energy  $E > 0$  (measured from the Fermi energy  $E_F$ ), that is within the superconducting gap  $\Delta$ . It can enter the superconductor only by forming a Cooper pair with another electron at energy  $-E$  with opposite spin and opposite momentum taken from the normal metal Fermi sea (FS). The result of this process, called *Andreev reflection*, is a normal metal FS with a missing electron, i.e., with a hole.

Below we summarize the properties of the hole excitation in relation to the properties of the electron taken from the FS (the missing electron):

- If the charge of the missing electron is  $q_e = -e$ , the charge of the hole is  $q_h = +e$ .

- If the spin of the missing electron is  $s_e$ , the spin of the hole is  $s_h = -s_e$ .
- If the net momentum of the FS is zero and the momentum of the electron taken from the FS is  $\hbar\mathbf{k}_e$ , the momentum of the hole is  $\hbar\mathbf{k}_h = -\hbar\mathbf{k}_e$ .
- The energy of the FS upon removing an electron is changed by  $-E_e(\mathbf{k}_e)$ . Therefore, the energy of the hole is  $E_h(\mathbf{k}_h) = -E_e(\mathbf{k}_e)$ .

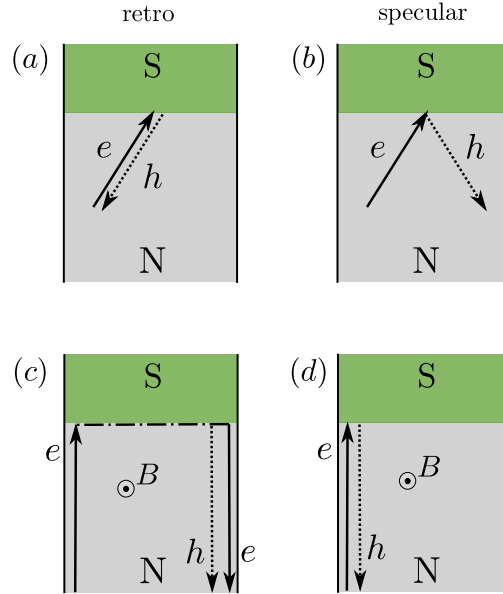


FIGURE 4.1: (a) Andreev retro-reflection and (b) Andreev specular reflection at the interface between a normal metal (N) and a superconductor (S) in the absence of a magnetic field. (c-d) The same in the quantum Hall regime. Semiclassical electron and hole trajectories are marked by solid and dotted line, respectively. The state propagating along the interface in (c) is of mixed electron-hole character (dash-dotted line).

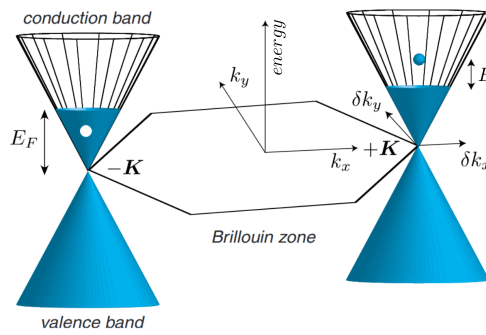


FIGURE 4.2: An electron from the valence band at energy  $E_F + E$  in one valley can be converted to a hole with energy  $E_F - E$  in the opposite valley via Andreev reflection. The Andreev retro-reflection case is shown, when  $E < E_F$ . Adapted from Ref. [67].

In a 2DEG, the reflected hole retraces the path of the incoming electron, as shown in Fig. 4.1(a). However, in the case of graphene, a specular reflection is possible [74]. Let us fix  $E_F > 0$ . For  $E < E_F$ , as illustrated in Fig. 4.2, the usual retro-reflection occurs, since the Andreev-reflected hole is in the same (conduction) band as the incoming electron.



On the other hand, when  $E > E_F$ , the hole is in the valence band and this leads to a specularly reflected hole as in Fig. 4.1(b).

This picture becomes quite different when we switch on the out-of-plane magnetic field and enter the quantum Hall regime in graphene. Here, the retro-reflection case ( $E < E_F$ ) yields the so-called Andreev edge states propagating along the interface with the superconductor, Fig. 4.1(c). In graphene, the probability of the state leaving the interface to be of an electron or hole character depends on the valley structure of the edge states within the distance of the order of magnetic length  $\ell_B$  away from the interface [28]. This probability is different for a 2DEG as discussed in Sec. 4.4. In the case of specular reflection ( $E > E_F$ ), the electron incoming onto the GS interface is Andreev reflected from the interface into the counter-propagating hole edge state, Fig. 4.1(d). In Sec. 4.5 we examine a situation in the presence of a Zeeman field that splits the zeroth Landau level (ZLL) into two, and we find that both, retro- and specular Andreev reflection takes place which leads to a spin filtering effect in a three-terminal setup.

## 4.2 Bogoliubov-De Gennes Hamiltonian

The quantum-mechanical description of Andreev reflection is provided by the Bogoliubov-De Gennes (BdG) Hamiltonian. The BdG Hamiltonian in real space can be derived from the standard Bardeen-Cooper-Schrieffer (BCS) Hamiltonian in momentum space

$$H = \sum_{\mathbf{k}s} \varepsilon_{\mathbf{k}} c_{\mathbf{k}s}^\dagger c_{\mathbf{k}s} + \frac{1}{2\Omega} \sum_{\mathbf{k}\mathbf{k}'qss'} V c_{\mathbf{k}+q,s}^\dagger c_{\mathbf{k}'-q,s'}^\dagger c_{\mathbf{k}',s'} c_{\mathbf{k},s}, \quad (4.1)$$

where  $\varepsilon_{\mathbf{k}}$  is the energy dispersion of free electrons,  $V$  is the effective electron-electron interaction,  $\Omega$  is the volume and  $c_{\mathbf{k}s}^\dagger$  ( $c_{\mathbf{k}s}$ ) is the creation (annihilation) operator for an electron with momentum  $\mathbf{k}$  and spin  $s$ . We introduce the field operators (linear combinations of  $c_{\mathbf{k}s}, c_{\mathbf{k}s}^\dagger$ )

$$\begin{aligned} \psi_s^\dagger(\mathbf{x}) &= \sum_{\mathbf{k}} \varphi_{\mathbf{k}}^*(\mathbf{x}) c_{\mathbf{k}s}^\dagger, \\ \psi_s(\mathbf{x}) &= \sum_{\mathbf{k}} \varphi_{\mathbf{k}}(\mathbf{x}) c_{\mathbf{k}s}, \end{aligned} \quad (4.2)$$

where  $\varphi_{\mathbf{k}}(\mathbf{x})$  is the wavefunction of the state with momentum  $\mathbf{k}$ . Then, one can rewrite Eq. (4.1) within the mean-field approximation as

$$H = \int d^3\mathbf{x} \begin{pmatrix} \psi_\uparrow^\dagger(\mathbf{x}) & \psi_\downarrow(\mathbf{x}) \end{pmatrix} \begin{pmatrix} h(\mathbf{x}) - E_F & \Delta(\mathbf{x}) \\ \Delta^*(\mathbf{x}) & E_F - \mathcal{T}h(\mathbf{x})\mathcal{T}^{-1} \end{pmatrix} \begin{pmatrix} \psi_\uparrow(\mathbf{x}) \\ \psi_\downarrow^\dagger(\mathbf{x}) \end{pmatrix} + \text{const..} \quad (4.3)$$

Here, the electron and hole wavefunctions are coupled via the superconducting pair potential  $\Delta(\mathbf{x}) = V(\mathbf{x}) \langle \psi_\downarrow(\mathbf{x}) \psi_\uparrow(\mathbf{x}) \rangle$  and  $\mathcal{T}$  is the time-reversal operator.  $h(\mathbf{x})$  is the single-particle Hamiltonian of a normal metal. The last term is just a constant, independent of creation and annihilation operators. In the rest of the thesis we assume constant and real  $\Delta(\mathbf{x}) = \Delta$  in the S region and  $\Delta(\mathbf{x}) = 0$  in the N region.

The nearest-neighbor tight-binding approximation on a discrete lattice leads to the following form of the BdG Hamiltonian:

$$H = H_0 + H_\Delta, \quad (4.4)$$

where

$$\begin{aligned} H_0 = & \sum_{\langle ij \rangle} \psi_i^\dagger \left[ -te^{i\varphi_{ij}} \frac{1}{2}(\rho_0 + \rho_z) + te^{-i\varphi_{ij}} \frac{1}{2}(\rho_0 - \rho_z) \right] \otimes s_0 \psi_j + \\ & + \sum_i \psi_i^\dagger (-(E_F + V)\rho_z \otimes s_0) \psi_i, \\ H_\Delta = & \sum_i \psi_i^\dagger (\Delta \rho_x \otimes s_0) \psi_i. \end{aligned} \quad (4.5)$$

The four-spinor field  $\psi_i$  is in the standard Nambu basis  $\psi_i = (c_{i\uparrow}, c_{i\downarrow}, c_{i\downarrow}^\dagger, -c_{i\uparrow}^\dagger)^T$ , where  $\psi_i^\dagger$  creates a particle localized at site  $i$  with a four component wavefunction  $(\varphi_{e\uparrow}(\mathbf{r} - \mathbf{r}_i), \varphi_{e\downarrow}(\mathbf{r} - \mathbf{r}_i), \varphi_{h\uparrow}(\mathbf{r} - \mathbf{r}_i), -\varphi_{h\downarrow}(\mathbf{r} - \mathbf{r}_i))^T$ . Here  $es$  ( $hs$ ) is for an electron (hole) with spin  $s \in \{\uparrow, \downarrow\}$ . Two sets of Pauli matrices  $\rho_\mu$  and  $s_\mu$  with  $\mu \in \{0, x, y, z\}$  describe the electron-hole and spin degree of freedom, respectively.  $\sum_{\langle ij \rangle}$  is the sum over the nearest neighbors.

The first (second) term in  $H_0$  represents the nearest-neighbor hopping of electrons (holes) in an out-of-plane magnetic field with hopping amplitude  $-te^{i\varphi_{ij}}$  ( $te^{-i\varphi_{ij}}$ ). The third term in  $H_0$  represents the Fermi energy  $E_F$  in the system. For undoped graphene,  $E_F = 0$ .  $V$  describes the doping of the superconductor with respect to the normal region, i.e.,  $V = V_0$  in the S region and  $V = 0$  in the N region. We may require  $V_0 + E_F \gg \Delta$  to satisfy the mean-field condition for superconductivity. The s-wave superconducting pairing is represented by  $H_\Delta$  and couples an electron with spin  $s$  to a hole with spin  $s$  on the same lattice site.

We assume a step function profile for the magnetic field  $\varphi_{ij} = 0$ , if  $i, j \in S$  and nonzero otherwise, as well as for the superconducting pair potential  $\Delta(\mathbf{r}_i) = \Delta$ , if  $i \in S$  and zero otherwise.

### 4.3 Two-terminal conductance across graphene-superconductor junction

We use the tight-binding model (4.4) to simulate two-terminal transport in a graphene-superconductor (GS) junction. In this section we investigate the situation in the absence of magnetic fields where the Peierls phase is zero. We numerically calculate the scattering matrix, from which we obtain the two-terminal differential conductance  $dI/dV$  at energy  $E$  across the GS junction given by [75]

$$dI/dV = (N - R_{ee} + R_{he})e^2/h. \quad (4.6)$$

Here  $N$  is the number of electron modes in the normal region at energy  $E$ ,  $R_{ee}$  is the normal reflection coefficient and  $R_{he}$  is the Andreev reflection coefficient at energy  $E$ .

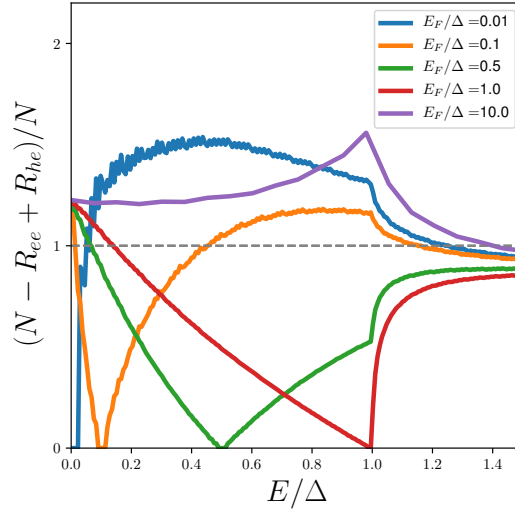


FIGURE 4.3: Differential conductance of the NS interface normalized by the number of transverse modes  $N$  as a function of energy for  $E_F/\Delta = 0.01, 0.1, 0.5, 1, 10$ . The curves are smooth if  $N \gg 1$ . Doping of the superconductor is  $V_0 = 0.5t$ .

In Fig. 4.3 we plot the differential conductance normalized to the normal-state ballistic value. Andreev retro-reflection occurs when  $E < E_F$  and its probability  $R_{he}$  decreases with increasing energy simply because the hole density of states (DOS) decreases towards the Dirac point. Once  $E = E_F$ , the differential conductance vanishes and  $R_{he} = 0$ , since the hole DOS is zero at the Dirac point and there is no hole excitation available for the Andreev reflection. Therefore, the incoming electron has to be reflected as an electron and  $R_{ee} = N$ . For  $E > E_F$ , specular Andreev reflection occurs, and the differential conductance increases with increasing energy. For  $E \gg \Delta$ , the differential conductance approaches a value that is in general smaller than the normal ballistic value  $Ne^2/h$  as a result of the Fermi wavelength mismatch due to the doping of the superconductor given by  $V_0$ . As  $V_0 \rightarrow 0$ , the differential conductance curves approach  $Ne^2/h$  for  $E \gg \Delta$ . The curves have qualitatively the same profile for different  $V_0$ , but the value of the differential conductance is overall suppressed as  $V_0$  is increased.

The larger the Fermi energy, the larger the number of transverse modes  $N$ . For  $N \gg 1$  the curves become smooth, while for smaller  $N$ , the quantization of the transverse modes becomes apparent (visible for  $E_F/\Delta = 0.01$  and  $0.1$  in Fig. 4.3).

Our results based on the tight-binding Hamiltonian (4.4) are in agreement with the analytical calculation of Ref. [74], where the continuum model for graphene is used, and the scattering matrix is found by matching the wavefunctions at the interface with a proper boundary condition.

From an experimental point of view, it is worth noting that the major drawback preventing observation of the specular Andreev reflection in monolayer graphene are Fermi energy fluctuations (so-called electron-hole puddles) on the order of  $\Delta$ . Such fluctuations are suppressed in bilayer graphene, where the DOS is large in the vicinity of the Dirac point. This means that the same carrier density fluctuations result in smaller Fermi energy fluctuations in bilayer than monolayer. The signature of specular Andreev

reflections (the dip in the differential conductance at  $E = E_F$ ) was first observed in bilayer graphene [76]. Direct observation of the specular reflection in monolayer graphene is still lacking.

#### 4.4 Two-terminal magnetoconductance across normal metal-superconductor junctions in the quantum Hall regime

Superconductivity and the quantum Hall effect are two seemingly contradictory phenomena: the first one requires small enough magnetic fields to survive, while the second one requires high enough fields for Landau levels (LLs) to develop. Recent experiments demonstrate the possibility of the coexistence of the two [77, 78]. In this section we omit the spin of an electron, while the effect of the spin degeneracy lifting is discussed in Sec. 4.5.

In an Andreev reflection process, electron edge states propagating towards the GS interface are converted into hole edge states propagating away from the interface, which is manifested in an experiment by a negative (electronic) chemical potential of the carriers leaving the interface. Graphene is an especially good material for the realization of this hybrid system because of two reasons. On the one hand, it provides a good electric contact with conventional metallic superconductors [71–73], which results in significant Andreev reflection probabilities. On the other hand, graphene has well-developed LLs for relatively weak magnetic fields. Namely, the gap between the two lowest LLs in graphene is  $\Delta E_G = 36\sqrt{B}$  meV/ $\sqrt{\text{T}}$ , while in, e.g., GaAs it is  $\Delta E_{\text{GaAs}} = 1.7B$  meV/T [79]. This amounts to the ratio  $\Delta E_G/\Delta E_{\text{GaAs}} \approx 6.7$  at  $B = 10$  T.

##### NS junction

Semiclassically, an electron in a strong magnetic field has a circularly curved trajectory due to the Lorentz force. When this trajectory is in the vicinity of the sample edge, it has the character of a skipping orbit. If the trajectory is close the interface with a superconductor and the Andreev reflection has nearly unit probability, the skipping orbit has an alternating electron-hole character.

However, quantum mechanically, the picture is as follows. When only a single LL is occupied in the 2DEG, there are two states of mixed electron-hole character at the interface marked  $|+\rangle$  and  $|-\rangle$  in Fig. 4.4(a). Their interference leads to an oscillatory pattern of the AR probability as a function of magnetic flux, see Fig. 4.5. This can be understood from the following [80]. Consider the NS junction shown in Fig. 4.4(c). Assuming that particles move ballistically in the edge states, the net scattering matrix is composed of three terms

$$S = T_2 \Lambda T_1, \quad (4.7)$$

where  $T_1$  is the scattering matrix from the left edge to the NS interface,  $\Lambda$  describes the ballistic propagation along the interface and  $T_2$  is the scattering from the interface to the right edge. If the transport is within the ZLL, there is only one electron and one

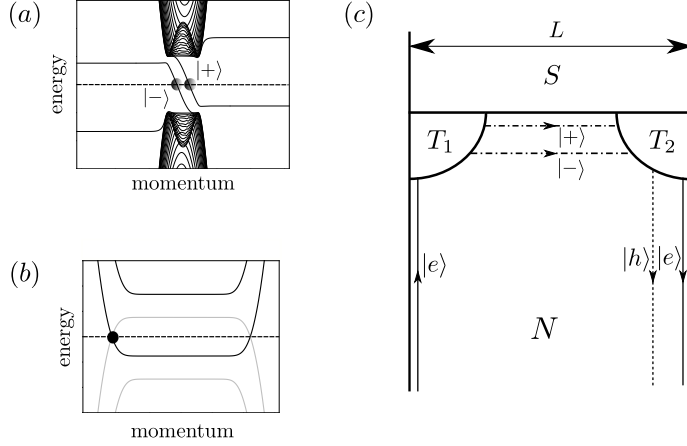


FIGURE 4.4: (a) Band structure of excitations propagating along a translationally invariant NS interface. Two Andreev edge states  $|+\rangle$  and  $|-\rangle$  (circles) of mixed electron-hole character at the Fermi energy (dashed line) are shown. These evolve into flat Landau levels far away from the interface. The bulk bands of the S region with a gap are also visible. (b) Band structure of electrons (black) and holes (grey) in the N region. The electron state marked with a black circle propagates along the left edge towards the NS interface as shown in (c). (c) Sketch of an NS junction with interface length  $L$ . The incoming electron is scattered into two Andreev edge states  $|+\rangle$  and  $|-\rangle$  described by scattering matrix  $T_1$ . After traveling along the interface, the particle is scattered into an outgoing electron or hole state described by  $T_2$ .

hole mode in the N region and these 2x2 matrices can be expressed as

$$T_1 = \begin{pmatrix} t_{+e} & t_{+h} \\ t_{-e} & t_{-h} \end{pmatrix}, \quad \Lambda = \begin{pmatrix} e^{ik_+L} & 0 \\ 0 & e^{ik_-L} \end{pmatrix}, \quad T_2 = \begin{pmatrix} t_{e+} & t_{e-} \\ t_{h+} & t_{h-} \end{pmatrix}, \quad (4.8)$$

where  $t_{\beta\alpha}$  is the matrix element describing scattering from state  $\alpha$  to state  $\beta$ ,  $k_{+(-)}$  is the momentum along the idealized translationally-invariant interface associated with state  $|+\rangle$  ( $|-\rangle$ ).  $L$  is the length of the NS interface and  $L \gg \xi$ , where  $\xi = \hbar v_F / \Delta$  is the superconducting coherence length with the Fermi velocity  $v_F$ . We assume a mirror symmetric junction (in the presence of a magnetic field), which means that  $T_1 = T_2^T$ . If the incoming electron energy  $E$  is less than  $\Delta$ , the scattering matrix is unitary and the AR probability can be expressed as

$$R_{he} = |\langle h | T_2 \Lambda T_1 | e \rangle|^2 = 2\tau(1 - \tau)[1 - \cos(\delta\varphi + (k_+ - k_-)L)], \quad (4.9)$$

where we used the following parametrization of the complex matrix elements

$$\begin{aligned} t_{e+} &= \sqrt{\tau} e^{i\varphi_1}, \\ t_{e-} &= \sqrt{1 - \tau} e^{i\varphi_2}, \\ \delta\varphi &= 2(\varphi_1 - \varphi_2). \end{aligned} \quad (4.10)$$

Here,  $\tau$  is the probability that an electron from state  $|e\rangle$  scatters into state  $|+\rangle$ , while  $\varphi_1$  and  $\varphi_2$  are the phases of the complex amplitudes  $t_{e+}$  and  $t_{e-}$ , respectively.

We observe this behavior in the tight-binding simulations of the NS junction as shown in Fig. 4.5. Besides the simple oscillation of  $R_{he}$  in the ZLL regime ( $N = 1$ ), there is

a slight modulation of the amplitude which could be accounted for by a flux-dependent  $\tau = \tau(\phi)$ . In agreement with Eq. (4.9), the AR probability also oscillates as a function of  $L$  for fixed  $\phi$  as shown in Fig. 4.6.

The simple picture that leads to Eq. (4.9) sheds light on the origin of the magnetooscillations within the ZLL regime. As higher LLs come into play ( $N > 1$ ), whether it is done by decreasing the magnetic field or increasing the Fermi energy, a beating pattern emerges and oscillations become more complex.

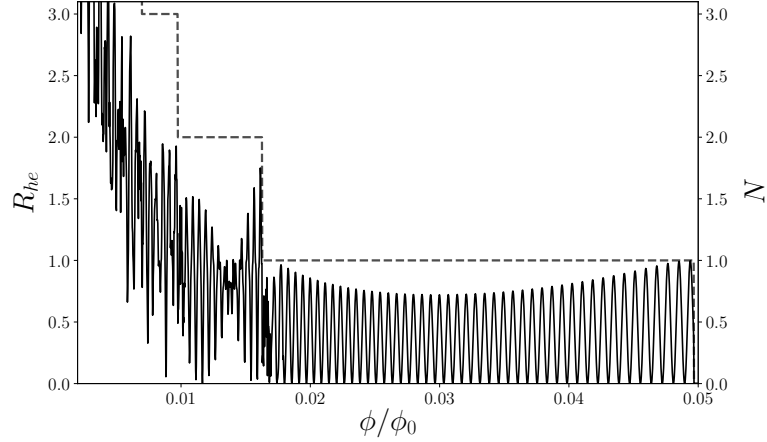


FIGURE 4.5: Andreev reflection probability  $R_{he}$  (left vertical axis) across an NS junction and number of propagating electron modes  $N$  in the normal 2DEG region (right vertical axis) as a function of magnetic flux  $\phi$ . In the region of fluxes where only a single Landau level is occupied ( $N = 1$ ),  $R_{he}$  has a sinusoidal character with a slight amplitude modulation. When  $N = 2$ , a beating pattern appears and for  $N > 2$  even more complicated oscillations can be observed. Magnetic field values and other parameters are exaggerated to make the effect more visible. Here  $\Delta = 0.004t$ ,  $E_F = 0.3t$ ,  $L = 600a$  and  $E = 10^{-6}t$ .

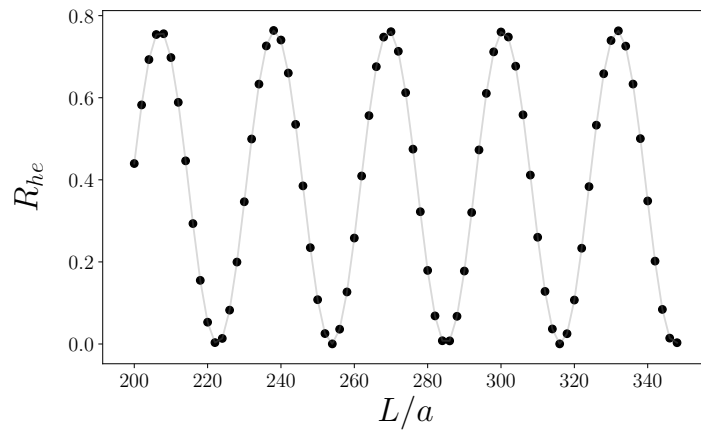


FIGURE 4.6: Andreev reflection probability  $R_{he}$  as a function of interface length  $L$  in an NS junction. The grey line guides the eye between discrete values of  $L$ . For the chosen parameters only the ZLL is occupied ( $N = 1$ ), and we see the oscillations as expected from Eq. (4.9). Here  $\Delta = 0.004t$ ,  $E_F = 0.06t$ ,  $\phi/\phi_0 = 0.005$  and  $E = 10^{-6}t$ .

## GS junction

The situation in GS junctions is different.  $R_{he}$  is constant within the ZLL (as long as the field is not unrealistically high). This is a consequence of the special valley structure of the ZLL edge states [28]. In Fig. 4.7 we plot the AR probability as a function of magnetic flux. The value within the ZLL is a constant given by

$$R_{he} = \frac{1}{2}(1 - \cos \Phi), \quad (4.11)$$

where  $\Phi$  is the angle between valley isospins of the states at the opposite edges represented as three-dimensional vectors on a Bloch sphere. This relation is conspicuously identical to the one in Eq. (3.3) for the conductance across the graphene  $p$ - $n$  junction in quantizing magnetic field. Indeed, there exist a mapping between the GS junction and graphene  $p$ - $n$  junction [67]. This mapping is not to be confused with another one: the correspondence between a junction with uniform carrier density in an antisymmetric magnetic field profile and a junction with antisymmetric carrier density in a uniform field [81].

An oscillatory behavior of  $R_{he}$  in GS junction appears once the higher valley-unpolarized LLs are involved.

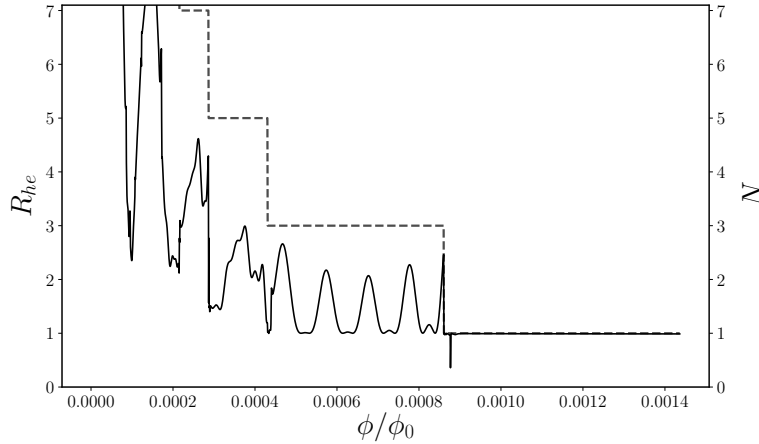


FIGURE 4.7: Andreev reflection probability  $R_{he}$  (left vertical axis) across a GS junction and number of propagating electron modes  $N$  in the normal region made of graphene ribbon with zigzag edges (right vertical axis) as a function of magnetic flux  $\phi$ . The constant  $R_{he} = 1$  within the ZLL ( $N = 1$ ) corresponds to the angle  $\Phi = \pi$  between the valley isospins of the states at the opposite edges of the ribbon. An oscillatory behavior appears once the higher valley unpolarized Landau levels play a role.

## 4.5 Spin transport in the spin-split zeroth Landau level edge states coupled to a superconductor

The results presented in this section are adapted from

T. Sekera, C. Bruder, R. P. Tiwari

*Spin transport in a graphene normal-superconductor junction in the quantum Hall regime*  
arXiv:1807.06975.

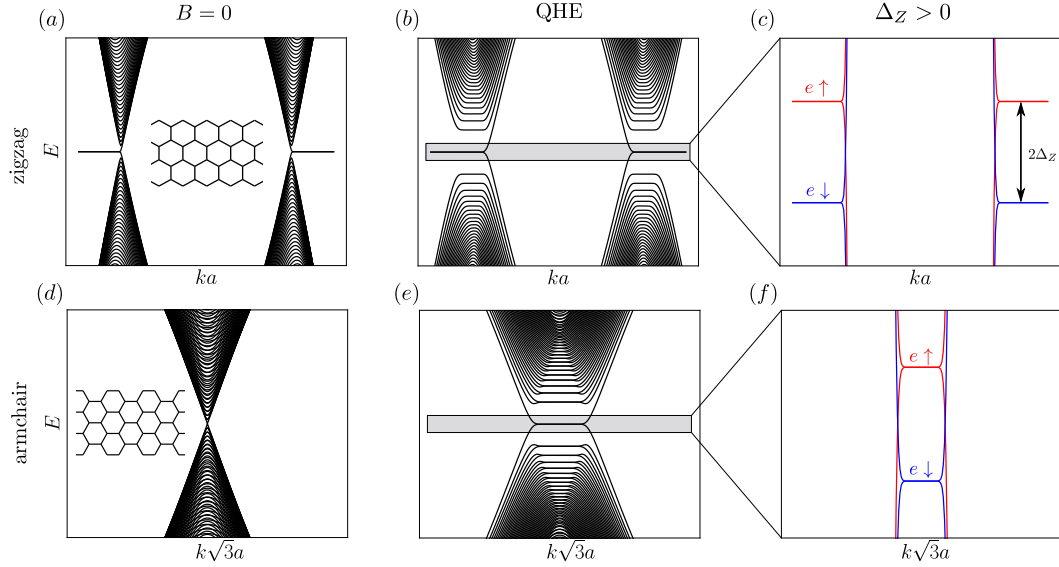


FIGURE 4.8: Zigzag ribbon band structure (a) for  $B = 0$ , (b) in the quantum Hall regime. (c) Zoom-in on the zeroth Landau level that is spin-split by the Zeeman field. (d-f) The same for an armchair ribbon.

The spin-degenerate ZLL in graphene is pinned at the Dirac point. Taking into account the spin splitting of the energy levels due to the Zeeman field, the ZLL is split into two with energy difference  $2\Delta_Z$ , where

$$\Delta_Z = \frac{1}{2}g^*\mu_B|\mathbf{B}|, \quad (4.12)$$

see Fig. 4.8(c). Here,  $2 \leq g^* \lesssim 4$  is the effective g-factor of an electron in graphene,  $\mu_B$  is the Bohr magneton and  $|\mathbf{B}|$  is the absolute value of the applied magnetic field. The energy difference between the spin-up and spin-down ZLL can reach up to  $2\Delta_Z = 2.3$  meV at  $B \sim 10$  T for the interaction-enhanced g-factor  $g^* = 4$  [82]. Note that in addition to the out-of-plane quantizing magnetic field, an in-plane magnetic field can be used to further control  $\Delta_Z$ .

Here we study the interplay of superconductivity and the quantum Hall effect in the ZLL of graphene that is spin-split by a Zeeman field. Without the superconductor, the electron (hole) edge states in the energy window  $\mp E_F - \Delta_Z < E < \mp E_F + \Delta_Z$  are helical: opposite-spin states propagate in opposite directions at a single edge (Fig. 4.9). In a system without a superconductor, the hole degree of freedom plays no role. Here lead  $L_2$  in the three-terminal device shown in Fig. 4.10 is in the normal state and one expects spin-polarized transport in the energy window  $-E_F - \Delta_Z < E < -E_F + \Delta_Z$ ,



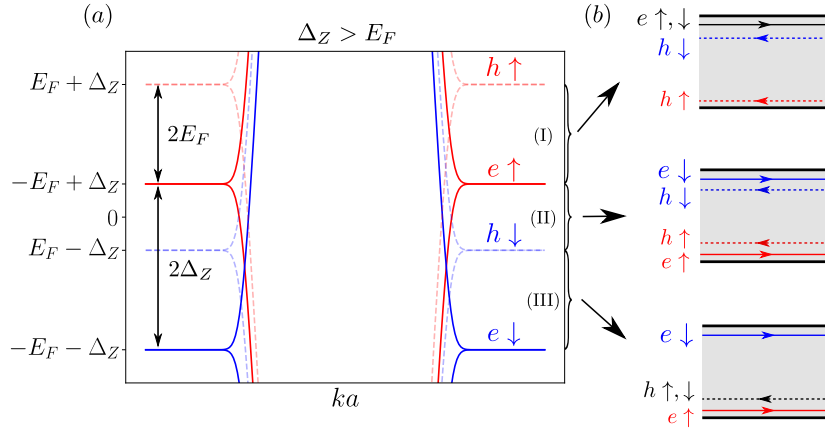


FIGURE 4.9: (a) Band structure of electrons (full lines) and holes (dashed lines) of the spin-split zeroth Landau level for spin up (red) and spin down (blue) in a graphene zigzag ribbon. (b) Electron and hole edge states in a graphene ribbon (gray area) and their propagation direction indicated by arrows shown for the three energy regions I–III.

where the electron edge states are helical in this regime. Curiously, in the case when  $L_2$  is in the superconducting state, this window is shifted to  $E_F - \Delta_Z < E < E_F + \Delta_Z$ . The charge transport is also altered in the presence of the superconducting interface as described below. Note, that the spin-filtering effect presented in this section requires no spin-orbit coupling.

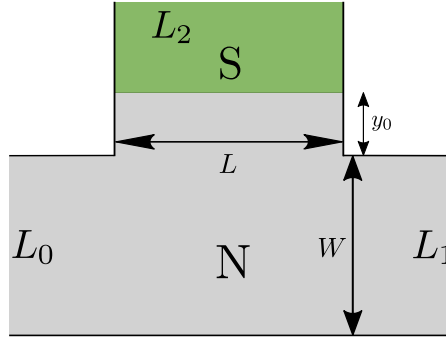


FIGURE 4.10: Three-terminal graphene device with two normal leads  $L_0$  and  $L_1$  and one superconducting lead  $L_2$ . The normal region (N) marked by the grey-shaded region hosts quantum Hall edge states. The superconductor (green area) couples electron and hole edge states propagating along the upper edge.

## Model of the graphene-superconductor interface in Zeeman field

We investigate the spin transport in the three-terminal system shown in Fig. 4.10. The underlying honeycomb lattice is exposed to a quantizing out-of-plane magnetic field. The upper edge of the system is coupled to an s-wave superconductor (S) with a sizeable critical field, such that the quantum Hall effect and superconductivity coexist. There are two normal leads  $L_0$  and  $L_1$  of width  $W$  which serve to probe the spin-resolved

transmission, and a superconducting lead  $L_2$ . The shape of the system is motivated by a recent experiment [77].

The tight-binding Hamiltonian of the system in real space is written in the standard Nambu basis as

$$H = H_0 + H_\Delta + H_Z, \quad (4.13)$$

where  $H_0$  and  $H_\Delta$  are defined in Eq. (4.5), and

$$H_Z = \sum_i \psi_i^\dagger (\rho_0 \otimes \Delta_Z s_z) \psi_i. \quad (4.14)$$

The Zeeman field described by  $H_Z$  splits each LL into two with energy difference  $2\Delta_Z$ .

For the configuration in Fig. 4.10, we choose the vector potential in Landau gauge that is invariant along the  $x$  axis. Namely,

$$\mathbf{A} = (-By, 0, 0). \quad (4.15)$$

Thus the Peierls phase is given by

$$\varphi_{ij} = -\frac{\pi B}{\phi_0} (x_i - x_j)(y_i + y_j), \quad (4.16)$$

where  $\phi_0 = h/e$  is the magnetic flux quantum and  $\mathbf{r}_i = (x_i, y_i)$  are the real-space coordinates of site  $i$ . The third term in  $H_0$  represents the Fermi energy of the system. In the absence of any doping,  $E_F$  is set to zero.

In this system, the following length scales play an important role: magnetic length  $\ell_B = \sqrt{\hbar/eB}$ , superconducting coherence length  $\xi = \hbar v_F/\Delta$  and the system dimensions  $W, L, y_0$  shown in Fig. 4.10. For well-developed LLs we require  $a \ll \ell_B \ll W, L, y_0$ .

## Results: spin and charge transport

In Fig. 4.11(a-c) we plot transport coefficients in the case when  $E_F < \Delta_Z < \Delta$  and the gap between the ZLL and other LLs is large enough so that only the ZLL plays a role in the transport. Since the Hamiltonian in Eq. (4.13) conserves the  $z$ -projection of the spin,  $[H, s_z] = 0$ , only the spin-diagonal transport coefficients are shown: red is for a particle with spin-up scattered to a particle with spin-up, while blue describes the same for spin-down particles.  $T_{ee}$  ( $T_{he}$ ) is the probability for an electron from  $L_0$  to be scattered into an electron (a hole) in  $L_1$  and  $R_{he}$  is the probability for an electron from  $L_0$  to be backscattered as a hole to  $L_0$ . Because we are in the quantum Hall regime and our system is wide enough, the probability for an electron from  $L_0$  to be backscattered as an electron is zero ( $R_{ee} = 0$ ) and hence not shown. Furthermore,  $T_{ee}$  is the normal (N) forward scattering,  $T_{he}$  is the crossed Andreev reflection (CAR) and  $R_{he}$  is the local Andreev reflection (LAR). For energies  $|E| < \Delta$ , the scattering matrix is unitary and  $T_{ee} + T_{he} + R_{he} = 1$  for each spin projection.

It is interesting to look at the spin polarization of the carriers in the subgap regime, where  $|E| < \Delta$ . Having in mind that  $H$  conserves the spin projection along the  $z$ -axis,

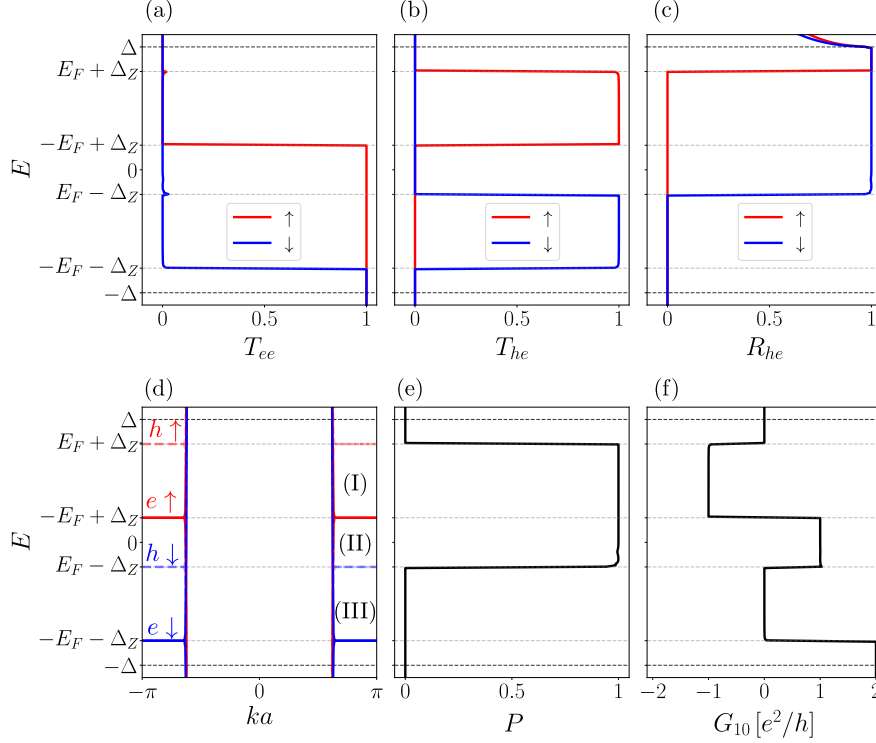


FIGURE 4.11: On the horizontal axis, we plot in (a)–(c) the transport coefficients  $T_{ee}$ ,  $T_{he}$ , and  $R_{he}$  for spin-up (red) and spin-down (blue) particles as a function of energy  $E$  (vertical axis). Similarly, (d) shows the band structure of the spin-split zeroth Landau level for electrons (full lines) and holes (dashed lines) of the normal lead  $L_0$ , (e) the spin polarization, and (f) the charge conductance, all as a function of  $E$ . The thin horizontal dashed lines mark the energies where the edge states change the direction of propagation, while the thick ones correspond to  $|E| = \Delta$ . Here, the edge terminations of  $L_0$  and  $L_1$  are zigzag while the edge termination of  $L_2$  is armchair. The parameters are  $\Delta = 10$  meV,  $E_F = 0.3\Delta$ ,  $\Delta_Z = 0.5\Delta$ ,  $B = 10$  T,  $W = 600a$ ,  $W_2 = 510a$ , and  $y_0 = 300a$ .

we define this quantity as

$$P = \frac{T_{e\uparrow,e\uparrow} + T_{h\uparrow,e\uparrow} - T_{e\downarrow,e\downarrow} - T_{h\downarrow,e\downarrow}}{T_{e\uparrow,e\uparrow} + T_{h\uparrow,e\uparrow} + T_{e\downarrow,e\downarrow} + T_{h\downarrow,e\downarrow}}, \quad (4.17)$$

where  $T_{\alpha's',\alpha s}$  is the transmission coefficient for a particle  $\alpha$  with spin  $s$  in lead  $L_0$  to a particle  $\alpha'$  with spin  $s'$  in lead  $L_1$ .<sup>1</sup>

The spin polarization calculated numerically and shown in Fig. 4.11(e) is non-zero in the energy region  $(E_F - \Delta_Z, E_F + \Delta_Z)$  and zero otherwise. This can be understood by looking at the direction of propagation of the particles, Fig. 4.9(b). In the energy region (II),  $e \uparrow$  travels undisturbed along the lower edge into  $L_1$ , while  $e \downarrow$  propagating along the upper edge is backscattered as  $h \downarrow$  to  $L_0$ . This results in accumulation of spin-up in  $L_1$ . The situation in the energy region (I) is the same for  $e \downarrow$ . However, here  $e \uparrow$  also travels along the upper edge and encounters the superconductor. Since the Andreev reflected  $h \uparrow$  has the same direction of propagation as  $e \uparrow$ , the particle propagates along the GS interface via Andreev edge states, and, depending on the geometry, ends

<sup>1</sup>In our calculations we choose a cut-off:  $P = 0$  if the denominator in Eq. (4.17) is smaller than  $10^{-3}$ , i.e., when almost no particle is transmitted from  $L_0$  to  $L_1$ .

up with a certain probability as  $e \uparrow$  or  $h \uparrow$  in  $L_1$ . This means that injecting spin-unpolarized particles in  $L_0$  results in spin-polarized particles in  $L_1$  in energy region  $E_F - \Delta_Z < E < E_F + \Delta_Z$ .

In the presence of hole excitations, the (differential) charge conductance from  $L_0$  to  $L_1$  is defined as

$$G_{10} = \frac{e^2}{h} \left( \sum_{s=\uparrow,\downarrow} T_{es,es} - T_{hs,es} \right). \quad (4.18)$$

In energy region (I) the carrier ending in  $L_1$  is a hole, while in region (II) it is an electron. In energy region (III) there is an electron  $e \uparrow$  along the lower edge and hole  $h \uparrow$  along the upper edge ending in  $L_1$ , which results in zero charge transfer. The charge conductance behavior, however, is not universal and depends on the geometrical details (valley structure of the edge states).

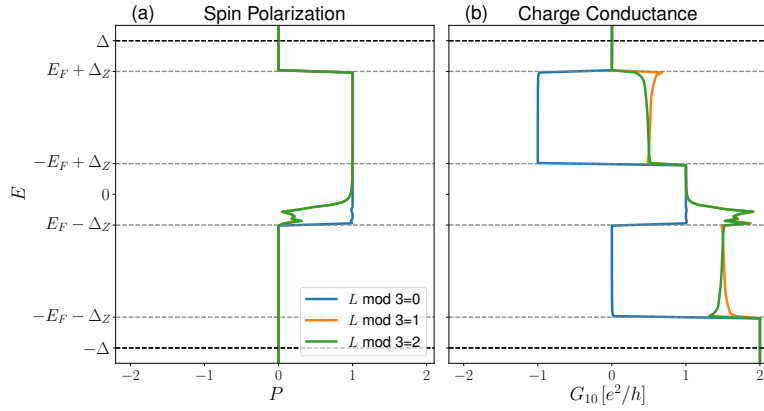


FIGURE 4.12: (a) The spin polarization and (b) the charge conductance for three different interface lengths that corresponds to three different valley polarizations. The charge conductance depends on the angle between the valley isospins, while the spin polarization does not (up to the region where  $e \downarrow$  leaks to  $L_1$  due to the smaller induced gap.) Here edge terminations of  $L_0$  and  $L_1$  are zigzag while of  $L_2$  are armchair. The parameters are  $\Delta = 20$  meV,  $E_F = 0.3\Delta$ ,  $\Delta_Z = 0.5\Delta$ ,  $B = 10$  T,  $W = 147.6$  nm,  $L = 125.46$  nm and  $y_0 = 73.8$  nm.

In Fig. 4.12 we show the spin polarization and conductance for three different widths of  $L_2$  with armchair edge termination. We see the spin polarization that is (almost) independent of  $L$  and the characteristic threefold transport due to the presence of an armchair ribbon. Besides that, we see a set of dips (peaks) in the spin polarization (conductance) for energies close to  $E_F - \Delta_Z$ , that might come as a surprise at first sight. The reason for this feature is an  $e \downarrow$  leaking from  $L_0$  to  $L_1$  through the interface. Without the superconductor, there are edge states propagating in the opposite directions for opposite spins. When we couple the superconductor to the upper edge, the electron incoming on the interface will be reflected as a hole (in the case of non-zero AR probability). However, this hole goes in the direction opposite to the electron edge state for both spin projections in this energy region. Hence, the transport along the interface should be blocked. But if the AR probability is less than one, the electron has a finite chance to leak along the interface onto the other side. In other words, edge states along the upper edge contacted to a superconductor develop an effective gap  $\Delta^*$  [83] that is smaller than the naively expected gap  $2(\Delta_Z - E_F)$  (if  $(\Delta_Z - E_F) < \Delta$ ). The bigger

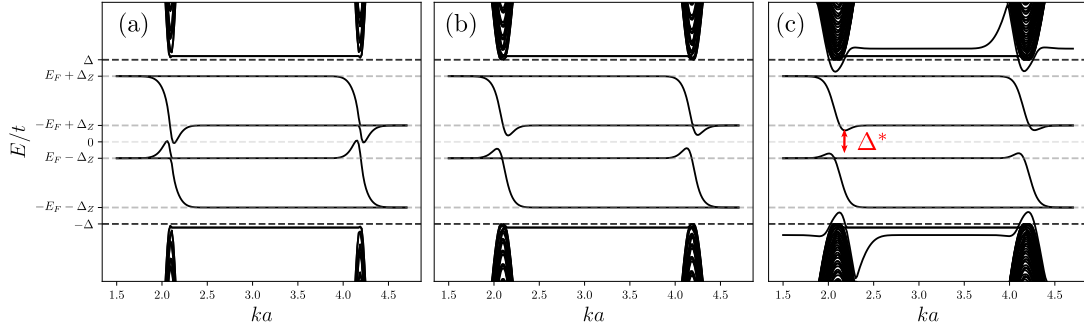


FIGURE 4.13: (a-c) Band structure of excitations along the graphene-superconductor interface in a quantizing magnetic field for  $\Delta/t = 0.03, 0.06, 0.1$ , respectively. Dispersing states at the interface for  $|E| < \Delta$  evolve into the flat zeroth Landau level (ZLL) away from the interface. The bulk ZLL is split into four due to its electron-hole character and the lifted spin degeneracy. When  $E_F < \Delta_Z$ , the ZLL edge states develop an effective band gap  $\Delta^*$  (red arrows) due to the coupling to a superconductor.  $\Delta^*$  increases from (a) to (c) with increasing superconducting pair potential  $\Delta$ . Here  $E_F = 0.3\Delta$ ,  $\Delta_Z = 0.5\Delta$  and the interface is along the zigzag direction. The parameters are exaggerated for better visibility.

the pairing  $\Delta$ , the higher the AR probability. So when increasing  $\Delta$ ,  $\Delta^*$  approaches  $2(\Delta_Z - E_F)$ , see Fig. 4.13.

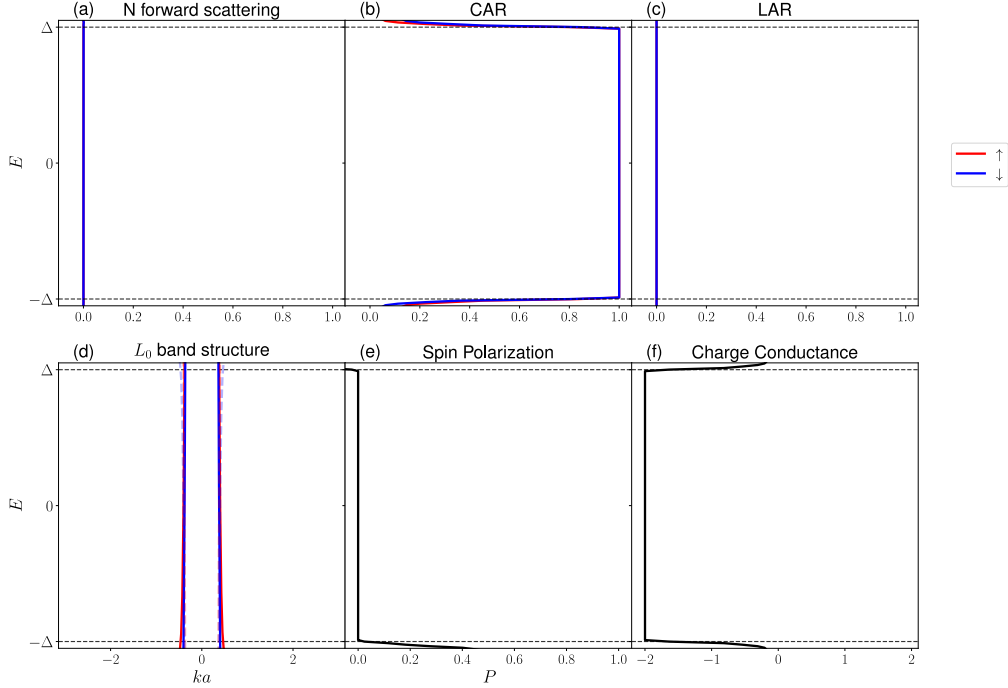


FIGURE 4.14: Same as Fig. 4.11, but  $E_F = 1.6\Delta$ .

The spin-filtering effect is lost once  $E_F > \Delta + \Delta_Z$ . We show this in Fig. 4.14 where the spin polarization vanishes completely for  $|E| < \Delta$ .

### Another edge termination of leads

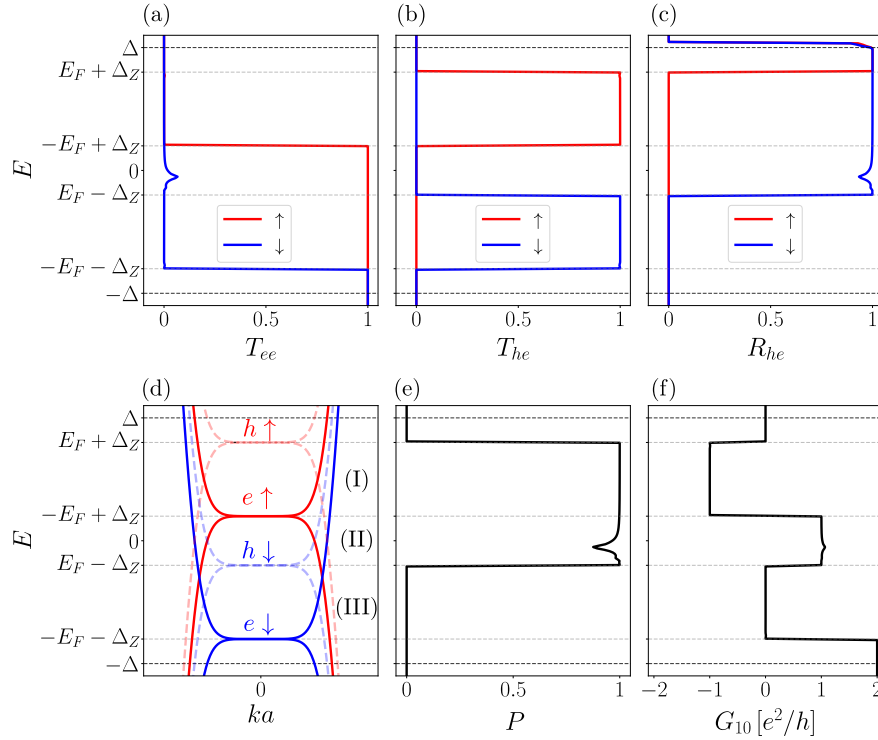


FIGURE 4.15: Same as Fig. 4.11 but with armchair edge terminations for  $L_0$  and  $L_1$  and zigzag edge termination for  $L_2$ .

We obtain the same results for the armchair orientation of leads  $L_0$  and  $L_1$  and the zigzag orientation of lead  $L_2$ , see Fig. 4.15. The spin polarization is again (nearly) perfect for  $E_F - \Delta_Z < E < E_F + \Delta_Z$ . This is expected since, unlike the valley structure, the spin structure of the ZLL in graphene is independent of the type of the edge termination. The dip in the spin polarization is there for the same reason as in Fig. 4.12.

We obtain similar results if leads  $L_0$  and  $L_1$  have armchair orientation and lead  $L_2$  has zigzag orientation, see Fig. 4.15. The spin polarization in Fig. 4.15(e) is again (nearly) perfect for  $E_F - \Delta_Z < E < E_F + \Delta_Z$ . This is expected since, unlike the valley structure, the spin structure of the ZLL in graphene is independent of the type of the edge termination. The conductance profile in Fig. 4.15(f) matches the one in Fig. 4.12(b) for  $L/a = 0 \bmod 3$ , which is the result of the same valley structure for the states at the edges of the NS interface for the two cases. The dip in the spin polarization is present for the same reason as in Fig. 4.12.

## 4.6 Conclusion

The interface between graphene and a superconductor has several unusual and distinct properties owing to the linear low-energy dispersion and its valley structure. Without a magnetic field, specular Andreev reflection takes place in energy region  $E > E_F$  for  $\Delta > E_F$ , where  $E$  is the energy of the incoming electron. Switching on a quantizing magnetic field, the conductance of a GS junction as a function of flux is constant within

the zeroth Landau level. That is in sharp contrast to the oscillatory behavior in the NS junction. When taking into account the Zeeman splitting of the zeroth Landau level, we show that a spin-filtering effect is present in a three-terminal setup with a GS junction, and can be switched on and off simply by gate voltage that shifts the Fermi energy. Such an effect requires no spin-orbit coupling.





## CHAPTER 5

# THE TOPOLOGICAL ANDERSON INSULATOR PHASE IN THE KANE-MELE MODEL

*The results presented in this chapter were published in*

C. P. Orth, T. Sekera, C. Bruder, T. L. Schmidt  
*The topological Anderson insulator phase in the Kane-Mele model*  
Sci. Rep. **6**, 24007 (2016).

*Changes have been made to better embed this work into the thesis. The introduction was expanded and Subsection 5.6.1 concerning magnetic disorder was added.*

It has been proposed that adding disorder to a topologically trivial mercury telluride/-cadmium telluride (HgTe/CdTe) quantum well can induce a transition to a topologically nontrivial state. The resulting state was termed topological Anderson insulator and was found in computer simulations of the Bernevig-Hughes-Zhang model. Here, we show that the topological Anderson insulator is a more universal phenomenon and also appears in the Kane-Mele model of topological insulators on a honeycomb lattice. We numerically investigate the interplay of the relevant parameters, and establish the parameter range in which the topological Anderson insulator exists. A staggered sublattice potential turns out to be a necessary condition for the transition to the topological Anderson insulator. For weak enough disorder, a calculation based on the lowest-order Born approximation reproduces quantitatively the numerical data. Our results thus considerably increase the number of candidate materials for the topological Anderson insulator phase.

### 5.1 Introduction

If the Fermi energy is placed in the band gap of a conventional insulator, no electronic states can propagate at this energy and the material does not conduct electricity. Even though the band gap of a conventional insulator, such as solid argon, is much larger in comparison to that of an ordinary semiconductor, the electronic states of the two are, in

a sense, equivalent. It is possible to deform their Hamiltonians into each other without closing the energy gap. There are, however, insulators with Hamiltonians that cannot be deformed into that of a conventional insulator. This motivated a topological classification scheme of gapped electronic systems [84]. The mathematical theory of vector bundles provides tools for such classification, see Refs. [85] and [86] for an introduction. The idea is that to each Hamiltonian one can assign a number, so-called *topological invariant*, that cannot be changed by adiabatically deforming the Hamiltonian unless the gap is closed or a symmetry is broken. So, which systems with Hamiltonians that are not topologically equivalent to conventional (trivial) insulators are there? The simplest one is the quantum Hall system studied in previous chapters. Here, the topological invariant is called the Chern number and can take integer values (thus also the name  $\mathbb{Z}$  invariant). The characteristic feature of the quantum Hall system is the existence of chiral states confined to the boundary with vacuum (edge states) that lead to the quantized Hall conductance. These states are robust against small perturbations and lead to the perfectly quantized Hall conductance. The number of edge states corresponds to the Chern number, as well as to the quantized filling factor. The existence of the states localized at the boundary with vacuum is a general feature of topologically nontrivial phases and the result of the bulk-boundary correspondence.

The key object of the present chapter is the so-called *topological insulator* (TI) in two dimensions (2D). This is a gapped electronic phase in the presence of time-reversal symmetry (TRS), where the bulk gap is opened by the spin-orbit coupling. Unlike the quantum Hall system, a TI is characterized by a  $\mathbb{Z}_2$  invariant that can take only two distinct values that correspond to the trivial phase and the TI phase. In the presence of a boundary with vacuum, the TI phase manifests itself by two gapless counter-propagating edge states of opposite spin projection. These states are robust with respect to TRS-preserving perturbations and lead to a quantized two-terminal conductance. In this chapter, the 2D TI is described by the Kane-Mele (KM) Hamiltonian (5.1), while also other models exist; e.g., the Bernevig-Hughes-Zhang (BHZ) model [87]. As will be shown in Sec. 5.2, the ratio among the parameters in the KM Hamiltonian decides which phase, trivial or topological, is realized in the ground state. For the review on TIs see Refs. [11, 88].

Due to the invariant nature of the topological phases, the edge states are robust against small symmetry-preserving perturbations. From Anderson's theory of localization [89] one expects that a system with finite conductance without disorder undergoes a transition to a system with localized states and suppressed conductance as the disorder is increased beyond a certain threshold value. Indeed, we observe a completely vanishing conductance for large disorder strength  $W$ , where the disorder is modeled by a random on-site potential. However, a curious effect may take place at intermediate  $W$ . A plateau of quantized conductance is seen to persist for a significant range of energies and  $W$ . Even more surprisingly, if a system described by the KM Hamiltonian without disorder is a trivial insulator, adding disorder can cause a closing of the trivial gap and reopening of the topological one. A system that exhibits such disorder induced transition from a trivial insulator to a TI is termed topological Anderson insulator (TAI). The explanation of this transition lies in the renormalization of the Hamiltonian parameters. The BHZ model with disorder and band mass  $m$  can be approximated by an effective

model of a clean system and renormalized mass  $\bar{m}$ . Using an effective-medium theory and the self-consistent Born approximation (SCBA), it was shown that for certain model parameters,  $\bar{m}$  can become negative even if the bare mass  $m$  is positive [90]. As a consequence, the effective model becomes that of a TI and features edge states with a quantized conductance of  $G_0 = e^2/h$  [91].

Furthermore, TAIs have been predicted in several related systems, for instance in a honeycomb lattice described by the TRS breaking Haldane model [92], a modified Dirac model [92], the BHZ model with  $s_z$  non-conserving spin-orbit coupling [93], as well as in 3D topological insulators [94]. Moreover, similar transitions from a topologically trivial to a topologically nontrivial phase have been found to be generated by periodically varying potentials [95] or phonons [96]. In contrast to on-site Anderson disorder, certain kinds of bond disorder cannot produce a TAI as they lead only to a positive correction to  $m$  [97, 98]. Here, we report on the TAI found in the KM model, describing materials with honeycomb lattice, such as graphene, silicene, germanene and stanene [99–102]. Previous studies found first indications to this TAI phase, showing that the KM model without a staggered sublattice potential hosts extended bulk states even for large disorder strengths [103].

The interplay between the parameters characterizing intrinsic spin-orbit coupling (SOC)  $\lambda_{\text{SO}}$ , extrinsic Rashba SOC  $\lambda_R$ , and a staggered sublattice potential  $\lambda_\nu$  turns out to be crucial for the visibility of TAIs, and we calculate the parameter ranges in which TAIs can be observed. We find analytically that to lowest order in  $W$ , the parameters  $\lambda_{\text{SO}}$  and  $\lambda_R$  are not renormalized with increasing disorder strength, in contrast to  $\lambda_\nu$ . However, a new effective hopping  $\lambda_{R3}$  is generated due to the disorder, which is related but not identical to  $\lambda_R$ . Although  $\lambda_R$  is not a crucial ingredient for the existence of TAIs, it significantly alters the physics of topological insulators in various ways [104, 105] and, as we will show below, strongly affects the TAI state.

Observation of the TAI is experimentally challenging. The main difficulty is the requirement of a rather large and specific amount of disorder, which is tough to control in the topological insulators currently investigated, where the 2D TI layer is buried inside a semiconductor structure. In contrast, producing and controlling disorder in 2D materials described by the KM model could be much easier. Disorder in 2D materials with honeycomb structure can be produced by randomly placed adatoms [106, 107] or a judicious choice of substrate material [108–111]. Moreover, a sizeable staggered sublattice potential can be generated via a suitable substrate material [112]. Other means of engineering disorder were proposed in periodically driven systems [113, 114]. Finally, honeycomb structures with the SOC necessary to produce a topological phase have already been realized using ultracold atoms in optical lattices [115], in which disorder can in principle be engineered. A recent experiment finds evidence for the TAI in one-dimensional disordered atomic wires [116].

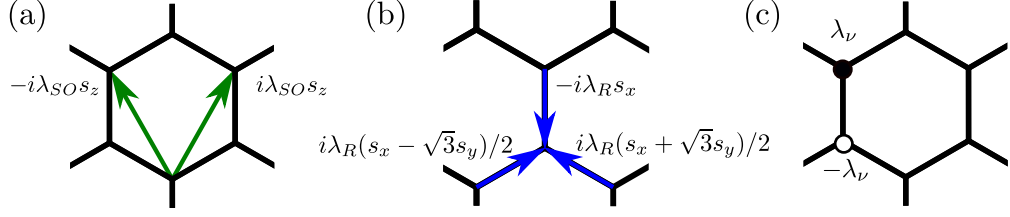


FIGURE 5.1: Visualization of the terms in the Kane-Mele Hamiltonian (5.1) and their amplitudes. (a) Intrinsic spin-orbit coupling represented by the second nearest-neighbor hopping (green arrows) and (b) Rashba spin-orbit coupling represented by the first nearest-neighbor hopping on a honeycomb lattice (blue arrows). (c) Staggered sublattice on-site potential.

## 5.2 Kane-Mele Hamiltonian

Let us start by introducing the KM Hamiltonian [117, 118]

$$H = t \sum_{\langle ij \rangle} c_i^\dagger c_j + i\lambda_{\text{SO}} \sum_{\langle\langle ij \rangle\rangle} \nu_{ij} c_i^\dagger s_z c_j + i\lambda_R \sum_{\langle ij \rangle} c_i^\dagger (\mathbf{s} \times \hat{\mathbf{d}}_{ij})_z c_j + \lambda_\nu \sum_i \xi_i c_i^\dagger c_i. \quad (5.1)$$

Summations  $\sum_{\langle ij \rangle}$  and  $\sum_{\langle\langle ij \rangle\rangle}$  denote the sum over the nearest and next-nearest neighbors (nn and nnn), respectively. Operators  $c_i^\dagger = (c_{i\uparrow}^\dagger, c_{i\downarrow}^\dagger)$  and  $c_i = (c_{i\uparrow}, c_{i\downarrow})^T$  are the creation and annihilation operators for the particle at site  $i$ . The parameters  $t$ ,  $\lambda_{\text{SO}}$  and  $\lambda_R$  represent the amplitude of the nn hopping, intrinsic SOC, and Rashba SOC, respectively. If the nnn hopping from site  $j$  to site  $i$  corresponds to a right-turn on the honeycomb lattice, then  $\nu_{ij} = 1$ , otherwise  $\nu_{ij} = -1$ . In other words,  $\nu_{ij} = (2/\sqrt{3})(\hat{\mathbf{d}}_1 \times \hat{\mathbf{d}}_2)_z$ , where  $\hat{\mathbf{d}}_1$  and  $\hat{\mathbf{d}}_2$  are unit vectors along the two bonds the electron traverses going from site  $j$  to site  $i$ . Furthermore,  $\mathbf{s} = (s_x, s_y, s_z)$  is the vector of Pauli matrices for the spin degree of freedom, and  $\hat{\mathbf{d}}_{ij}$  is the unit vector between sites  $j$  and  $i$ . The Wannier states at the two basis atoms of the honeycomb lattice are separated in energy by twice the amplitude of the staggered sublattice potential term  $\lambda_\nu$ , where  $\xi_i = 1$  for the  $A$  sublattice and  $\xi_i = -1$  for the  $B$  sublattice. Terms in Eq. (5.1) and their amplitudes are visualized in Fig. 5.1.

Hamiltonian (5.1) can be diagonalized in translationally symmetric situation. Due to sublattice and spin, each block (labeled by  $\mathbf{k}$ ) in the block-diagonal matrix is the following 4x4 matrix

$$\mathcal{H}(\mathbf{k}) = \sum_{a=0}^5 d_a(\mathbf{k}) \Gamma^a + \sum_{a<b=1}^5 d_{ab}(\mathbf{k}) \Gamma^{ab}, \quad (5.2)$$

where  $\Gamma^{(0,1,2,3,4,5)} = (\sigma^0 \otimes s^0, \sigma^x \otimes s^0, \sigma^z \otimes s^0, \sigma^y \otimes s^x, \sigma^y \otimes s^y, \sigma^y \otimes s^z)$  and  $\Gamma^{ab} = [\Gamma^a, \Gamma^b]/(2i)$ . Here,  $\sigma^\mu$  for  $\mu \in \{0, 1, 2, 3\}$  are the Pauli matrices representing the sublattice index. The coefficient are

$$\begin{aligned} d_1(\mathbf{k}) &= t(1 + 2 \cos x \cos y), & d_{12}(\mathbf{k}) &= -2t \cos x \sin y, \\ d_1(\mathbf{k}) &= \lambda_\nu, & d_{12}(\mathbf{k}) &= \lambda_{\text{SO}}(2 \sin 2x - 4 \sin x \cos y), \\ d_1(\mathbf{k}) &= \lambda_R(1 - \cos x \cos y), & d_{12}(\mathbf{k}) &= -\lambda_R \cos x \sin y, \\ d_1(\mathbf{k}) &= -\sqrt{3} \lambda_R \sin x \sin y, & d_{12}(\mathbf{k}) &= \sqrt{3} \lambda_R \sin x \cos y, \end{aligned}$$

with  $x = k_x a/2$  and  $y = \sqrt{3}k_y a/2$ . Diagonalized Hamiltonian (5.2) leads to four energy bands that are functions of 2D momentum  $\mathbf{k}$ . The Dirac point structure due to the nn hopping term is still present, however, a gap can be opened at these points. The topological nature and size of the gap depends on the parameter set  $\lambda_{\text{SO}}$ ,  $\lambda_R$ , and  $\lambda_\nu$ . For  $\lambda_R = 0$ , the system has an energy gap of magnitude  $|6\sqrt{3}\lambda_{\text{SO}} - 2\lambda_\nu|$ , that is topologically non-trivial if  $\lambda_\nu/\lambda_{\text{SO}} < 3\sqrt{3}$  and trivial otherwise [117]. The quasi-1D ribbon along the zigzag direction and examples of the band structure are displayed in Fig. 5.2. For  $\lambda_\nu = 0$ , the system will be a topological insulator if  $\lambda_R/\lambda_{\text{SO}} \lesssim 2\sqrt{3}$  and a metal or semimetal otherwise. For finite  $\lambda_\nu$  and  $\lambda_R$  the situation is more complex and a topological transition appears for values within these two boundaries, see the phase diagram in Fig. 5.2(c).

Low energy expansion of Hamiltonian (5.2) in the vicinity of Dirac point  $\mathbf{K} = (2\pi/a)(2/3, 0)$  leads to

$$\mathcal{H}(\mathbf{q}) = -t \frac{\sqrt{3}a}{2} (q_x \sigma_x + q_y \sigma_y) \otimes s_0 - \lambda_{\text{SO}} 3\sqrt{3} (\sigma_z \otimes s_z) + \lambda_R \frac{3}{2} (\sigma_y \otimes s_x - \sigma_x \otimes s_y) + \lambda_\nu (\sigma_z \otimes s_0), \quad (5.3)$$

where  $\mathbf{k} = \mathbf{K} + \mathbf{q}$ . The presence or absence of the terms depends on the symmetries of the system. The spin-orbit term  $\propto \sigma_z \otimes s_z$  respects all of the symmetries dictated by the nn hopping term and is present, hence the name intrinsic. If the mirror symmetry about  $z = 0$  plane is broken, e.g., by an out-of-plane electric field or substrate, that allows for the (extrinsic) Rashba term  $\propto (\sigma_y \otimes s_x - \sigma_x \otimes s_y)$ . Finally, if the inversion symmetry in the plane of the honeycomb lattice is broken, i.e., A atoms and B atoms cannot be interchanged, then also the staggered sublattice potential  $\propto (\sigma_z \otimes s_0)$  is present. Note that all the terms respect the TRS symmetry.

The KM Hamiltonian was first introduced to describe electrons in graphene [117]. However, it turned out that the non-trivial gap caused by the intrinsic SOC is tiny [119–121]. Thus, graphene is not considered to be a good candidate for a TI while other materials like germanene, stanene or silicene might play this role better.

In order to study the disorder-induced transition from the trivial insulator to the TI, the following term is added to the Hamiltonian (5.1)

$$H' = W \sum_i \epsilon_i c_i^\dagger c_i. \quad (5.4)$$

This is the on-site disorder term with disorder strength  $W$  and uniformly distributed random variables  $\epsilon_i \in [-1, 1]$ .

### 5.3 Numerical results

For  $\lambda_R = 0$ , we find a TAI phase for parameters close to the topological transition at  $\lambda_\nu/\lambda_{\text{SO}} = 3\sqrt{3} \approx 5.2$ . Changing this ratio corresponds to changing the band mass in the case of the BHZ model. Figure 5.3 shows the conductance for different values of  $\lambda_\nu$ . We find that for  $\lambda_\nu = 1.45t \approx 4.8\lambda_{\text{SO}}$  the system is a topological insulator. For  $W = 0$ , i.e., in the clean case, the conduction and valence bands are separated by a red region

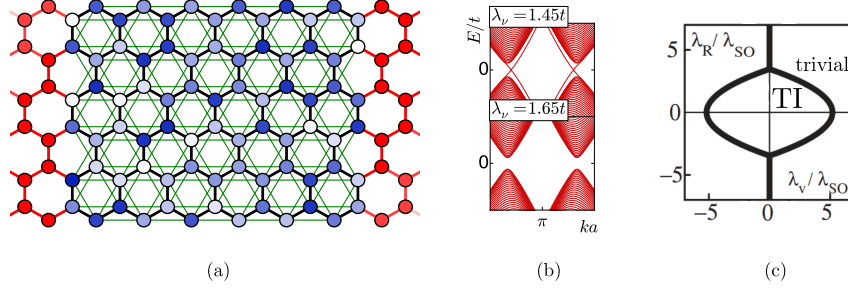


FIGURE 5.2: (a) Zigzag ribbon of honeycomb lattice illustrating the tight-binding terms in the Kane-Mele Hamiltonian (5.1) with disorder. The blue color scale marks different on-site potentials. Thick black lines correspond to nearest-neighbor hopping and Rashba SOC, while thin green lines correspond to intrinsic SOC. The leads attached at both sides (red color) are modeled by a hexagonal lattice with nearest-neighbor hopping term and finite chemical potential. In this example, the sample has width  $w = 5a$  and length  $l = 6a$ . Much larger sample sizes of  $w = 93a$  and length  $l = 150a$  were used in the calculations described below. (b) Band structures of infinitely long samples of width  $w = 93a$  for two different values of  $\lambda_v$  showing a topologically nontrivial and a trivial gap. Vertical and horizontal axis correspond to energy in units of  $t$  and dimensionless momentum, respectively. Parameters are  $\lambda_{SO} = 0.3t$  and  $\lambda_R = 0$ . (c) Phase diagram adapted from [118].

with a quantized conductance of  $2G_0$ . Remarkably, with increasing disorder strength, the states in the conduction and valence bands localize, but the helical edge states that are responsible for the conductance of  $2G_0$  exist for an even larger energy window. The conductances and the vanishing error bars for the two distinct energy values  $E_F = 0$ ,  $E_F = 0.2t$  in the lower row of Fig. 5.3 show that the conductance quantization, and with it the topological nature of the system, persist for the vast majority of microscopic disorder configurations. For  $\lambda_v = 1.65t = 5.5\lambda_{SO}$ , the system is a trivial insulator at  $W = 0$ . The trivial gap closes however, and at  $W \approx t$  the system develops a topologically non-trivial gap and edge states. This can be seen from the quantized conductance. Finally, for  $\lambda_v = 1.85t \approx 6.2\lambda_{SO}$ , the closing of the trivial gap and re-opening of the topological gap happens at a disorder strength which is strong enough to destabilize the emergent topological phase. Features of the conductance quantization can still be seen, but this behavior is not that robust anymore. As no averaging is done in the upper row of Fig. 5.3, and a new disorder configuration is taken for every data point, destabilization of the topological phase can be seen by red and white speckles in the figure.

We find that no TAI exists without staggered sublattice potential ( $\lambda_v = 0$ ). If both  $\lambda_v$  and  $\lambda_R$  are finite, the TAI phase is in general less pronounced, see Fig. 5.4. The plot on the right shows the closing of a trivial gap and emergence of a topological one at  $W \approx 0.5t$ .

Furthermore, we observe that the simultaneous presence of intrinsic and Rashba SOC (both  $\lambda_R \neq 0$  and  $\lambda_{SO} \neq 0$ ) destroys the particle-hole symmetry in the spectrum. In the absence of Rashba SOC, the symmetry operator  $\Upsilon$ , which acts on the lattice operators as  $\Upsilon c_{i\sigma A} \Upsilon^{-1} = c_{-i,\sigma,B}^\dagger$  and  $\Upsilon c_{i\sigma B} \Upsilon^{-1} = -c_{-i,\sigma A}^\dagger$  for the sublattices  $A$  and  $B$ , leaves the (disorder-free) Hamiltonian invariant.  $\Upsilon$  can be viewed as particle-hole conjugation combined with spatial inversion, and the inversion is needed to leave the staggered sublattice potential term invariant.

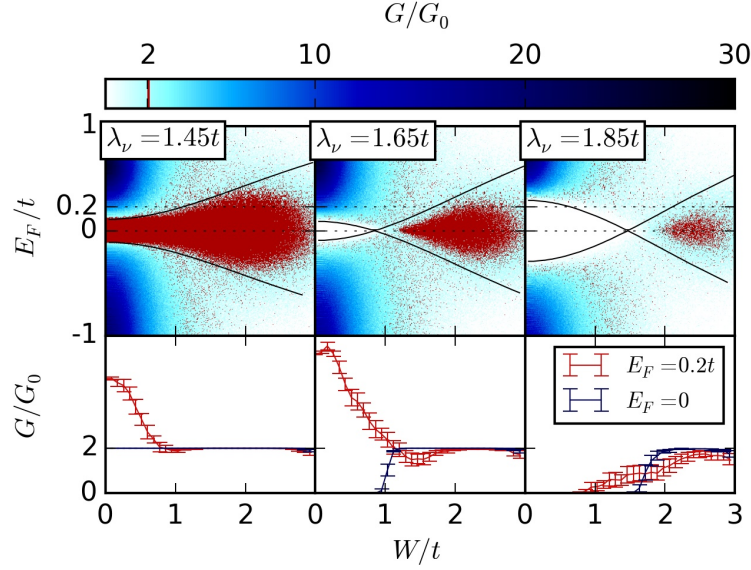


FIGURE 5.3: *Top row:* The conductance from the left to the right lead as a function of the disorder strength  $W$  (horizontal axis) and chemical potential  $E_F$  (vertical axis). The conductance varies from 0 (white) to  $30G_0$  (dark blue). The quantized value of  $2G_0$  (red for all conductances within  $[1.95G_0, 2.05G_0]$ ) originates from two helical edge states. The three plots show the conductance for three different values of  $\lambda_\nu$  that represent, respectively, a topological insulator, a TAI, and a TAI at the transition to an ordinary insulator. The black lines are obtained from a lowest-order Born approximation without any adjustable parameter. The two dotted lines mark the energies  $E_F = 0$ ,  $E_F = 0.2t$ . *Bottom row:* The conductance at fixed chemical potentials  $E_F = 0$  (black) and  $E_F = 0.2t$  (red) for the same parameters as in the top row. The errors bars originate from an averaging procedure over 100 disorder configurations. The vanishing error bars in the regions with a conductance of  $2G_0$  show that the topological phase is stable irrespective of the exact disorder configuration. The system parameters are  $w = 93a$ ,  $l = 150a$ ,  $\lambda_{SO} = 0.3t$ , and  $\lambda_R = 0$ .

## 5.4 Lowest-order Born approximation

In the self-consistent Born approximation, the self-energy  $\Sigma$  for a finite disorder strength is given by the following integral equation [90, 122]

$$\Sigma = \frac{1}{3}W^2 \left( \frac{a}{2\pi} \right)^2 \int_{BZ} d\mathbf{k} \frac{1}{E_F - \mathcal{H}(\mathbf{k}) - \Sigma}, \quad (5.5)$$

where  $\mathcal{H}(\mathbf{k})$  is the Fourier transform of  $H$  in the clean limit, Eq. (5.2). The coefficient  $1/3$  originates from the second moment  $\langle \epsilon_i^2 \rangle = 1/3$  of the uniform distribution function of the disorder amplitudes, and  $E_F$  is the chemical potential. The integration is over the full first Brillouin zone. We use the lowest-order Born approximation, which means setting  $\Sigma = 0$  on the right-hand side of the equation.

After a low-energy expansion of  $\mathcal{H}(\mathbf{k})$ , i.e., Eq. (5.3), the integral can be evaluated analytically [90] for  $\lambda_R = 0$ . This requires keeping the terms up to second order in  $\mathbf{k}$  wherever this is the leading  $\mathbf{k}$ -dependent order. The evaluation yields the renormalized

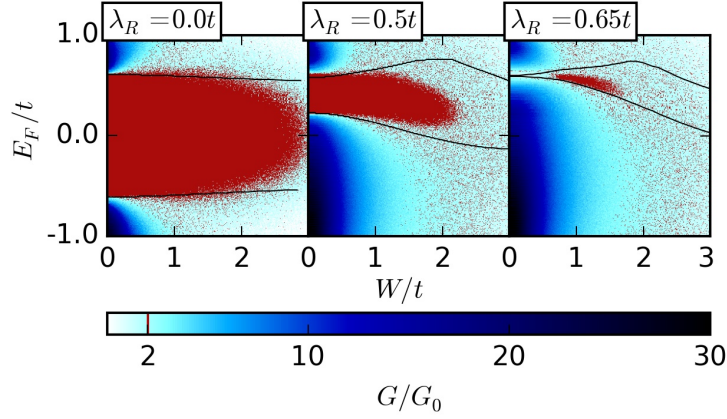


FIGURE 5.4: The conductance for increasing disorder strength  $W$  and chemical potentials  $E_F$  for three different values of  $\lambda_R = 0$  (left),  $\lambda_R = 0.5t$  (middle) and  $\lambda_R = 0.65t$  (right). The system parameters are  $w = 93a$ ,  $l = 150a$ ,  $\lambda_{\text{SO}} = 0.3t$ , and  $\lambda_\nu = 0.95t$ . The black lines are obtained from a lowest-order Born approximation without any fitting parameter. The conductance color code is the same as in Fig. 5.3

staggered sublattice potential

$$\bar{\lambda}_\nu = \lambda_\nu + \frac{W^2}{9\pi\sqrt{3}\lambda_{\text{SO}}} \log \left| \frac{27\lambda_{\text{SO}}^2}{E_F^2 - (\lambda_\nu - 3\sqrt{3}\lambda_{\text{SO}})^2} \left( \frac{\pi}{2} \right)^4 \right|, \quad (5.6)$$

For a certain set of parameters, the logarithm can be negative and  $\bar{\lambda}_\nu$  is reduced compared to  $\lambda_\nu$ . Moreover, we find that  $\lambda_{\text{SO}}$  is not renormalized to order  $W^2$ . Therefore, it is possible to obtain  $\lambda_\nu > 3\sqrt{3}\lambda_{\text{SO}} > \bar{\lambda}_\nu$ . The system thus makes a transition from a trivial insulator to a topological insulator with increasing  $W$ .

For a more quantitative treatment, we evaluate the integral for the full Hamiltonian  $\mathcal{H}(\mathbf{k})$  in Eq. (5.2) numerically. The self-energy  $\Sigma$  is then written as a linear combination of several independent contributions

$$\Sigma = \sum_{a=0}^5 g_a \Gamma^a + \sum_{a<b=1}^5 g_{ab} \Gamma^{ab}, \quad (5.7)$$

where  $g_a$  and  $g_{ab}$  are the coefficients determined by the disorder. This leads to the following equations for the renormalized quantities

$$\begin{aligned} \bar{\lambda}_\nu &= \lambda_\nu + g_2, \\ \bar{E}_F &= E_F - g_0, \\ \bar{\lambda}_{R3} &= g_3, \end{aligned} \quad (5.8)$$

whereas  $\bar{\lambda}_{\text{SO}} = \lambda_{\text{SO}}$  and  $\bar{\lambda}_R = \lambda_R$  remain unrenormalized to lowest order in  $W$ . Surprisingly, a new coupling  $\bar{\lambda}_{R3}\Gamma^3$  is created by the disorder. This coupling has the matrix structure  $\Gamma^3$ , which is similar but not identical to the one for Rashba SOC. Expressing this new term in the lattice coordinates of Eq. (5.1) reveals that it corresponds to a Rashba-type nearest-neighbor hopping term which is asymmetric and appears only for



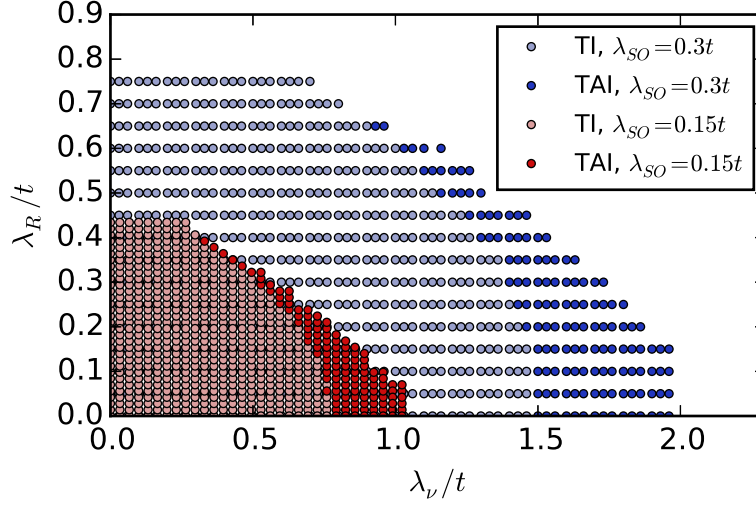


FIGURE 5.5: Phase diagram in the  $(\lambda_\nu, \lambda_R)$  plane. Strong blue (red) color marks the region for which a TAI exists for  $\lambda_{SO} = 0.3t$  ( $0.15t$ ). Transparent blue (red) color indicates the regions where a topological insulator is found for zero disorder. Each dot represents an individual simulation of the kind illustrated in Fig. 5.3.

bonds that are parallel to the unit vector  $(0, 1)$ ,

$$H_{R3} = i\lambda_{R3} \sum_{\langle ij \rangle_v} c_i^\dagger (\mathbf{s} \times \hat{\mathbf{d}}_{ij})_z c_j, \quad (5.9)$$

where  $\langle ij \rangle_v$  stands for summations over strictly vertical bonds only. Furthermore, we find to lowest order in  $W$  that  $\bar{\lambda}_{R3} = 0$  for  $\lambda_R = 0$ .

For  $W = \lambda_R = 0$ , the upper and lower edge of the gap are at the energies  $E_F = \pm|3\sqrt{3}\lambda_{SO} - \lambda_\nu|$ . This is the case for both topological and trivial insulators. Extrapolation of these equations to finite  $W$  leads to the conditions  $\bar{E}_F(E_F) = \pm|3\sqrt{3}\bar{\lambda}_{SO} - \bar{\lambda}_\nu(E_F)|$ . The solid black lines in Fig. 5.3 are the two solutions to these equations and describe the closing and reopening of the gap qualitatively for small  $W$ .

For finite  $\lambda_R$  and therefore finite  $\lambda_{R3}$ , there is no analytical expression of the gap energy. In this case, we read off the positions of the gap edges from band structure calculations for several values of  $\lambda_R$  and  $\lambda_{R3}$ . An interpolation leads to two functions  $h_{U,L}(\lambda_\nu, \lambda_R, \lambda_{R3})$  for the upper and lower band edge in the clean system. Replacing the unperturbed by the renormalized parameters yields two equations

$$h_{U,L}[\bar{\lambda}_\nu(E_F), \bar{\lambda}_R(E_F), \bar{\lambda}_{R3}(E_F)] = \bar{E}_F(E_F). \quad (5.10)$$

The solutions of these equations are indicated by the solid black lines in Fig. 5.4. Hence, these results agree with the numerical data for small  $W$  without any fitting parameter. Deviations appear for larger  $W$ , when the lowest-order Born approximation is not applicable.

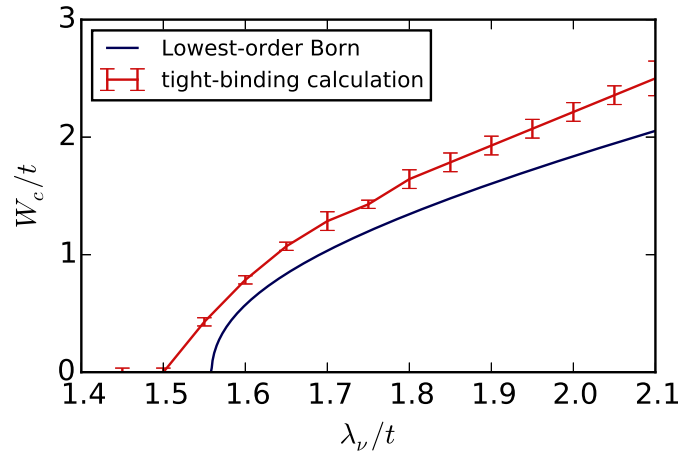


FIGURE 5.6: Critical value of the disorder strength for the TAI transition along the line  $\lambda_R = 0$  for  $\lambda_{SO} = 0.3t$ . Comparison between tight-binding simulation and analytical results.

## 5.5 Phase diagram

Figure 5.5 shows a phase diagram as a function of  $\lambda_\nu$  and  $\lambda_R$  based on the tight-binding simulations. The strong color marks the regions for which a critical disorder strength  $W_c$  exists above which the system is a TAI (blue for  $\lambda_{SO} = 0.3t$ , red for  $\lambda_{SO} = 0.15t$ ). The TAI phase is located along the boundary separating trivial from topological insulators in the clean case. Towards larger  $\lambda_R$ , the TAI region becomes narrower and eventually vanishes above a critical  $\lambda_R$ . Figure 5.6 shows the critical disorder strength  $W_c$  as a function of  $\lambda_\nu$  for a fixed value of  $\lambda_R$ .

In Figs. 5.3 and 5.4 rather large values of the parameters  $\lambda_{SO}$ ,  $\lambda_\nu$  and  $\lambda_R$  were chosen to better visualize the effect. The TAI phenomenon scales down also to smaller values of the parameters, as the red region in the Fig. 5.5 indicates, but the TAI phase becomes less pronounced in the conductance plots and is harder to identify. Material parameters for stanene, for example, are  $t = 1.3$  eV,  $\lambda_{SO} = 0.1$  eV [123] and  $\lambda_R = 10$  meV [124]. We suspect that disorder, e.g., originating from missing or dislocated atoms, can reach disorder strengths in the eV range.

## 5.6 Alternative disorder models

### 5.6.1 Magnetic disorder

Here we numerically investigate if magnetic disorder, i.e., disorder that may arise from magnetic adatoms and alters the spin of scattered electrons, can lead to a transition from a trivial to topological insulator. The magnetic-disorder Hamiltonian is

$$H' = W \sum_i \varepsilon_i c_i^\dagger m_i c_i, \quad (5.11)$$

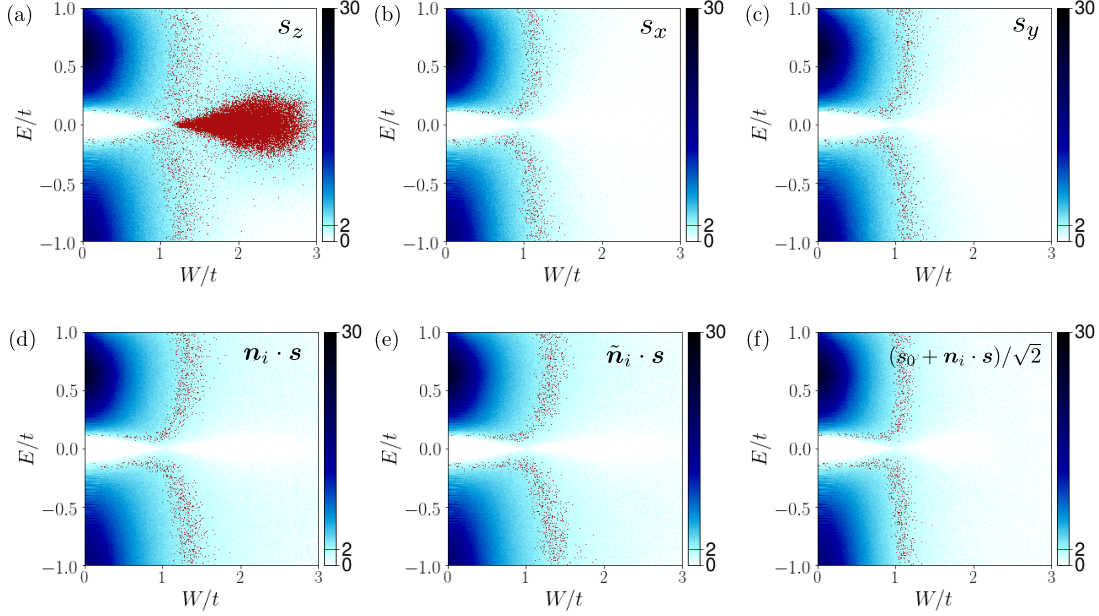


FIGURE 5.7: Conductance maps as in Fig. 5.3 for various choices of matrix  $m_i$  for  $\lambda_\nu = 1.65t$ ,  $\lambda_{\text{SO}} = 0.3t$ , and  $\lambda_R = 0$ . (a) The TAI phase (red region of quantized conductance) is realized only in the case when  $m_i = s_z$ . (b-f) The disorder term for these choices of  $m_i$  (indicated in the upper right corner) does not commute with the KM Hamiltonian and no TAI phase can be seen.

where, as previously,  $W$  is the disorder strength and  $\varepsilon_i \in [-1, 1]$  are uniformly distributed random variables at each site  $i$ . The new feature is the  $2 \times 2$  matrix in spin space,  $m_i$ . In the previous sections of this chapter we focused on the case  $m_i = s_0$ .

Here, we calculate conductance maps for different choices of  $m_i$ . The results are shown in Fig. 5.7 for  $\lambda_\nu = 1.65t$ ,  $\lambda_{\text{SO}} = 0.3t$ , and  $\lambda_R = 0$ . In the upper three conductance maps we use  $m_i \in \{s_z, s_x, s_y\}$ . Only the case with  $m_i = s_z$  leads to the TAI phase. One could expect that if we mix all the Pauli matrices, on average, we will restore the spin symmetry of the disorder and obtain the TAI phase. That this is not the case can be seen in the lower row of the figure. Here,  $m_i \in \{\mathbf{n}_i \cdot \mathbf{s}, \tilde{\mathbf{n}}_i \cdot \mathbf{s}, (\mathbf{s}_0 + \mathbf{n}_i \cdot \mathbf{s})/\sqrt{2}\}$ , where  $\mathbf{n}_i = (\sin \theta_i \cos \phi_i, \sin \theta_i \sin \phi_i, \cos \theta_i)^T$  is the unit vector pointing in a random direction on a sphere and  $\tilde{\mathbf{n}}_i$  is the unit vector pointing in direction along the  $x$  or  $y$  or  $z$  axis randomly on each site. We conclude that only a disorder term for which  $[H', H] = 0$  leads to the TAI phase.

### 5.6.2 Sparse disorder

Anderson disorder is a special model for disorder which is not necessarily representative for all TI materials. To better understand the effect of the disorder model, we briefly remark on the following disorder Hamiltonian

$$H' = \frac{W}{\sqrt{3}} \sum_i \eta_i c_i^\dagger c_i. \quad (5.12)$$

In contrast to the Anderson disorder model, where a random potential is assigned to *every* lattice site, here the distribution function for  $\eta_i$  is such that only a fraction  $0 < \rho \leq 1$  of the sites are affected by disorder. Denoting the total number of sites by  $N$ , we assume  $\eta_i = 1$  on  $\rho N/2$  sites,  $\eta_i = -1$  on  $\rho N/2$  sites, and  $\eta_i = 0$  on the remaining sites. The disorder amplitude  $W$  is constant. Because  $\langle \eta_i^2 \rangle = \rho$ , the normalization factor in Eq. (5.12) ensures that the mean squared disorder strength is equal to the Anderson disorder case for  $\rho = 1$ .

For general  $\rho$ , the prefactor in Eq. (5.5) is thus replaced by  $\rho W^2/3$ . The lowest-order Born approximation for the disorder model (5.12) therefore predicts that a reduced disorder density  $\rho$  can be exactly compensated by an increased amplitude  $W$ . For large enough  $\rho$ , this is indeed confirmed in the tight-binding simulations.

However, because a single impurity ( $\rho = 1/N$ ) cannot destroy the topological phase, it is clear that the TAI phase should eventually vanish for  $\rho \rightarrow 0$  at arbitrary  $W$ . Nevertheless, we find numerical evidence for the TAI phase at surprisingly low impurity densities. A TAI region remains pronounced for densities as low as  $\rho = 0.1$ .

## 5.7 Conclusion

Using a combination of an analytical approach and tight-binding simulations, we have established that the topological Anderson insulator appears in the Kane-Mele model that describes potential topological insulators such as silicene, germanene, and stanene and that can also be realized in optical lattices. We have observed a transition from a trivially insulating phase to a topological phase at a finite disorder strength and have mapped out the phase diagram as a function of the staggered sublattice potential ( $\sim \lambda_\nu$ ) and the Rashba spin-orbit coupling ( $\sim \lambda_R$ ). The new Anderson insulator exists at the boundary between trivial and topological insulators for small  $\lambda_R$  and finite  $\lambda_\nu$ , but not at the boundary between a semimetal and a topological insulator for small  $\lambda_\nu$  and finite  $\lambda_R$ . Additionally, we found that magnetic disorder does not induce the transition from trivial to topological phase unless it commutes with Hamiltonian. Since the Kane-Mele model on a honeycomb lattice describes a wide class of candidate materials for topological insulators, we hope that our work will trigger experimental efforts to confirm the existence of the topological Anderson insulator.

## Part II

# Quantum transport in a junction between interacting cold atomic Fermi gases



## CHAPTER 6

# THERMOELECTRICITY IN A JUNCTION BETWEEN INTERACTING COLD ATOMIC FERMIONIC GASES

*The results presented in this chapter were published in*

T. Sekera, C. Bruder, and W. Belzig

*Thermoelectricity in a junction between interacting cold atomic Fermi gases*

Phys. Rev. A **94**, 033618 (2016).

*Changes have been made to better embed this work into the thesis. The introduction was expanded.*

A gas of interacting ultracold fermions can be tuned into a strongly interacting regime using a Feshbach resonance. Here, we theoretically study quasiparticle transport in a system of two reservoirs of interacting ultracold fermions on the BCS side of the BCS-BEC crossover coupled weakly via a tunnel junction. Using the generalized BCS theory, we calculate the time evolution of the system that is assumed to be initially prepared in a nonequilibrium state characterized by a particle number imbalance or a temperature imbalance. A number of characteristic features like sharp peaks in quasiparticle currents or transitions between the normal and superconducting states are found. We discuss signatures of the Seebeck and the Peltier effects and the resulting temperature difference of the two reservoirs as a function of the interaction parameter  $(k_F a)^{-1}$ . The Peltier effect may lead to an additional cooling mechanism for ultracold fermionic atoms.

### 6.1 Introduction: cold fermionic atoms

A cloud of ultracold atoms potentially allows for an experimental realization of a system that reproduces physics of a precisely defined Hamiltonian. It can, therefore, play the role of a quantum simulator [13]. The advantage is that such a quantum simulator may allow to access information about complex many-body states [125] or about transport [126] in solid-state systems that is usually inaccessible by classical computer simulation.

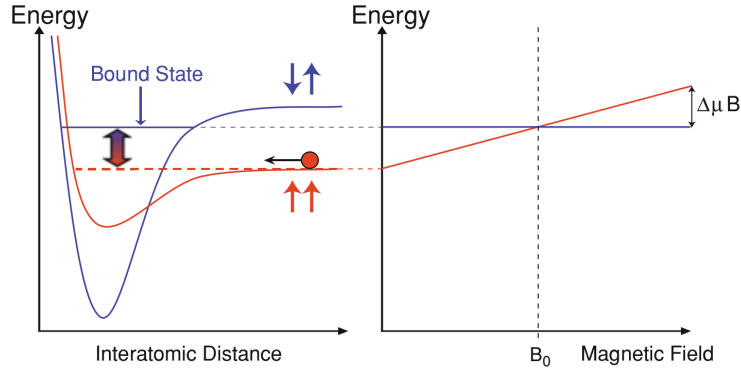


FIGURE 6.1: (a) Open triplet channel (red) slightly detuned from the bound state in the closed singlet channel (blue). (b) The energy difference  $\Delta\mu B$  between the open channel and the closed-channel bound state can be tuned via an external magnetic field ( $\Delta\mu$  is the difference in the magnetic moments of the two channels). Reproduced from Ref. [127].

### Interaction tunability

In condensed-matter systems, the interaction between electrons is fixed by the material parameters and cannot be tuned. The situation is different in a gas of alkali fermionic atoms, such as  $^{40}\text{K}$  and  $^6\text{Li}$ , that have a single outermost electron in an s-orbital. A dilute gas of such atoms can be laser-trapped and cooled down to the regime, where the interatomic interaction between the atoms can be tuned. Even though this interaction can be a complicated function of the interatomic distance in general, due to the diluteness of the gas, it can be represented by a single number: the s-wave scattering length  $a$ .<sup>1</sup>

In a superconducting system described by the mean-field theory of Bardeen-Cooper-Schrieffer (BCS) [128], the effective attractive interaction leads to the formation of Cooper pairs that are composed of spin up and spin down fermions. The two different fermionic species in the case of cold atomic gases are two different hyperfine states, often called spin up and spin down as well. The phenomenon allowing for a tunable interaction between the two atoms of different species is called *Feshbach resonance* [129], which we will now briefly describe. Take the specific case of  $^6\text{Li}$ , where the two hyperfine species are  $m_J = 1/2$ ,  $m_I = 1/2$  and  $-1/2$ , where  $m_I$  ( $m_J$ ) is the total nuclear (electronic) angular momentum. In the presence of a magnetic field ( $> 0.05$  T), the real electron spin of a lithium atom is aligned with the direction of the field. Two atoms colliding in a triplet configuration (open channel) can be in resonance with the singlet bound state in the closed channel, see Fig. 6.1. Due to the hyperfine interaction between electron spin and nuclear spin the two channels can mix. Additionally, because the magnetic moments of the open and closed channels are different, one can tune the system into the resonance via an external magnetic field  $B$ . This leads to a scattering length given by

$$a = a_{BG}[1 - \Delta B/(B - B_0)] \quad (6.1)$$

<sup>1</sup>The letter  $a$  should not be confused with the symbol for the lattice constant defined in Part I of the thesis.



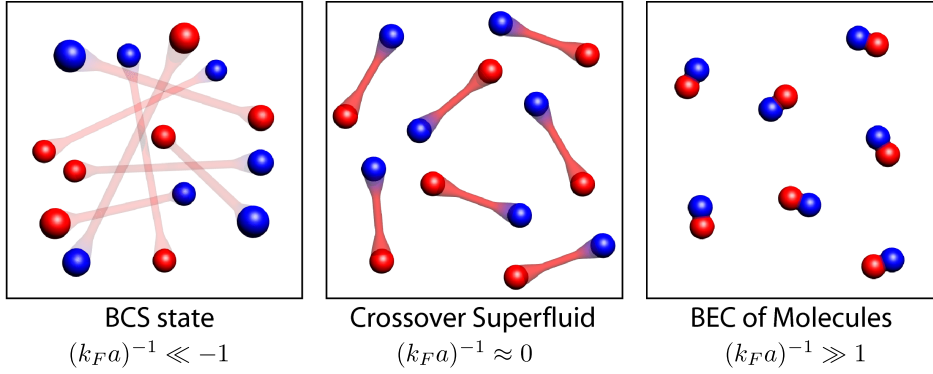


FIGURE 6.2: BCS-BEC crossover. The interaction parameter  $(k_F a)^{-1}$  is swept from large negative to large positive values (from left to right). Adapted from Ref. [131].

in the vicinity of the resonance [127, 130]. Here,  $a_{BG}$  is the background value of the scattering length in the absence of coupling to the closed channel,  $B_0$  is the field at which the resonance occurs and  $\Delta B$  is the width of the resonance.

It is convenient to describe the interaction via the dimensionless parameter  $(k_F a)^{-1}$ . Then, by tuning the magnetic field, one can in principle sweep the interaction parameter from large negative values (BCS state) to large positive values (BEC state). The BCS state is characterized by largely overlapping Cooper pairs, while the BEC state is a condensate of tightly-bound two atomic “molecules”. There is a smooth transition (BCS-BEC crossover) between the two limiting cases, and at  $(k_F a)^{-1} = 0$  the unitary Fermi gas takes place. These regimes are schematically shown in Fig. 6.2.

## Transport

Thermal transport is an important tool to investigate many-body systems. There is a variety of transport coefficients describing the heat carried by thermal currents as well as the voltages (in the case of charged particles) or chemical potential differences (in the case of neutral particles) induced by a thermal gradient (Seebeck effect). The inverse effect, the build-up of a thermal gradient by a particle current is of great practical importance (Peltier effect). These thermoelectric effects depend in sensitive ways on the excitation spectrum of the system close to the Fermi surface [132, 133]. If the spectrum is particle-hole symmetric (as it is to a good approximation in the bulk of a metallic superconductor), the Seebeck effect vanishes. Breaking this symmetry in superconducting tunnel junctions allows for refrigeration [134] and/or giant thermoelectric effects [135–137].

In recent years, transport in ultracold atomic gases has been investigated both theoretically [138–142] and in a number of experiments [143–147]. Optical potentials were used to realize a narrow channel connecting two macroscopic reservoirs of neutral fermionic atoms to form an atomic analogue of a quantum mesoscopic device. Ohmic conduction in such a setup was observed [143] as well as conductance plateaus at integer multiples of the conductance quantum  $1/h$  for a ballistic channel [146]. Tuning the interaction between the atoms by a magnetic field via a Feshbach resonance allowed to drive the system into the superfluid regime. The resulting drop of the resistance was observed

experimentally [144]. Moreover, a quantum point contact between two superfluid reservoirs was realized [147]. Signatures of thermoelectric effects were observed in the normal state of these systems [145]. Several theoretical studies also examined mesoscopic transport [141], thermoelectric effects [148], and Peltier cooling in ultracold fermionic quantum gases [149, 150]. For a recent review on this topic see Ref. [126].

In this chapter, we investigate the coupling of thermal and particle currents in a junction of two superfluids. The goal is to explore the possibility to realize dynamical heating and refrigeration phenomena around the phase transition. To this end, we consider two reservoirs of interacting ultracold atoms connected by a weak link that we model as a tunnel junction. The generalized BCS theory [130] provides self-consistency equations for the gap parameter and the chemical potential as a function of the dimensionless interaction parameter  $(k_F a)^{-1}$ . We use the tunneling approach to describe quasiparticle transport in a system with a fixed number of particles and specify the initial particle and/or temperature imbalance of the two reservoirs. The resulting time evolution of the system shows a number of characteristic features: we find transitions between superfluid and normal states as well as signatures of the Peltier and Seebeck effects. In addition, there are peaks in the transport current that can be related to a resonant condition in the expression for the tunneling current.

The rest of this chapter is organized as follows: In Sec. 6.2 we introduce a model Hamiltonian for the system consisting of two tunnel-coupled reservoirs as well as the self-consistency equations for the superconducting gap and the chemical potential in the generalized BCS theory. We also give expressions for the particle and the heat current. In Sec. 6.3 we calculate the time evolution of the system with a fixed total number of particles initially prepared with an imbalance in particle number and/or temperature. Finally, we conclude in Sec. 6.4.

## 6.2 Model: tunneling Hamiltonian

Our system, depicted in Fig. 6.3, consists of two reservoirs of interacting neutral fermionic atoms connected by a weak link that is modeled by a tunnel junction. Experimentally, the junction can be realized as a constriction in space using trapping lasers. We denote the number of particles and temperature in the left (right) reservoir as  $N_{L(R)}$  and  $T_{L(R)}$ , respectively.

The Hamiltonian describing this system is assumed to be

$$H = H_L + H_R + H_t, \quad (6.2)$$

where  $H_L$  and  $H_R$  are the BCS Hamiltonians for the two reservoirs

$$\begin{aligned} H_L &= \sum_{p\sigma} \xi_p c_{p\sigma}^\dagger c_{p\sigma} + \frac{1}{2} \sum_{pp'\sigma} V_{pp'} c_{p\sigma}^\dagger c_{-p-\sigma}^\dagger c_{-p'-\sigma} c_{p'\sigma}, \\ H_R &= \sum_{k\sigma} \xi_k a_{k\sigma}^\dagger a_{k\sigma} + \frac{1}{2} \sum_{kk'\sigma} V_{kk'} a_{k\sigma}^\dagger a_{-k-\sigma}^\dagger a_{-k'-\sigma} a_{k'\sigma}. \end{aligned} \quad (6.3)$$

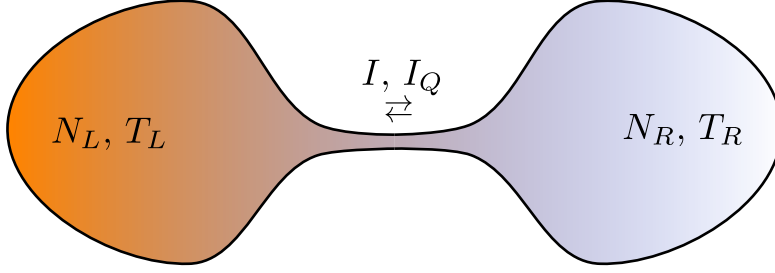


FIGURE 6.3: Two reservoirs of ultracold fermions connected via a tunnel junction allowing particle and heat transport. Each reservoir is characterized by the particle number  $N$  and temperature  $T$ .

Here,  $c_{p\sigma}$  and  $c_{p\sigma}^\dagger$  ( $a_{p\sigma}$  and  $a_{p\sigma}^\dagger$ ) are the annihilation (creation) operators of a fermion with momentum  $p$  and spin  $\sigma$  in the left (right) reservoir,  $\xi_p = \varepsilon_p - \mu$  is the single-particle energy with respect to the chemical potential, and  $V_{pp'}$  is the (singlet) pairing interaction. In the context of neutral fermionic atoms the spin degree of freedom is represented by the two hyperfine states of the atom in consideration. The tunneling Hamiltonian is

$$H_t = \sum_{kp\sigma} \eta_{kp} a_{k\sigma}^\dagger c_{p\sigma} + h.c. , \quad (6.4)$$

where  $\eta_{kp}$  is the tunneling matrix element, which in the following we assume to be energy independent,  $|\eta_{kp}|^2 = |\eta|^2$ .

In the next step, we restrict ourselves to the mean-field approximation for the Hamiltonians in Eq. (6.3) introducing the mean-field parameter  $\Delta_L$  for the left reservoir

$$\Delta_{p\sigma-\sigma} = - \sum_{p'} V_{pp'} \langle c_{-p'-\sigma} c_{p'\sigma} \rangle \approx \Delta_L \quad (6.5)$$

and analogously for the right reservoir.

In a dilute gas of neutral fermionic atoms it is a good approximation to describe the interaction  $V_{pp'}$  between two atoms using a single parameter, the s-wave scattering length  $a$ . Consequently, the dimensionless interaction parameter  $(k_F a)^{-1}$  can be included in the BCS gap equation using a standard renormalization procedure (see, e.g. Appendix 8A of Ref. [130]). The gap equation then takes the form

$$\frac{\pi}{k_F a} \sqrt{\varepsilon_F} = \int_0^\infty d\varepsilon \sqrt{\varepsilon} \left[ \frac{1}{\varepsilon} - \frac{1}{E} \tanh \left( \frac{E}{2T} \right) \right], \quad (6.6)$$

where  $E = \sqrt{(\varepsilon - \mu)^2 + |\Delta|^2}$  and  $\varepsilon_F$  is the Fermi energy. In Eq. (6.6), there are two unknown variables  $\mu$  and  $\Delta$ . To solve it, the second equation is obtained by fixing the number of particles

$$\frac{4}{3} \varepsilon_F^{3/2} = \int_0^\infty d\varepsilon \sqrt{\varepsilon} \left[ 1 - \frac{\varepsilon - \mu}{E} \tanh \left( \frac{E}{2T} \right) \right]. \quad (6.7)$$

For the density of states (DOS) of a 3D Fermi gas in the normal state  $\mathcal{N}^0(\varepsilon) \propto \sqrt{\varepsilon}$  (neglecting the confining potential) which we used above, the integrals in Eqs. (6.6)

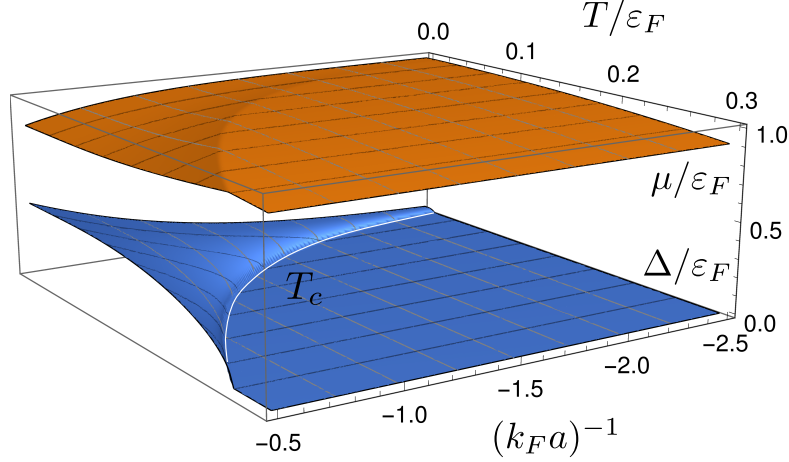


FIGURE 6.4: (Color online) Solution for  $\Delta$  (lower blue surface) and  $\mu$  (upper orange surface) following from Eqs. (6.6) and (6.7) as a function of  $(k_F a)^{-1}$  and  $T$ . The mean-field critical temperature  $T_c$  is highlighted in the lower surface as a white curve. In the BCS limit  $(k_F a)^{-1} \rightarrow -\infty$ , the chemical potential  $\mu/\varepsilon_F \rightarrow 1$  and  $\Delta$  as well as  $T_c$  approach zero.

and (6.7) converge and no cut-off energy needs to be introduced. The solution to these equations is shown in Fig. 6.4 as a function of temperature  $T$  and interaction parameter  $(k_F a)^{-1}$ . As the interaction parameter approaches the BCS limit,  $(k_F a)^{-1} \ll -1$ , the superconducting gap  $\Delta$  and critical temperature  $T_c$  are proportional to  $e^{-\pi/(2k_F a)}$  and  $\mu/\varepsilon_F \rightarrow 1$  at  $T = 0$  [130]. On the other hand, towards unitarity, where  $(k_F a)^{-1} \rightarrow 0^-$ ,  $\Delta$  and  $T_c$  increase and  $\mu$  decreases.

Note that this mean-field critical temperature  $T_c$  is, in fact, the pairing temperature below which a significant number of fermions are bound in pairs. In the BCS limit the real critical temperature and mean-field  $T_c$  coincide, however, closer to the unitary regime, this approximation starts to fail.

An initial state with particle number imbalance or temperature imbalance between the left and right reservoirs will give rise to particle and heat transport. The particle current  $I$  and energy current  $I_{\mathcal{E}}$  are defined as

$$\begin{aligned} I &= -\frac{\partial \langle \hat{N}_L \rangle}{\partial t} = i \langle [\hat{N}_L, H] \rangle, \\ I_{\mathcal{E}} &= -\frac{\partial \langle H_L \rangle}{\partial t} = i \langle [H_L, H] \rangle, \end{aligned} \quad (6.8)$$

where the angular brackets represent the thermodynamic average in the grandcanonical ensemble and  $\hat{N}_L = \sum_{p\sigma} c_{p\sigma}^\dagger c_{p\sigma}$  is the fermion number operator in the left reservoir. All the operators are in the Heisenberg picture. These expressions for the currents are general. The commutator on the right-hand side of Eq. (6.8) leads to terms describing quasiparticle tunneling and Cooper-pair tunneling, see e.g. Ref. [151] for the explicit evaluation of the particle current and the appendix of Ref. [152] for the evaluation of the heat current. In the following, we restrict ourselves to quasiparticle transport (i.e., ignore terms corresponding to Cooper-pair tunneling). Consequently, the expressions

for the particle and heat current in the tunneling limit read

$$\begin{aligned} I &= I_{L \rightarrow R} - I_{R \rightarrow L} \\ &= \frac{2\pi|\eta|^2}{\hbar} \mathcal{V}_L \mathcal{V}_R \int_{-\infty}^{\infty} dE \mathcal{N}_L(E) \mathcal{N}_R(E) [f_L(E) - f_R(E)] \end{aligned} \quad (6.9)$$

and

$$\begin{aligned} I_Q &= I_{Q,L \rightarrow R} - I_{Q,R \rightarrow L} \\ &= \frac{2\pi|\eta|^2}{\hbar} \mathcal{V}_L \mathcal{V}_R \int_{-\infty}^{\infty} dE \mathcal{N}_L(E) \mathcal{N}_R(E) \\ &\quad \times [(E - \mu_L) f_L(E) (1 - f_R(E)) - (E - \mu_R) f_R(E) (1 - f_L(E))] . \end{aligned} \quad (6.10)$$

Here,  $\mathcal{V}_{L(R)}$  is the volume and  $f_{L(R)}(E)$  the Fermi function describing the left (right) reservoir. The superconducting density of states

$$\mathcal{N}_{L(R)}(E) = \text{Re} \{ \mathcal{N}_{L(R)}^0(\varepsilon) \} \text{Re} \left\{ \frac{|E - \mu_{L(R)}|}{\sqrt{(E - \mu_{L(R)})^2 - \Delta_{L(R)}^2}} \right\}$$

contains the energy-dependent density of states  $\mathcal{N}_{L(R)}^0$  of a normal 3-dimensional Fermi gas that can be expressed as

$$\begin{aligned} \mathcal{N}_{L(R)}^0(\varepsilon) &= \frac{1}{2\pi^2} \left( \frac{2m}{\hbar^2} \right)^{3/2} \sqrt{\varepsilon} \\ &= \frac{1}{2\pi^2} \left( \frac{2m}{\hbar^2} \right)^{3/2} \sqrt{\mu_{L(R)} + \text{sign}(E - \mu_{L(R)}) \text{Re} \sqrt{(E - \mu_{L(R)})^2 - \Delta_{L(R)}^2}} . \end{aligned}$$

The quasiparticle currents (6.9) and (6.10) can be understood already on a phenomenological level: the first term in Eq. (6.10) describes quasiparticles with energy  $(E - \mu_L)$  tunneling with probability  $|\eta|^2$  from the left to right reservoir while the second term describes quasiparticles with energy  $(E - \mu_R)$  tunneling from the right to left reservoir. Similar considerations lead to Eq. (6.9) for the particle current: the terms involving products of Fermi functions of the left and right reservoirs cancel.

### 6.3 Time evolution of the system

For finite reservoirs, which is the case we are studying here, a non-equilibrium initial state (like a temperature or particle number imbalance between the left and right reservoir) will induce time-dependent transport [141, 148, 149]. To model this phenomenon we consider the balance equations for the particle number  $N_{L(R)}$  and energy  $\mathcal{E}_{L(R)}$  in each reservoir that lead to

$$\begin{aligned} \frac{\partial N_{L(R)}}{\partial t} &= \mp I, \\ \frac{\partial \mathcal{E}_{L(R)}}{\partial t} &= \mp \frac{1}{C_{\mathcal{V}_{L(R)}}} (I_Q + \mu_L I_{L \rightarrow R} - \mu_R I_{R \rightarrow L}) . \end{aligned} \quad (6.11)$$

Here, we used the relation between the energy of the left (right) reservoir and temperature change of the system at constant volume  $C_V = \partial \mathcal{E} / \partial T$ . The heat capacity in the (generalized) BCS theory described by Eqs. (6.6) and (6.7) is given by

$$C_V(T) = \frac{2}{T} \int_{-\infty}^{\infty} dE \mathcal{N}(E) \left( -\frac{\partial f(E)}{\partial E} \right) \times \left( E^2 - \frac{T}{2} \frac{\partial \Delta^2}{\partial T} + T \text{sign}(E) \sqrt{E^2 - \Delta^2} \frac{\partial \mu}{\partial T} \right). \quad (6.12)$$

In writing Eqs. (6.11) and (6.12), we have neglected number and energy fluctuations in the reservoirs which were shown to be small in the regime considered here [153].

To calculate the time evolution of the system, we proceed as follows: starting with  $N_{L(R)}(t) = N \pm \delta N/2$  and  $T_{L(R)}(t) = T \pm \delta T/2$  at time  $t$ , we calculate the corresponding values of  $\mu_{L(R)}(t)$  and  $\Delta_{L(R)}(t)$  using Eqs. (6.6) and (6.7). Then, using the discretized form of Eq. (6.11), we obtain  $N_{L(R)}(t + \delta t)$  and  $T_{L(R)}(t + \delta t)$  at time  $t + \delta t$ , and the procedure is iterated. The time evolution is hence uniquely determined by setting initial values of  $N_{L(R)}^0$ ,  $T_{L(R)}^0$  and  $(k_{F,L}^0 a)^{-1}$ , where quantities with superscript 0 denote the values at time  $t = 0$ . The interaction parameter on the right side follows from  $(k_{F,L}^0 a)^{-1}$  and  $N_R^0$ . Note that in linear response in  $\delta N$  and  $\delta T$ , assuming  $\Delta_L = \Delta_R = 0$  and  $C_V$  = constant, Eqs. (6.11) can be solved analytically using simple exponential functions[148]. For example, an initial particle number imbalance will decay exponentially with time.

Typically, starting with an initial particle number (temperature) imbalance  $\delta N_0$  ( $\delta T_0$ ) will lead to a time-dependent temperature (particle number) imbalance due to the coupling between particle and heat transport. As a consequence, the chemical potential imbalance  $\delta \mu = \mu_L - \mu_R$  and  $\delta \Delta = \Delta_L - \Delta_R$  will also depend on time. Eventually, as  $t \rightarrow \infty$ , the system reaches an equilibrium state.

In the following we show and discuss three examples of such a time evolution displaying various quantities characterizing the system as a function of time. The time scale in Figs. 6.5–6.7 is fixed as follows: time can be expressed in units of  $\varepsilon_b \hbar / |\eta|^2$ , where  $\varepsilon_b = \hbar^2 / (2ma^2)$  and  $|\eta|^2 = |\eta_{kp}|^2$  is the modulus squared of the tunneling matrix element introduced after Eq. (6.4). As mentioned earlier, the time evolution of a system in the normal state within linear response corresponds to an exponential decay of the initial particle number imbalance. To get an order-of-magnitude estimate for the absolute time scale in seconds, we compare our results for the dimensionless linear response coefficient  $1/\tilde{\tau}$  in  $\tilde{I} = \delta N / \tilde{\tau}$ , where the tilde denotes dimensionless quantities, with the experimental value  $1/\tau_0 = 2.9 \text{ s}^{-1}$  taken from Ref. [143]. This leads to relation

$$\frac{\varepsilon_b \hbar}{|\eta|^2} = \tau_0 / \tilde{\tau}.$$

The time scale  $\tau_0$  represents a characteristic particle transport time scale and is analogous to the  $RC$ -time of a capacitor circuit.

Figure 6.5 demonstrates a case in which a sharp peak in the current as a function of time appears. This can be understood in the semiconductor picture of the tunneling

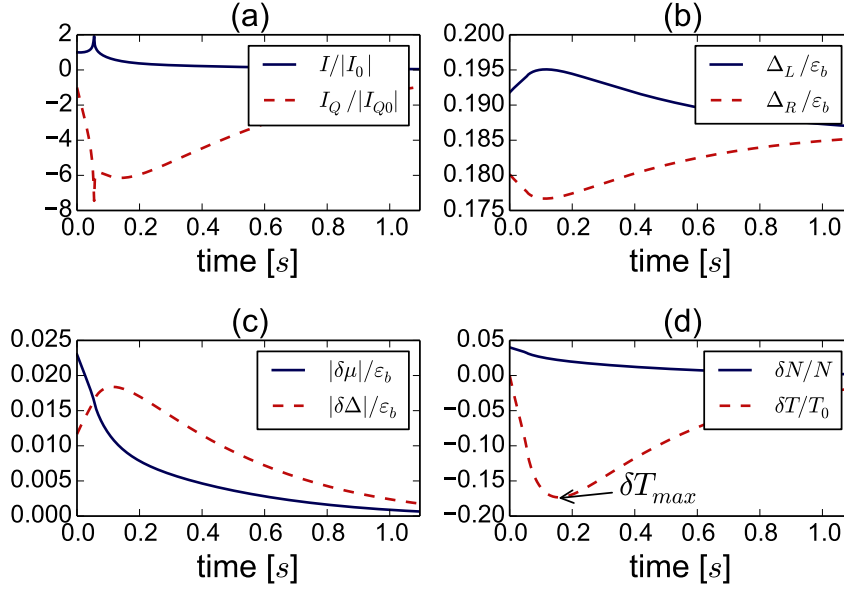


FIGURE 6.5: Time evolution of various quantities: (a) particle current ( $I$ ) and heat current ( $I_Q$ ), (b) superconducting gap in the left ( $\Delta_L$ ) and right ( $\Delta_R$ ) reservoir, (c) chemical potential difference ( $\delta\mu$ ) and difference between gaps in the left and right reservoir ( $\delta\Delta$ ), (d) particle number difference ( $\delta N$ ) and temperature difference ( $\delta T$ ). The sharp peak in the currents occurs for the time  $t$  at which  $|\delta\mu| = |\Delta_L - \Delta_R|$ , *i.e.*, when thermally excited quasiparticles are allowed to tunnel between the peaks in the DOS of the two reservoirs. The initial conditions chosen are  $N = 2 \times 10^4$ ,  $\delta N_0/N = 0.04$ ,  $T_L^0 = T_R^0 = T_0 = 0.07\varepsilon_b$ , and  $(k_{F,L}^0 a)^{-1} = -1$ .

process: the BCS DOS at the edges of the gap,  $E = \pm\Delta$ , in both reservoirs is divergent, provided that both reservoirs are in the superfluid regime. Hence, if the condition  $|\delta\mu(t)| = |\Delta_L(t) - \Delta_R(t)|$  is satisfied, electrons from a peak in the DOS of one reservoir are allowed to tunnel into the peak in the DOS of the other reservoir. This condition creates a logarithmic singularity in the integrals in Eqs. (6.9), (6.10) (in the absence of gap anisotropy and level broadening) [154]. Moreover, a time-dependent temperature imbalance  $\delta T(t)$  develops that exhibits a non-monotonic behavior and reaches its maximum value  $\delta T_{max}$  at a certain time, see Fig. 6.5(d). The build-up of this temperature imbalance is a signature of the Peltier effect. For the case shown in Fig. 6.5 the initial conditions are chosen such that both reservoirs are in the superfluid regime throughout the time evolution:  $N = 2 \times 10^4$ ,  $\delta N_0/N = 0.04$ ,  $T_L^0 = T_R^0 = T_0 = 0.07\varepsilon_b$ ,  $(k_{F,L}^0 a)^{-1} = -1$ . The corresponding initial values of  $T_c^0$  are  $T_{c,L}^0 = 0.125\varepsilon_b$  and  $T_{c,R}^0 = 0.119\varepsilon_b$ .

In Fig. 6.6 we choose a negative initial particle number imbalance  $\delta N_0/N = -0.04$  (while keeping  $(k_{F,L}^0 a)^{-1} = -1$ ) and an initial temperature  $T_L^0 = T_R^0 = T_0 = 0.1248\varepsilon_b$  that lies between the initial transition temperatures of the two reservoirs. Since  $T_{c,L}^0 = 0.119\varepsilon_b$  and  $T_{c,R}^0 = 0.125\varepsilon_b$  in this case, the left reservoir is initially normal and the right one superfluid. During the time evolution, the left reservoir undergoes a transition to a superfluid state as shown in Fig. 6.6(b). Interestingly, this is not caused by lowering the temperature in the left reservoir. On the contrary, the temperature in the left reservoir actually temporarily rises. But the particle number (and hence the density) in the left

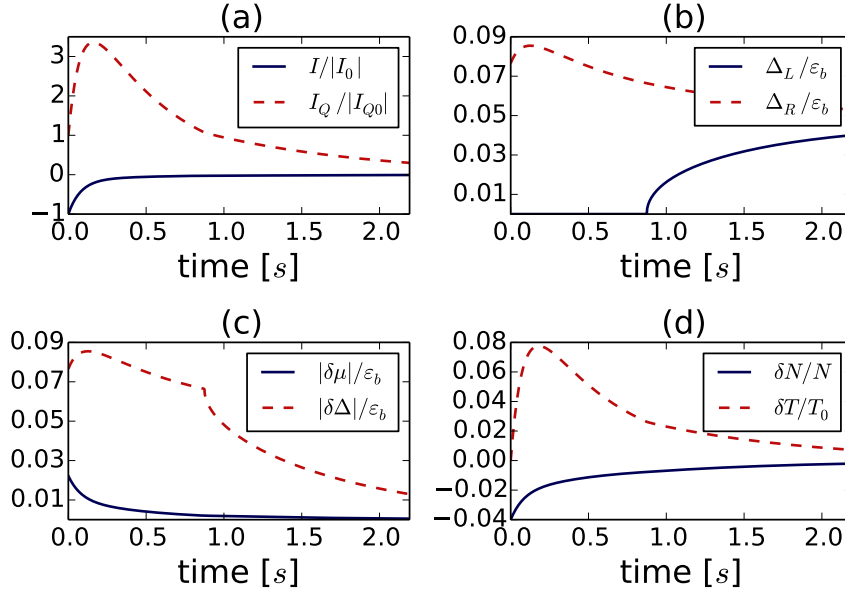


FIGURE 6.6: Time evolution of the same quantities as in Fig. 6.5. A negative initial particle number imbalance and an initial temperature between the transition temperatures of the two reservoirs leads to a transition of the left reservoir from an initially normal to a superfluid state at intermediate times. The initial conditions are  $N = 2 \times 10^4$ ,  $\delta N_0/N = -0.04$ ,  $T_L^0 = T_R^0 = T_0 = 0.1248 \varepsilon_b$ , and  $(k_{F,L}^0 a)^{-1} = -1$ .

reservoir rises which causes the transition from  $\Delta_L = 0$  to  $\Delta_L \neq 0$ . As before, the calculation was done for  $N = 2 \times 10^4$ .

Figure 6.7 shows a more complex time evolution. The peaks in the current as a function of time appear for the same reason as in Fig. 6.5(a), but now the condition  $|\delta\mu| = |\Delta_L(t) - \Delta_R(t)|$  is satisfied twice during the time-evolution, see Fig. 6.7(c). The system also undergoes several superfluid transitions similar to Fig. 6.6(b). Finally, when the system equilibrates for  $t \rightarrow \infty$ , both reservoirs end up in the superfluid state. The initial conditions were chosen as  $N = 2 \times 10^4$ ,  $\delta N_0/N = 0.04$ ,  $T_L^0 = 0.132 \varepsilon_b$ ,  $T_R^0 = 0.115 \varepsilon_b$ ,  $T_0 = (T_L^0 + T_R^0)/2$ , and  $(k_{F,L}^0 a)^{-1} = -1$ .

As mentioned earlier, the induced temperature imbalance  $\delta T$  due to an initial particle number imbalance  $\delta N_0$  is a signature of the Peltier effect. It shows a non-monotonous behavior as a function of time with a maximum  $\delta T_{\max}$  at intermediate times, see Figs. 6.5(d) and 6.6(d). In Fig. 6.8 we show  $|\delta T_{\max}|$  as a function of  $(k_{F,L}^0 a)^{-1}$  for different values of the initial particle number imbalance  $\delta N_0$  and initial temperature  $T_L^0 = T_R^0 = T_0$ . Each of the functions is divided into two sections monotonically increasing with increasing  $(k_{F,L}^0 a)^{-1}$ . The left section represents data from a system which is in the normal state,  $\Delta_{L(R)}(t) = 0$ , during the whole time evolution, whereas for the right section  $\Delta_{L(R)}(t) \neq 0$ , as in Fig. 6.5. Between the two sections, there is a “transient” regime, where superfluid transitions occur, similar to the ones in Figs. 6.6 and 6.7. The generalized BCS theory [130] on which our description of the BCS-BEC crossover is based is an approximation that becomes less accurate on approaching the unitary limit. However, the increase of the temperature imbalance starts already at relatively large (negative) values of  $(k_{F,L}^0 a)^{-1} < -2$ . We therefore expect the trend to be qualitatively correct in



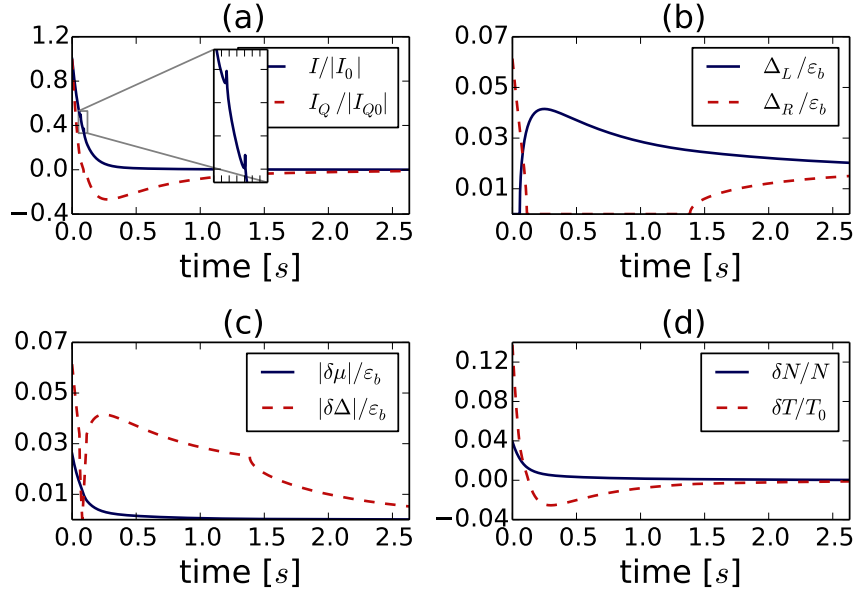


FIGURE 6.7: Time evolution of the same quantities as in Fig. 6.5. The system exhibits several transitions. The peaks in the particle and heat current, zoomed in for the particle current in the inset, are present for the same reason as in Fig. 6.5. In this case the condition  $|\delta\mu| = |\Delta_L - \Delta_R|$  is satisfied twice during the time evolution. The initial conditions are  $N = 2 \times 10^4$ ,  $\delta N_0/N = 0.04$ ,  $T_L^0 = 0.132 \varepsilon_b$ ,  $T_R^0 = 0.115 \varepsilon_b$ ,  $T_0 = (T_L^0 + T_R^0)/2$ , and  $(k_{F,L}^0 a)^{-1} = -1$ .

a region approaching (but not too close) to unitarity. This increase of  $|\delta T_{\max}|$  towards unitarity cannot be explained by particle-hole asymmetry alone but is due to a delicate interplay of the various factors in the integrands of Eqs. (6.9) and (6.10).

## 6.4 Conclusion

To summarize, we have investigated particle and heat transport on the BCS side of the BCS-BEC crossover in a two-terminal setup with two reservoirs of interacting ultracold atoms. We have shown that a system initially out of equilibrium will show particle and/or thermal currents whose existence leads to characteristic time-dependent signatures, such as transitions between normal and superconducting states and resonant features in the currents as a function of time. An initial temperature imbalance can lead to a difference in chemical potentials at intermediate times. This is a signature of the Seebeck effect. Conversely, an initial particle number imbalance for two reservoirs at equal temperatures can lead to the build-up of a temperature difference at intermediate times, which is a signature of the Peltier effect. The maximal induced temperature imbalance increases if  $(k_F a)^{-1}$  moves closer to the unitarity limit.

In conclusion, this chapter points out a variety of dynamical features visible in the equilibration process that can be used to pin-point the parameters of the system. An experimental confirmation of the Peltier effect discussed here is important since an additional cooling mechanism for ultracold fermionic atoms will be a valuable resource.

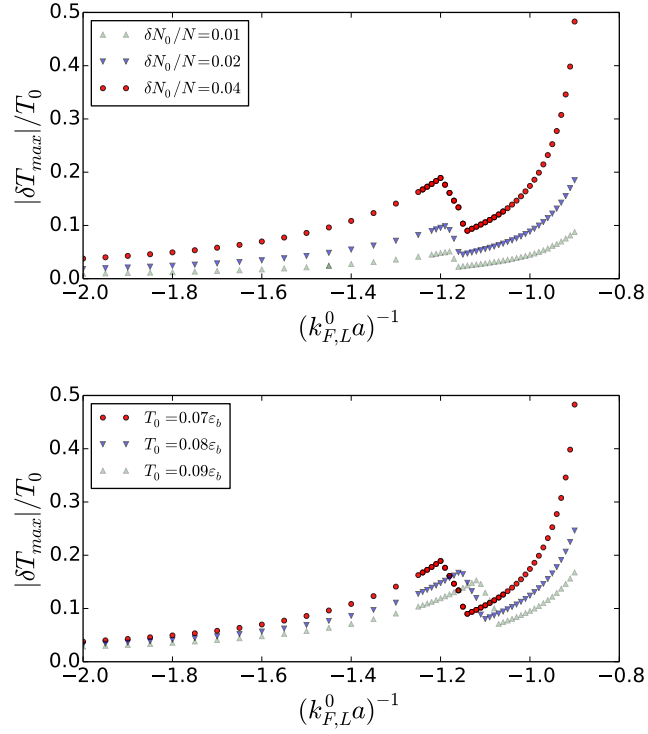


FIGURE 6.8: Maximal induced temperature imbalance  $|\delta T_{\max}|$  as a function of  $(k_{F,L}^0 a)^{-1}$  for different values of the initial particle number imbalance  $\delta N_0$  and initial temperature  $T_L^0 = T_R^0 = T_0$ . Upper panel:  $N = 2 \times 10^4$ ,  $T_0 = 0.07 \epsilon_b$ , and three different values of  $\delta N_0/N$ . Lower panel:  $N = 2 \times 10^4$ ,  $\delta N_0/N = 0.04$ , and three different values of  $T_0$ . The Peltier effect gets more significant approaching the unitary point.

Furthermore, transport experiments in systems of ultracold atoms provide a fascinating laboratory in which the combination of particle and thermal currents can be explored in a regime that is not accessible to experiments with metallic superconductors.

## CHAPTER 7

## SUMMARY

We studied quantum transport of fermionic particles in several systems. In Chapters 3-5 we dealt with transport of electrons in two-dimensional systems with a honeycomb lattice structure, out of which graphene is the most famous one.

In Chapter 3 we studied the valley polarization of current in a three-terminal device based on a graphene  $p$ - $n$  junction in a uniform quantizing magnetic field. Valley, additionally to the spin and charge, is a new degree of freedom for electrons in graphene. It arises within the low-energy description of excitations in materials based on a honeycomb lattice. The three-terminal device we proposed partitions the valley-unpolarized current into two branches of valley-polarized currents. Such a valley filter might find its applications in the field of valleytronics.

In Chapter 4 we investigated a junction between graphene and a superconductor. One way to create such a junction is by placing a superconducting electrode on top of a graphene sheet. The superconducting pairing is induced in the sheet via the proximity effect. If the critical field of the superconductor is large enough, such junctions can be studied in the quantum Hall regime, where the current in the normal part is carried by edge states only. We found that in the junction based on graphene there are no magnetoconductance oscillations in a two-terminal device within the zeroth Landau level. This is in stark contrast to junctions based on a two-dimensional electron gas in semiconductor heterostructures. In a three-terminal device, where two leads are in a normal and one in a superconducting state, we find a spin-filtering effect if the spin-degeneracy is lifted by the Zeeman field.

Chapter 5 deals with topological insulators on a honeycomb lattice in the presence of disorder. As a model, we chose the Kane-Mele Hamiltonian, where the spin-orbit coupling opens a topologically non-trivial gap. The relevant materials include silicene, germanene, and stanene. The disorder is represented via random on-site energy. We numerically calculate the differential conductance map as a function of the disorder strength and energy. We found that if the system has a topologically trivial gap for zero disorder strength (two-terminal conductance is zero), it may close and reopen as a topological

one (two-terminal conductance is  $2e^2/h$ ) upon increasing the disorder strength. This is understood via renormalization of the Hamiltonian parameters due to the presence of disorder. Such a disorder-induced topological insulator is called topological Anderson insulator. Investigating the effect of magnetic disorder, we found that the topological Anderson insulator phase takes place only if the disorder term commutes with the Kane-Mele Hamiltonian.

In Chapter 6 we studied transport of Bogoliubov quasiparticles between two reservoirs of ultracold fermionic atoms. In such systems one can tune the strength of interparticle interactions via the Feshbach resonance. This allows sweeping from the Bardeen-Cooper-Schrieffer (BCS) regime of large and overlapping Cooper pairs through the strongly interacting unitary regime to the Bose-Einstein condensate (BEC) regime of tightly-bound pairs. This is known as the BCS-BEC crossover. Using the generalized BCS theory, we calculated the time evolution of the weakly-coupled two-reservoir system that is assumed to be initially prepared in a nonequilibrium state characterized by a particle number imbalance or a temperature imbalance. We found a number of characteristic features like sharp peaks in quasiparticle currents or transitions between the normal and superconducting state.

While the systems studied in this thesis are manifold, they all feature mesoscopic transport of fermions where the quantumness plays a significant role. Research of such systems is not only fundamentally interesting but gains its relevance in technological applications due to increasing demand for miniaturization.

## APPENDIX A

## NUMERICS IN PART I

### A.1 Kwant: an example

The main numerical tool used in the first part of the thesis is the Python package Kwant [30]. Besides highly efficient and stable algorithms, an essential feature of Kwant is its user-friendliness. In other words, “... the way one writes down a Hamiltonian in Kwant is very close to what one would write on a blackboard” [30].

Even though there is plenty of documentation and tutorials on the web [155], we demonstrate here the usage of Kwant by calculating a two-terminal conductance of a graphene sample in the quantum Hall regime with Zeeman field. The Python code below is minimal, and each box represents a jupyter-notebook cell [156].

First, we import libraries (1-5), define the spin Pauli matrices (7-10) and parameters of the system (12-17).

```
1 import kwant, tinyarray
2 from math import pi, sqrt
3 from matplotlib import pyplot as plt
4 from cmath import exp
5 import numpy as np
6
7 s_x = tinyarray.array([[0, 1], [1, 0]])
8 s_y = tinyarray.array([[0, -1j], [1j, 0]])
9 s_z = tinyarray.array([[1, 0], [0, -1]])
10 s_0 = tinyarray.array([[1, 0], [0, 1]])
11
12 t = -1 #nn hopping
13 phi = 0.01 #magnetic flux
14 E_F = 0.0 #Fermi energy
15 Delta_Z = 0.02 #Zeeman field
16 L = 60 #length
17 W = 40 #width
```

Next, we define a function (1) that creates the system: the scattering region and leads. The nearest-neighbor hopping in the presence of a magnetic field (27) is position-dependent but spin-independent. The other two functions defined at lines (33) and (43) serve to calculate the spin-resolved band structure of a lead.

```

1 def make_system():
2     # define the honeycomb lattice
3     lat = kwant.lattice.general([(sqrt(3)*1/2, 1/2), (0, 1)],
4                                [(0, 0), (1/(2*sqrt(3)), 1/2)], norbs = 2)
5
6     def scattering_region(pos):
7         x, y = pos
8         return abs(x) < L/2 and abs(y) < W/2
9
10    def lead_shape(pos):
11        x, y = pos
12        return abs(y) < W/2
13
14    # define the scattering region
15    sys = kwant.Builder()
16    sys[lat.shape(scattering_region, (0,0))] = -E_F * s_0 + Delta_Z * s_z
17    sys[lat.neighbors()] = hopping
18
19    # define the leads
20    sym = kwant.TranslationalSymmetry(lat.vec((-2,1)))
21    L_0 = kwant.Builder(sym, conservation_law = s_z)
22    L_0[lat.shape(lead_shape, (0,0))] = -E_F * s_0 + Delta_Z * s_z
23    L_0[lat.neighbors()] = hopping
24    L_1 = L_0.reversed()
25    return sys, L_0, L_1
26
27 def hopping(sitei, sitej, phi):
28     xi, yi = sitei.pos
29     xj, yj = sitej.pos
30     phaseij = 2 * pi * phi * (xi - xj) * ((yi + yj)/2)
31     return -t * exp(1j * phaseij) * s_0
32
33 def H_k(lead, phi=phi):
34     HL = lead.cell_hamiltonian(params=dict(phi=phi))
35     # get inter-cell hopping and make it a square matrix
36     _V = lead.inter_cell_hopping(params=dict(phi=phi))
37     V = np.empty(HL.shape, dtype=complex) #create HL.shape matrix of
38     uninitialized (arbitrary) data
39     V[:, :_V.shape[1]] = _V
40     V[:, _V.shape[1]:] = 0
41     # return a function that, given 'k', calculates H(k)
42     return lambda k: HL + exp(-1j * k) * V + exp(1j * k) * V.conjugate().
43     transpose()
44
45 def eig(k, projector):
46     Htemp = projector.conjugate().transpose() @ H(k) @ projector
47     eigsys = np.linalg.eigh(Htemp)
48     return eigsys[0]
    
```

We create the system (1). To get a two-terminal system, we attach the leads to the scattering region (3-4) and check if the system looks as intended (6). The output is in Fig. A.1.

```

1 sys, L_0, L_1 = make_system()
2
3 sys.attach_lead(L_0)
4 sys.attach_lead(L_1)
5
6 kwant.plot(sys)
    
```

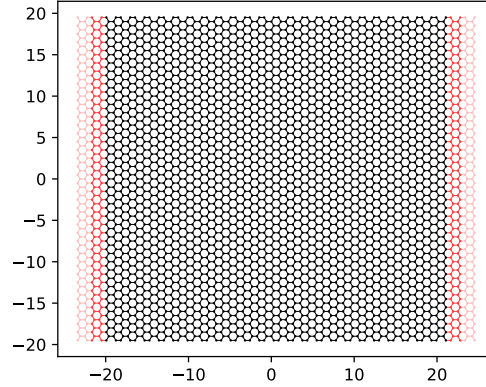


FIGURE A.1: Scattering region (black) with two leads attached (red). Only two unit cells of each of the leads is shown.

Next, we finalize lead L\_0 (1) to make it suitable for numerical calculation. In Kwant, it is very easy to calculate the band structure of the lead (3-5) and plot it (7-11). The output is in Fig. A.2.

```

1 L_0f = L_0.finalized()
2
3 bands = kwant.physics.Bands(L_0f, params = dict(phi = phi))
4 ks = np.linspace(-pi, pi, num = 101)
5 energies = [bands(k) for k in ks]
6
7 f, ax = plt.subplots()
8 ax.plot(ks, energies, 'black')
9 ax.set_ylim(-0.5, 0.5)
10 plt.show()
    
```

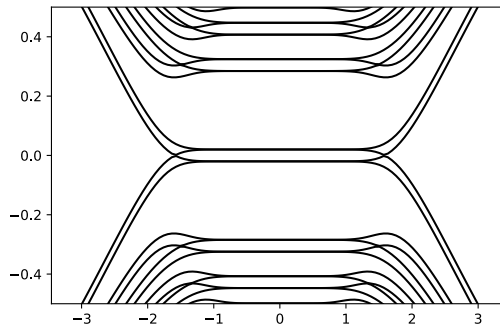


FIGURE A.2: Band structure of lead L\_0.

With the help of the functions  $H.k$  and  $eig$ , we can also calculate (3-7) and plot (9-13) the spin-projected band structure. The output is in Fig. A.3.

```

1 projector_down, projector_up = L_0f.discrete_symmetry().projectors
2 H = H_k(L_0f)
3 ks = np.linspace(-pi, pi, num = 101)
4 bands_down = np.array([eig(k, projector_down) for k in ks])
5 bands_up = np.array([eig(k, projector_up) for k in ks])
6
7 f, ax = plt.subplots()
8 ax.plot(ks, bands_down, 'blue')
9 ax.plot(ks, bands_up, 'red')
10 ax.set_ylim(-0.4, 0.4)
11 plt.show()
    
```

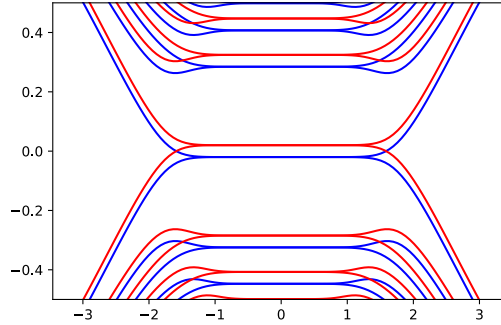


FIGURE A.3: Band structure of lead  $L_0$  with spin resolved bands: spin up (red) and spin down (blue).

It is equally straightforward to calculate the transmission function as a function of energy (4) from the scattering matrix and plot it (8-11). The output is in Fig. A.4.

```

1 sysf = sys.finalized()
2 energies = np.linspace(-0.4, 0.4, 200)
3 T00 = []
4 for energy in energies:
5     smatrix = kwant.smatrix(sysf, energy, params=dict(phi=phi))
6     T00.append(smatrix.transmission((1), (0)))
7
8 f, ax = plt.subplots()
9 ax.plot(energies, T00)
10 plt.tight_layout()
11 plt.show()
    
```

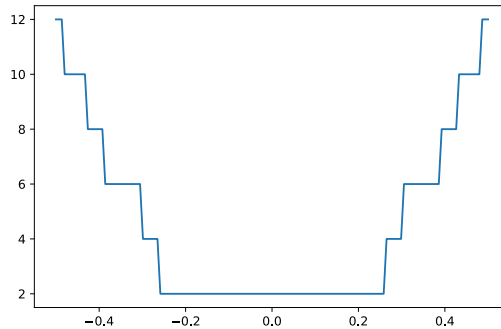


FIGURE A.4: Transmission as a function of energy.

A detailed description of the Kwant methods used above can be found on the web [155] together with plenty other tutorials.



## A note on the ribbon width

Our choice of the coordinate system leads to the following relations between the parameter  $W$  used in the code and the actual width  $W_{\text{act}}$  of the zigzag ribbon

$$\begin{aligned} W_{\text{act}} &= \frac{\sqrt{3}}{2}(a+b) + \frac{1}{2\sqrt{3}}, \\ a &= \left\lfloor \frac{W/2}{\sqrt{3}/2} \right\rfloor, \\ b &= \left\lfloor \frac{W/2 - 1/(2\sqrt{3})}{\sqrt{3}/2} \right\rfloor, \end{aligned} \quad (\text{A.1})$$

and of the armchair ribbon

$$W_{\text{act}} = \lfloor (W/2 - \epsilon)/(1/2) \rfloor, \quad (\text{A.2})$$

where  $\lfloor x \rfloor$  is the floor function. The relative difference

$$\delta W = \frac{W_{\text{act}} - W}{W_{\text{act}} + W} \quad (\text{A.3})$$

vanishes as the system size is increased, as is shown in Figs. A.5(c-d).

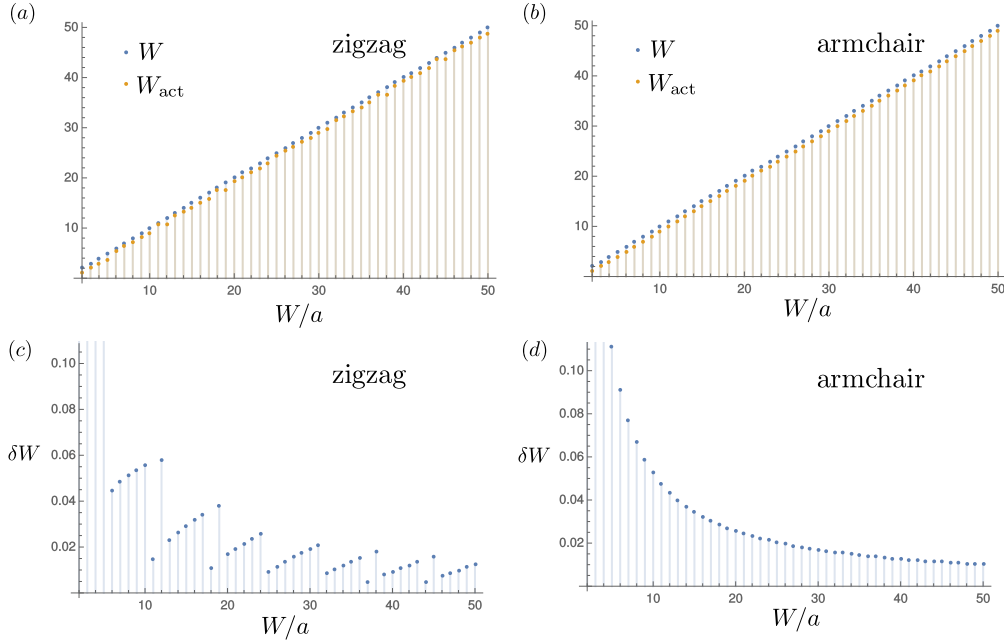


FIGURE A.5: Demonstration that the difference between the parameter  $W$  used in the code and the actual width  $W_{\text{act}}$  is negligible and vanishes for wider ribbons.

Another scheme to express the width of a ribbon is shown in Fig. 2 of Ref. [20]. Here,  $N$  is the number of dimer lines for the armchair ribbon and the number of zigzag lines for the zigzag ribbon. The corresponding relation between  $W_{\text{act}}$  and  $N$  for the armchair ribbon is

$$W_{\text{act}} = \frac{N-1}{2}a, \quad (\text{A.4})$$

while for the zigzag ribbon it is

$$W_{\text{act}} = \frac{\sqrt{3}}{2}Na + \frac{a}{2\sqrt{3}}. \quad (\text{A.5})$$

Consequently, the condition for the metallic armchair ribbon translates from  $N = a \pmod{3}$  to  $2W_{\text{act}} = 2a \pmod{3}$ .

---

## BIBLIOGRAPHY

- [1] P. R. Wallace, Phys. Rev. **71**, 622 (1947).
- [2] K. S. Novoselov, A. K. Geim, S. V. Morozov, D. Jiang, Y. Zhang, S. V. Dubonos, I. V. Grigorieva, and A. A. Firsov, Science **306**, 666 (2004).
- [3] A. K. Geim and K. S. Novoselov, *The Nobel Prize in Physics* (2010), [http://www.nobelprize.org/nobel\\_prizes/physics/laureates/2010/](http://www.nobelprize.org/nobel_prizes/physics/laureates/2010/).
- [4] E. H. Hall, Am. J. Math. **2**, 287 (1879).
- [5] K. von Klitzing, G. Dorda, and M. Pepper, Phys. Rev. Lett. **45**, 494 (1980).
- [6] K. von Klitzing, *The Nobel Prize in Physics* (1985), [http://www.nobelprize.org/nobel\\_prizes/physics/laureates/1985/](http://www.nobelprize.org/nobel_prizes/physics/laureates/1985/).
- [7] K. S. Novoselov, Z. Jiang, Y. Zhang, S. V. Morozov, H. L. Stormer, U. Zeitler, J. C. Maan, G. S. Boebinger, P. Kim, and A. K. Geim, Science **315**, 1379 (2007).
- [8] D. C. Tsui, H. L. Stormer, and A. C. Gossard, Phys. Rev. Lett. **48**, 1559 (1982).
- [9] R. B. Laughlin, Phys. Rev. Lett. **50**, 1395 (1983).
- [10] D. J. Thouless, F. D. M. Haldane, and J. M. Kosterlitz, *The Nobel Prize in Physics* (2016), [http://www.nobelprize.org/nobel\\_prizes/physics/laureates/2016/](http://www.nobelprize.org/nobel_prizes/physics/laureates/2016/).
- [11] M. Z. Hasan and C. L. Kane, Rev. Mod. Phys. **82**, 3045 (2010).
- [12] J. Bardeen, L. N. Cooper, and J. R. Schrieffer, *The Nobel Prize in Physics* (1972), [http://www.nobelprize.org/nobel\\_prizes/physics/laureates/1972/](http://www.nobelprize.org/nobel_prizes/physics/laureates/1972/).
- [13] T. Schaetz, C. R. Monroe, and T. Esslinger, New J. Phys. **15**, 085009 (2013).
- [14] L. E. F. Torres, S. Roche, and J.-C. Charlier, *Introduction to graphene-based nano-materials: from electronic structure to quantum transport* (Cambridge University Press, Cambridge, England, 2014).

- [15] M. Y. Han, B. Özyilmaz, Y. Zhang, and P. Kim, Phys. Rev. Lett. **98**, 206805 (2007).
- [16] D. V. Kosynkin, A. L. Higginbotham, A. Sinitskii, J. R. Lomeda, A. Dimiev, B. K. Price, and J. M. Tour, Nature **458**, 872 (2009).
- [17] P. Ruffieux, S. Wang, B. Yang, C. Sánchez-Sánchez, J. Liu, T. Dienel, L. Talirz, P. Shinde, C. A. Pignedoli, D. Passerone, *et al.*, Nature **531**, 489 (2016).
- [18] D. Hug, S. Zihlmann, M. K. Rehmann, Y. B. Kalyoncu, T. N. Camenzind, L. Marot, K. Watanabe, T. Taniguchi, and D. M. Zumbühl, NPJ 2D Mater. Appl. **1**, 21 (2017).
- [19] L. C. Campos, V. R. Manfrinato, J. D. Sanchez-Yamagishi, J. Kong, and P. Jarillo-Herrero, Nano Lett. **9**, 2600 (2009).
- [20] K. Wakabayashi, K. Sasaki, T. Nakanishi, and T. Enoki, Sci. Technol. Adv. Mater. **11**, 054504 (2010).
- [21] A. Rycerz, J. Tworzydło, and C. W. J. Beenakker, Nat. Phys. **3**, 172 (2007).
- [22] K. Wakabayashi, M. Fujita, H. Ajiki, and M. Sigrist, Phys. Rev. B **59**, 8271 (1999).
- [23] Y.-W. Son, M. L. Cohen, and S. G. Louie, Phys. Rev. Lett. **97**, 216803 (2006).
- [24] R. Peierls, in *Selected Scientific Papers of Sir Rudolf Peierls* (Co-published by Imperial College Press and World Scientific Publishing Co., 1997), pp. 97–120.
- [25] O. Shevtsov, P. Carmier, C. Petitjean, C. Groth, D. Carpentier, and X. Waintal, Phys. Rev. X **2**, 031004 (2012).
- [26] A. V. Volkov, A. A. Shylau, and I. V. Zozoulenko, Phys. Rev. B **86**, 155440 (2012).
- [27] N. Menezes, V. S. Alves, E. C. Marino, L. Nascimento, L. O. Nascimento, and C. Morais Smith, Phys. Rev. B **95**, 245138 (2017).
- [28] A. R. Akhmerov and C. W. J. Beenakker, Phys. Rev. Lett. **98**, 157003 (2007).
- [29] Y. Zhang, Y.-W. Tan, H. L. Stormer, and P. Kim, Nature **438**, 201 (2005).
- [30] C. W. Groth, M. Wimmer, A. R. Akhmerov, and X. Waintal, New J. Phys. **16**, 063065 (2014).
- [31] J. R. Schaibley, H. Yu, G. Clark, P. Rivera, J. S. Ross, K. L. Seyler, W. Yao, and X. Xu, Nature Reviews Materials **1**, 16055 (2016).
- [32] D. Xiao, M.-C. Chang, and Q. Niu, Rev. Mod. Phys. **82**, 1959 (2010).
- [33] D. Xiao, W. Yao, and Q. Niu, Phys. Rev. Lett. **99**, 236809 (2007).
- [34] J. Li, K. Wang, K. J. McFaul, Z. Zern, Y. Ren, K. Watanabe, T. Taniguchi, Z. Qiao, and J. Zhu, Nat. Nanotechnol. **11**, 1060 (2016).
- [35] M. Sui, G. Chen, L. Ma, W.-Y. Shan, D. Tian, K. Watanabe, T. Taniguchi, X. Jin, W. Yao, D. Xiao, *et al.*, Nat. Phys. **11**, 1027 (2015).

- [36] Y. Shimazaki, M. Yamamoto, I. V. Borzenets, K. Watanabe, T. Taniguchi, and S. Tarucha, *Nat. Phys.* **11**, 1032 (2015).
- [37] W. Yao, D. Xiao, and Q. Niu, *Phys. Rev. B* **77**, 235406 (2008).
- [38] D. Xiao, G.-B. Liu, W. Feng, X. Xu, and W. Yao, *Phys. Rev. Lett.* **108**, 196802 (2012).
- [39] J. M. Pereira, Jr., F. M. Peeters, R. N. C. Filho, and G. A. Farias, *J. Phys. Condens. Matter* **21**, 045301 (2009).
- [40] M. Ramezani Masir, A. Matulis, and F. M. Peeters, *Phys. Rev. B* **84**, 245413 (2011).
- [41] D. Moldovan, M. Ramezani Masir, L. Covaci, and F. M. Peeters, *Phys. Rev. B* **86**, 115431 (2012).
- [42] S.-G. Cheng, J. Zhou, H. Jiang, and Q.-F. Sun, *New J. Phys.* **18**, 103024 (2016).
- [43] S. Milovanović and F. Peeters, *Appl. Phys. Lett.* **109**, 203108 (2016).
- [44] M. Settnes, S. R. Power, M. Brandbyge, and A.-P. Jauho, *Phys. Rev. Lett.* **117**, 276801 (2016).
- [45] M. M. Grujić, M. Ž. Tadić, and F. M. Peeters, *Phys. Rev. Lett.* **113**, 046601 (2014).
- [46] M. O. Goerbig, *Rev. Mod. Phys.* **83**, 1193 (2011).
- [47] J. E. Müller, *Phys. Rev. Lett.* **68**, 385 (1992).
- [48] S. Park and H.-S. Sim, *Phys. Rev. B* **77**, 075433 (2008).
- [49] L. Oroszlány, P. Rakytá, A. Kormányos, C. J. Lambert, and J. Cserti, *Phys. Rev. B* **77**, 081403 (2008).
- [50] T. K. Ghosh, A. De Martino, W. Häusler, L. Dell’Anna, and R. Egger, *Phys. Rev. B* **77**, 081404 (2008).
- [51] E. Prada, P. San-Jose, and L. Brey, *Phys. Rev. Lett.* **105**, 106802 (2010).
- [52] P. Carmier, C. Lewenkopf, and D. Ullmo, *Phys. Rev. B* **81**, 241406 (2010).
- [53] P. Carmier, C. Lewenkopf, and D. Ullmo, *Phys. Rev. B* **84**, 195428 (2011).
- [54] P. Rickhaus, P. Makk, M.-H. Liu, E. Tóvári, M. Weiss, R. Maurand, K. Richter, and C. Schönenberger, *Nat. Commun.* **6**, 6470 (2015).
- [55] C. W. J. Beenakker, A. R. Akhmerov, P. Recher, and J. Tworzydło, *Phys. Rev. B* **77**, 075409 (2008).
- [56] Y. Liu, R. P. Tiwari, M. Brada, C. Bruder, F. V. Kusmartsev, and E. J. Mele, *Phys. Rev. B* **92**, 235438 (2015).
- [57] L. S. Cavalcante, A. Chaves, D. R. da Costa, G. A. Farias, and F. M. Peeters, *Phys. Rev. B* **94**, 075432 (2016).

- [58] L. Cohnitz, A. De Martino, W. Häusler, and R. Egger, Phys. Rev. B **94**, 165443 (2016).
- [59] C. Fräßdorf, L. Trifunovic, N. Bogdanoff, and P. W. Brouwer, Phys. Rev. B **94**, 195439 (2016).
- [60] K. Kolasiński, A. Mreńca-Kolasińska, and B. Szafran, Phys. Rev. B **95**, 045304 (2017).
- [61] T. Taychatanapat, J. Y. Tan, Y. Yeo, K. Watanabe, T. Taniguchi, and B. Özyilmaz, Nat. Commun. **6**, 6093 (2015).
- [62] J. Williams, L. DiCarlo, and C. Marcus, Science **317**, 638 (2007).
- [63] M. Zarenia, J. M. Pereira, F. M. Peeters, and G. A. Farias, Phys. Rev. B **87**, 035426 (2013).
- [64] D. A. Abanin and L. S. Levitov, Science **317**, 641 (2007).
- [65] J. Tworzydło, I. Snyman, A. R. Akhmerov, and C. W. J. Beenakker, Phys. Rev. B **76**, 035411 (2007).
- [66] L. Brey and H. A. Fertig, Phys. Rev. B **73**, 195408 (2006).
- [67] C. W. J. Beenakker, Rev. Mod. Phys. **80**, 1337 (2008).
- [68] S. Milovanović, M. Ramezani Masir, and F. Peeters, Appl. Phys. Lett. **105**, 123507 (2014).
- [69] A. R. Akhmerov, J. H. Bardarson, A. Rycerz, and C. W. J. Beenakker, Phys. Rev. B **77**, 205416 (2008).
- [70] C. Handschin, P. Makk, P. Rickhaus, R. Maurand, K. Watanabe, T. Taniguchi, K. Richter, M.-H. Liu, and C. Schönenberger, Nano Lett. **17**, 5389 (2017).
- [71] H. B. Heersche, P. Jarillo-Herrero, J. B. Oostinga, L. M. K. Vandersypen, and A. F. Morpurgo, Nature **446**, 56 (2007).
- [72] D. Jeong, J.-H. Choi, G.-H. Lee, S. Jo, Y.-J. Doh, and H.-J. Lee, Phys. Rev. B **83**, 094503 (2011).
- [73] G.-H. Lee, S. Kim, S.-H. Jhi, and H.-J. Lee, Nat. Commun. **6**, 6181 (2015).
- [74] C. W. J. Beenakker, Phys. Rev. Lett. **97**, 067007 (2006).
- [75] M. P. Anantram and S. Datta, Phys. Rev. B **53**, 16390 (1996).
- [76] D. K. Efetov, L. Wang, C. Handschin, K. B. Efetov, J. Shuang, R. Cava, T. Taniguchi, K. Watanabe, J. Hone, C. R. Dean, *et al.*, Nat. Phys. **12**, 328 (2015).
- [77] G.-H. Park, M. Kim, K. Watanabe, T. Taniguchi, and H.-J. Lee, Sci. Rep. **7**, 10953 (2017).

- [78] G.-H. Lee, K.-F. Huang, D. K. Efetov, D. S. Wei, S. Hart, T. Taniguchi, K. Watanabe, A. Yacoby, and P. Kim, *Nat. Phys.* **13**, 693 (2017).
- [79] R. Ribeiro-Palau, F. Lafont, J. Brun-Picard, D. Kazazis, A. Michon, F. Cheynis, O. Couturaud, C. Consejo, B. Jouault, W. Poirier, *et al.*, *Nat. Nanotechnol.* **10**, 965 (2015).
- [80] I. M. Khaymovich, N. M. Chtchelkatchev, I. A. Shereshevskii, and A. S. Mel'nikov, *EPL* **91**, 17005 (2010).
- [81] Y. Liu, R. P. Tiwari, M. Brada, C. Bruder, F. V. Kusmartsev, and E. J. Mele, *Phys. Rev. B* **92**, 235438 (2015).
- [82] D. A. Abanin, P. A. Lee, and L. S. Levitov, *Phys. Rev. Lett.* **96**, 176803 (2006).
- [83] P. San-Jose, J. L. Lado, R. Aguado, F. Guinea, and J. Fernández-Rossier, *Phys. Rev. X* **5**, 041042 (2015).
- [84] C.-K. Chiu, J. C. Y. Teo, A. P. Schnyder, and S. Ryu, *Rev. Mod. Phys.* **88**, 035005 (2016).
- [85] M. Atiyah, *K-theory* (CRC Press, 2018).
- [86] M. Fecko, *Differential geometry and Lie groups for physicists* (Cambridge University Press, Cambridge, England, 2006).
- [87] B. A. Bernevig, T. L. Hughes, and S.-C. Zhang, *Science* **314**, 1757 (2006).
- [88] R. M. Kaufmann, D. Li, and B. Wehefritz-Kaufmann, *Rev. Math. Phys.* **28**, 1630003 (2016).
- [89] P. W. Anderson, *Phys. Rev.* **109**, 1492 (1958).
- [90] C. W. Groth, M. Wimmer, A. R. Akhmerov, J. Tworzydło, and C. W. J. Beenakker, *Phys. Rev. Lett.* **103**, 196805 (2009).
- [91] E. Prodan, *Phys. Rev. B* **83**, 195119 (2011).
- [92] Y. Xing, L. Zhang, and J. Wang, *Phys. Rev. B* **84**, 035110 (2011).
- [93] A. Yamakage, K. Nomura, K.-I. Imura, and Y. Kuramoto, *J. Phys. Soc. Jpn.* **80**, 053703 (2011).
- [94] H.-M. Guo, G. Rosenberg, G. Refael, and M. Franz, *Phys. Rev. Lett.* **105**, 216601 (2010).
- [95] B. Fu, H. Zheng, Q. Li, Q. Shi, and J. Yang, *Phys. Rev. B* **90**, 214502 (2014).
- [96] I. Garate, *Phys. Rev. Lett.* **110**, 046402 (2013).
- [97] J. Song, H. Liu, H. Jiang, Q.-f. Sun, and X. C. Xie, *Phys. Rev. B* **85**, 195125 (2012).
- [98] S.-H. Lv, J. Song, and Y.-X. Li, *J. Appl. Phys.* **114**, 183710 (2013).

- [99] B. Aufray, A. Kara, S. Vizzini, H. Oughaddou, C. Léandri, B. Ealet, and G. L. Lay, *Appl. Phys. Lett.* **96**, 183102 (2010).
- [100] A. Kara, H. Enriquez, A. P. Seitsonen, L. L. Y. Voon, S. Vizzini, B. Aufray, and H. Oughaddou, *Surf. Sci. Rep.* **67**, 1 (2012).
- [101] M. E. Dávila, L. Xian, S. Cahangirov, A. Rubio, and G. L. Lay, *New J. Phys.* **16**, 095002 (2014).
- [102] F.-f. Zhu, W.-j. Chen, Y. Xu, C.-l. Gao, D.-d. Guan, C.-h. Liu, D. Qian, S.-C. Zhang, and J.-f. Jia, *Nat. Mater.* **14**, 1020 (2015).
- [103] E. Prodan, *J. Phys. A* **44**, 113001 (2011).
- [104] C. P. Orth, G. Strübi, and T. L. Schmidt, *Phys. Rev. B* **88**, 165315 (2013).
- [105] A. Rod, T. L. Schmidt, and S. Rachel, *Phys. Rev. B* **91**, 245112 (2015).
- [106] C. Weeks, J. Hu, J. Alicea, M. Franz, and R. Wu, *Phys. Rev. X* **1**, 021001 (2011).
- [107] H. Jiang, Z. Qiao, H. Liu, J. Shi, and Q. Niu, *Phys. Rev. Lett.* **109**, 116803 (2012).
- [108] T. Ando, *J. Phys. Soc. Jpn.* **75**, 074716 (2006).
- [109] M. Ishigami, J. H. Chen, W. G. Cullen, M. S. Fuhrer, and E. D. Williams, *Nano Lett.* **7**, 1643 (2007).
- [110] S. Fratini and F. Guinea, *Phys. Rev. B* **77**, 195415 (2008).
- [111] A. Varlet, M. Mucha-Kruczyński, D. Bischoff, P. Simonet, T. Taniguchi, K. Watanabe, V. Fal'ko, T. Ihn, and K. Ensslin, *Synth. Met.* **210**, 19 (2015).
- [112] M. S. Nevius, M. Conrad, F. Wang, A. Celis, M. N. Nair, A. Taleb-Ibrahimi, A. Tejeda, and E. H. Conrad, *Phys. Rev. Lett.* **115**, 136802 (2015).
- [113] P. Titum, N. H. Lindner, M. C. Rechtsman, and G. Refael, *Phys. Rev. Lett.* **114**, 056801 (2015).
- [114] Z. Yang, F. Gao, X. Shi, X. Lin, Z. Gao, Y. Chong, and B. Zhang, *Phys. Rev. Lett.* **114**, 114301 (2015).
- [115] G. Jotzu, M. Messer, R. Desbuquois, M. Lebrat, T. Uehlinger, D. Greif, and T. Esslinger, *Nature* **515**, 237 (2014).
- [116] E. J. Meier, F. A. An, A. Dauphin, M. Maffei, P. Massignan, T. L. Hughes, and B. Gadway, *Observation of the topological Anderson insulator in disordered atomic wires* (2018), arXiv:1802.02109.
- [117] C. L. Kane and E. J. Mele, *Phys. Rev. Lett.* **95**, 226801 (2005).
- [118] C. L. Kane and E. J. Mele, *Phys. Rev. Lett.* **95**, 146802 (2005).
- [119] H. Min, J. E. Hill, N. A. Sinitsyn, B. R. Sahu, L. Kleinman, and A. H. MacDonald, *Phys. Rev. B* **74**, 165310 (2006).



- [120] D. Huertas-Hernando, F. Guinea, and A. Brataas, Phys. Rev. B **74**, 155426 (2006).
- [121] Y. Yao, F. Ye, X.-L. Qi, S.-C. Zhang, and Z. Fang, Phys. Rev. B **75**, 041401 (2007).
- [122] H. Bruus and K. Flensberg, *Many-body quantum theory in condensed matter physics: an introduction* (Oxford University Press, Oxford, 2004).
- [123] Y. Xu, B. Yan, H.-J. Zhang, J. Wang, G. Xu, P. Tang, W. Duan, and S.-C. Zhang, Phys. Rev. Lett. **111**, 136804 (2013).
- [124] C.-C. Liu, H. Jiang, and Y. Yao, Phys. Rev. B **84**, 195430 (2011).
- [125] S. Murmann, F. Deuretzbacher, G. Zürn, J. Bjerlin, S. M. Reimann, L. Santos, T. Lompe, and S. Jochim, Phys. Rev. Lett. **115**, 215301 (2015).
- [126] S. Krinner, T. Esslinger, and J.-P. Brantut, J. Phys. Condens. Matter **29**, 343003 (2017).
- [127] M. Randeria and E. Taylor, Annu. Rev. Condens. Matter Phys. **5**, 209 (2014).
- [128] J. Bardeen, L. N. Cooper, and J. R. Schrieffer, Phys. Rev. **108**, 1175 (1957).
- [129] C. Chin, R. Grimm, P. Julienne, and E. Tiesinga, Rev. Mod. Phys. **82**, 1225 (2010).
- [130] A. J. Leggett, *Quantum liquids: Bose condensation and Cooper pairing in condensed-matter systems* (Oxford University Press, Oxford, 2006).
- [131] W. Ketterle and M. W. Zwierlein, La Rivista del Nuovo Cimento **31**, 247–422 (2008).
- [132] A. A. M. Staring, L. W. Molenkamp, B. W. Alphenaar, H. van Houten, O. J. A. Buyk, M. A. A. Mabeoone, C. W. J. Beenakker, and C. T. Foxon, EPL **22**, 57 (1993).
- [133] G. D. Guttman, E. Ben-Jacob, and D. J. Bergman, Phys. Rev. B **51**, 17758 (1995).
- [134] F. Giazotto, T. T. Heikkilä, A. Luukanen, A. M. Savin, and J. P. Pekola, Rev. Mod. Phys. **78**, 217 (2006).
- [135] P. Machon, M. Eschrig, and W. Belzig, Phys. Rev. Lett. **110**, 047002 (2013).
- [136] A. Ozaeta, P. Virtanen, F. S. Bergeret, and T. T. Heikkilä, Phys. Rev. Lett. **112**, 057001 (2014).
- [137] S. Kolenda, M. J. Wolf, and D. Beckmann, Phys. Rev. Lett. **116**, 097001 (2016).
- [138] B. T. Seaman, M. Krämer, D. Z. Anderson, and M. J. Holland, Phys. Rev. A **75**, 023615 (2007).
- [139] R. A. Pepino, J. Cooper, D. Z. Anderson, and M. J. Holland, Phys. Rev. Lett. **103**, 140405 (2009).

- [140] R. A. Pepino, J. Cooper, D. Meiser, D. Z. Anderson, and M. J. Holland, Phys. Rev. A **82**, 013640 (2010).
- [141] M. Bruderer and W. Belzig, Phys. Rev. A **85**, 013623 (2012).
- [142] A. Ivanov, G. Kordas, A. Komnik, and S. Wimberger, Eur. Phys. J. B **86**, 345 (2013).
- [143] J.-P. Brantut, J. Meineke, D. Stadler, S. Krinner, and T. Esslinger, Science **337**, 1069 (2012).
- [144] D. Stadler, S. Krinner, J. Meineke, J.-P. Brantut, and T. Esslinger, Nature **491**, 736 (2012).
- [145] J.-P. Brantut, C. Grenier, J. Meineke, D. Stadler, S. Krinner, C. Kollath, T. Esslinger, and A. Georges, Science **342**, 713 (2013).
- [146] S. Krinner, D. Stadler, D. Husmann, J.-P. Brantut, and T. Esslinger, Nature **517**, 64 (2014).
- [147] D. Husmann, S. Uchino, S. Krinner, M. Lebrat, T. Giamarchi, T. Esslinger, and J.-P. Brantut, Science **350**, 1498 (2015).
- [148] C. Grenier, C. Kollath, and A. Georges, *Probing thermoelectric transport with cold atoms* (2012), arXiv:1209.3942.
- [149] C. Grenier, A. Georges, and C. Kollath, Phys. Rev. Lett. **113**, 200601 (2014).
- [150] C. Grenier, C. Kollath, and A. Georges, Comptes Rendus Physique **17**, 1161 (2016).
- [151] A. Barone and G. Paternò, *Physics and Applications of the Josephson Effect* (Wiley, New York, 1982).
- [152] E. Zhao, T. Löfwander, and J. A. Sauls, Phys. Rev. B **69**, 134503 (2004).
- [153] W. Belzig, C. Schroll, and C. Bruder, Phys. Rev. A **75**, 063611 (2007).
- [154] M. Tinkham, *Introduction to Superconductivity* (Dover, New York, 2004).
- [155] *Kwant documentation*, <https://kwant-project.org/doc/>.
- [156] *The jupyter notebook*, <http://jupyter.org/index.html>.

---

## LIST OF PUBLICATIONS

- *The topological Anderson insulator phase in the Kane-Mele model*  
C. P. Orth, T. Sekera, C. Bruder, and T. L. Schmidt  
Sci. Rep. **6**, 24007 (2016)
- *Thermoelectricity in a junction between interacting cold atomic Fermi gases*  
T. Sekera, C. Bruder, and W. Belzig  
Phys. Rev. A **94**, 033618 (2016)
- *Switchable valley filter based on a graphene p-n junction in a magnetic field*  
T. Sekera, C. Bruder, E. J. Mele, and R. P. Tiwari  
Phys. Rev. B **95**, 205431 (2017)
- *Spin transport in a graphene normal-superconductor junction in the quantum Hall regime*  
T. Sekera, C. Bruder, and R. P. Tiwari  
arXiv:1807.06975  
*submitted to Phys. Rev. B*